SIMULATION STUDIES ON SHAPE AND GROWTH KINETICS FOR FRACTAL AGGREGATES IN AEROSOL AND COLLOIDAL SYSTEMS

by

WILLIAM RAYMOND HEINSON

B.S., Kansas State University, 2008

AN ABSTRACT OF A DISSERTATION

submitted in partial fulfillment of the requirements for the degree

DOCTOR OF PHILOSOPHY

Department of Physics
College of Arts and Science

KANSAS STATE UNIVERSITY
Manhattan, Kansas

2015

Abstract

The aim of this work is to explore, using computational techniques that simulate the motion and subsequent aggregation of particles in aerosol and colloidal systems, many common but not well studied systems that form fractal clusters. Primarily the focus is on cluster shape and growth kinetics. The structure of clusters made under diffusion limited cluster-cluster aggregation (DLCA) is looked at. More specifically, the shape anisotropy is found to have an inverse relationship on the scaling prefactor k_0 and have no effect on the fractal dimension D_f. An analytical model that predicts the shape and fractal dimension of diffusion limited cluster-cluster aggregates is tested and successfully predicts cluster shape and dimensionality. Growth kinetics of cluster-cluster aggregation in the free molecular regime where the system starts with ballistic motion and then transitions to diffusive motion as the aggregates grow in size is studied. It is shown that the kinetic exponent will crossover from the ballistic to the diffusional values and the onset of this crossover is predicted by when the nearest neighbor Knudsen number reaches unity. Simulations were carried out for a system in which molten particles coalesce into spheres, then cool till coalescing stops and finally the polydispersed monomers stick at point contacts to form fractal clusters. The kinetic exponent and overall cluster structure for these aggregates was found to be in agreement with DLCA that started with monodispersed monomers. Colloidal aggregation in the presence of shear was studied in detail. Study of a colloidal system characterized a by short-range attractive potential showed that weak shear enhanced the aggregation process. Strong shear led to fragmentation and subsequent nucleation as cluster growth rebounded after an induction time.

SIMULATION STUDIES ON SHAPE AND GROWTH KINETICS FOR FRACTAL AGGREGATES IN AEROSOL AND COLLOIDAL SYSTEMS

by

WILLIAM RAYMOND HEINSON

B.S., Kansas State University, 2008

A DISSERTATION

submitted in partial fulfillment of the requirements for the degree

DOCTOR OF PHILOSOPHY

Department of Physics
College of Arts and Science

KANSAS STATE UNIVERSITY
Manhattan, Kansas

2015

Approved by:

Major Professor
Amit Chakrabarti

Copyright

Abstract

The aim of this work is to explore, using computational techniques that simulate the motion and subsequent aggregation of particles in aerosol and colloidal systems, many common but not well studied systems that form fractal clusters. Primarily the focus is on cluster shape and growth kinetics. The structure of clusters made under diffusion limited cluster-cluster aggregation (DLCA) is looked at. More specifically, the shape anisotropy is found to have an inverse relationship on the scaling prefactor "k" _"0" and have no effect on the fractal dimension "D" _"f" . An analytical model that predicts the shape and fractal dimension of diffusion limited cluster-cluster aggregates is tested and successfully predicts cluster shape and dimensionality. Growth kinetics of cluster-cluster aggregation in the free molecular regime where the system starts with ballistic motion and then transitions to diffusive motion as the aggregates grow in size is studied. It is shown that the kinetic exponent will crossover from the ballistic to the diffusional values and the onset of this crossover is predicted by when the nearest neighbor Knudsen number reaches unity. Simulations were carried out for a system in which molten particles coalesce into spheres, then cool till coalescing stops and finally the polydispersed monomers stick at point contacts to form fractal clusters. The kinetic exponent and overall cluster structure for these aggregates was found to be in agreement with DLCA that started with monodispersed monomers. Colloidal aggregation in the presence of shear was studied in detail. Study of a colloidal system characterized a by short-range attractive potential showed that weak shear enhanced the aggregation process. Strong shear led to fragmentation and subsequent nucleation as cluster growth rebounded after an induction time.

Table of Contents

List of Figures

List of Tables

Acknowledgements

I would like to thank my advisor, Professor Amit Chakrabarti, for taking a chance on me and giving me the opportunity to pursue this research. His encouragement and leadership helped me develop as a scientist.

I also would like to thank Professor Chris Sorensen for all the guidance he has given me throughout my PhD studies. His office was always open and our discussions were always enlightening.

I would like to thank my committee members: Professor Michael O'Shea, Professor Steve Eckels and Professor Christer Aakeroy. My colleagues who were of great help during my research and studies also deserve many thanks. I would like to especially thank my friends Raiya Ebini, Justin Maughan, Siddique Khan, Omer Farooq, Mai Ababneh and Yuli Wang for all their support and advice.

Chapter 1 - Introduction

1.1 Fractals

"Many important spatial patterns of Nature are either irregular or fragmented to such an extreme degree that ... classical geometry ... is hardly of any help in describing their form. ... I hope to show that it is possible in many cases to remedy this absence of geometric representation by using a family of shapes I propose to call fractals -- or fractal sets." [1]

Much of the work discussed in this dissertation will deal with flame soot aggregates and their geometry. These soot aggregates are formed from the collisions between dispersed monomers with random trajectories and in-turn have random shape. Flame soot aggregates with random shape have been known for years; for example diesel exhaust particulates are randomly shaped black carbon aggregates, but their random structure has made descriptive analysis difficult. The best that could be done was to describe aggregates with words such as "fluffy" or "grainy". That changed in 1975 when the mathematician Mandelbrot developed the idea of fractal geometry. [1]

Fractals have repeating branching structures that lead to scale invariance. For example, consider a toy model of a tree. First start with the trunk rising from the ground then split into two branches; those two branches would continue and at some point split again and so on. If you were to break off a twig from this model tree and compare it to the whole, the zoomed-in branch would look like the entire tree. Since the tree looks the same at all length scales it has scale invariance.

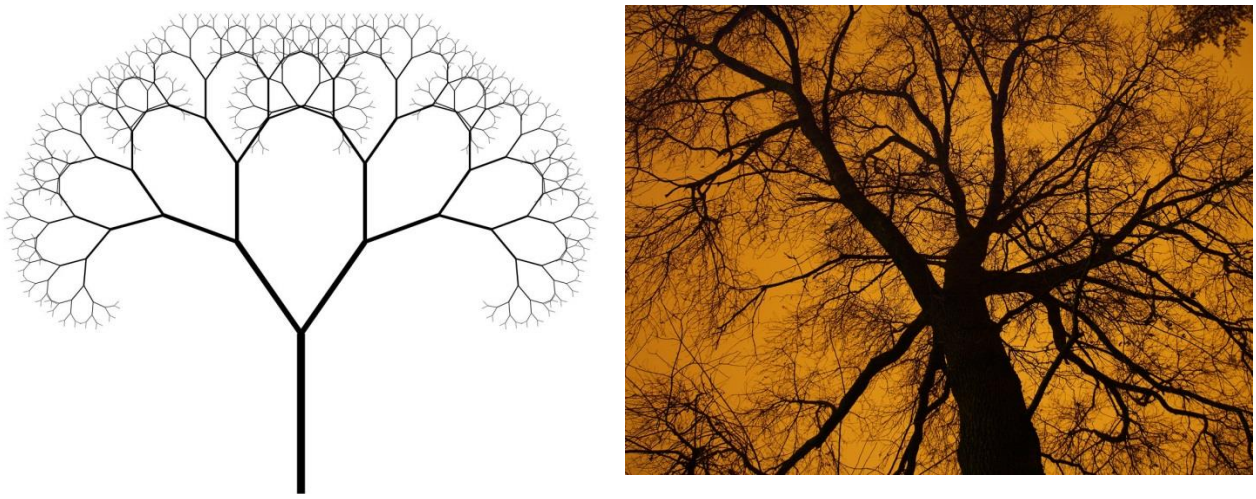

Figure 1.1 Model tree compared to actual tree. Both show scale invariance.[2], [3]

Notice that in Figure 1.1 the tree encompasses a lot of empty space. Fractals do not fill space like classical geometric objects. In classical geometry the amount of space an object fills is proportional to its characteristic length scale raised to the spatial dimension i.e. the area of a square is $A=L^2$ or the volume of a sphere is $V\sim r^3$. Fractal's branching structure allows them to reach larger sizes without filling much space. To get to larger sizes without filling space the scaling dimension must be less than the spatial dimension and a non-integer scaling exponent called the fractal dimension, D_f, is introduced. For example a fractal tree would have a volume that goes as $V\sim L^{D_f}$ where L is the tree's characteristic length and D_f is the fractal dimension which has value $D_f<3$.

1.2 Fractals from Random Aggregates

When monomers aggregate from random motion they can form clusters that also have fractal morphology[4]–[6]. Most of these fractal aggregates can be described by three aggregation models: percolation, cluster-monomer and cluster-cluster. A percolation model starts with a d-dimensional lattice in which all sites on the lattice are empty. Then lattice sites are filled

randomly. If two adjacent sites become occupied they are considered joined into a cluster. As more sites become filled the clusters become larger till a single cluster reaches a desired size. An example of a percolation cluster is shown in Figure 1.2a. In a cluster-monomer aggregation scheme the system starts with a seed monomer in the center and additional monomers are introduced one at a time that randomly walk in the simulation space. If the monomer hits the seed it sticks and forms a cluster. Then new monomers are introduced one at a time. If they hit the cluster they stick and the cluster grows. An example of a cluster-monomer aggregate is shown in Figure 1.2b. The final aggregation scheme for random motion is called cluster-cluster aggregation. Here many monomers are placed in the simulation space and all move with random motion. Monomers will stick upon collision and form clusters. These clusters are also free to move around and will stick with any cluster or monomer they collide with. An example of cluster-cluster aggregation is shown in Figure 1.2c.

From the examples in Figure 1.2 it is clear that the percolation cluster is the densest and thus has the largest fractal dimension D_f and the cluster-cluster aggregates are the least dense and therefore have the smallest D_f. The cluster-monomer type aggregates are special due to their centered symmetry while the other two are the result of many centers of growth colliding and therefore exhibit a more oblong shape.

The first works done with fractal aggregates from random growth dealt with the percolation and cluster-monomer growth models but in this work the systems studied such as flame soot and colloidal gels exhibited the cluster-cluster type aggregation.

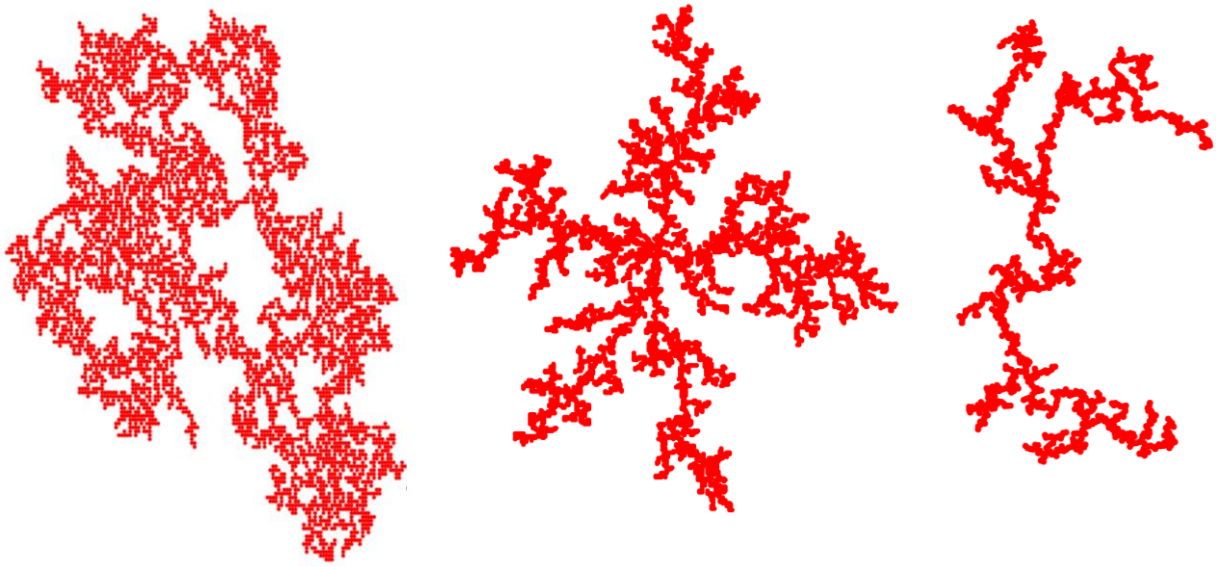

a. b. c.

Figure 1.2 (a) A percolation cluster. D_f=2.55 [7]. (b) A diffusion limited cluster-monomer aggregate. D_f=2.5 [8]. (c) A diffusion limited cluster-cluster aggregate. D_f=1.8 [9].

1.3 Cluster-Cluster Aggregation Growth Kinetics

Growth Kinetics in cluster-cluster aggregation models is described by the Smoluchowski equation[10]:

$$\frac{dn_N}{dt} = \sum_{i=1}^{N-1} K(i, N-i)\, n_i n_{N-i} - n_N \sum_{i=1}^{\infty} K(i,N) n_i \qquad (1.1)$$

The Smoluchowski equation shows how the concentration of clusters n_N, made up of N monomers, changes with time. The only way the number of clusters with N monomers can change is for two clusters whose mass equal N to aggregate and add to the tally or for a cluster of mass N to aggregate with some other cluster and decrease the population. The first term of equation 1.1 describes the addition of clusters of mass N while the second term handles the subtractions from the population of mass N clusters. Both terms are linked by the aggregation

kernel K. The aggregation kernel is proportional to the colliding clusters relative collision cross-sectional area, A and relative velocity, v

$$K \sim Av \tag{1.2}$$

Ballistic Motion

When clusters move in a straight line motion due to the equipartition of energy their velocity is

$$v = \sqrt{\frac{3k_B T}{m}} \tag{1.3}$$

where T is the temperature, k_B is the Boltzmann constant and m is the mass of the cluster. Since the mass of the cluster is directly proportional to the number of monomers in the cluster, the velocity is proportional to

$$v \sim N^{-1/2} \tag{1.4}$$

The volume of a fractal cluster is also related to cluster length by $V \sim L^{D_f}$. The monomers are considered to be at a constant density and therefore the volume of a cluster is proportional to N. Thus cluster length is

$$L \sim N^{1/D_f} \tag{1.5}$$

From equation 1.4 and 1.5 it becomes clear the aggregation kernel K can be written as

$$K \sim N^{\lambda} \tag{1.6}$$

where in the ballistic case the scaling exponent of the kernel is

$$\lambda = \frac{2}{D_f} - \frac{1}{2} \tag{1.7}$$

Using the expected value for fractal dimension of ballistic cluster-cluster aggregation D_f=1.9, the scaling exponent of the aggregation kernel is λ=0.55.

Diffusional Motion

In diffusional motion the mean square displacement of an object is

$$\langle x^2 \rangle = 2dDt \tag{1.8}$$

where d is the spatial dimension, D is the diffusion constant, t is the time and x is the displacement. By equation 1.8 the time it takes a cluster to travel some characteristic length R_c is

$$t_c = \frac{R_c^2}{2dD} \tag{1.9}$$

Thus the velocity of a cluster moving under diffusion is proportional to

$$v \sim \frac{D}{R_c} \tag{1.10}$$

In the continuum limit the diffusion constant D is inversely proportional to the cluster length, thus

$$v \sim \frac{1}{R_c L} \tag{1.11}$$

In the cluster dilute limit the only characteristic length R_c scale is L and since the cluster area is proportional to L^2, the aggregation kernel becomes a constant with scaling exponent λ=0. When the system is cluster dense the nearest-neighbor separation R_{nn} becomes the characteristic length R_c. The nearest-neighbor separation is the distance between clusters and equals

$$R_{nn} = \left(\frac{System\ Volume}{N_c}\right)^{\frac{1}{3}} \tag{1.12}$$

where N_c is the number of clusters in the system. If the total number of monomers in the system is N_m then $N_c = N_m / N$. Thus the nearest-neighbor separation is proportional to cluster mass by

$$R_{nn} = N^{1/3} \tag{1.13}$$

The scaling exponent for a cluster dense diffusional system is then

$$\lambda = \frac{1}{D_f} - \frac{1}{3} \tag{1.14}$$

and using the expected value of $D_f = 1.8$ the scaling exponent becomes $\lambda = 0.22$

Now that it has been shown for both ballistic and diffusional cluster-cluster aggregation that the aggregation kernel is a homogenous function with the exponent λ, simplifications can be made to the Smoluchowski equation that yield helpful expressions. First we work under the assumption that the aggregation is between like-sized clusters, then the Smoluchowski equation becomes

$$\frac{dn_N}{dt} = -n_N^2 K(N, N) \tag{1.15}$$

While this assumption may seem unphysical, the resulting expressions do a good job of describing real world systems. Since K is homogeneous, equation 1.15 becomes

$$\frac{dn_N}{dt} = -n_N^2 N^{\lambda} K(1,1) \tag{1.16}$$

The concentration of clusters of size N is equal to the number of clusters divided by the system volume

$$n_N = \frac{N_c}{System\ Volume} \tag{1.17}$$

and since the number of clusters equals $N_c = N_m / N$ then n_N becomes

$$n_N = \frac{n_1}{N} \tag{1.18}$$

Now equation 1.16 becomes

$$n_1 N^{-2} \frac{dN}{dt} = \left(\frac{n_1}{N}\right)^2 N^{\lambda} K(1,1) \tag{1.19}$$

or more simply put

$$N^{-\lambda} dN = n_1 K(1,1) dt \tag{1.20}$$

Integration yields

$$N(t) = [1 + (1-\lambda) K(1,1) n_1 t]^{\frac{1}{1-\lambda}} \tag{1.21}$$

which is rewritten as

$$N(t) = [t_0 + t]^z \tag{1.22}$$

Finally, we are left with a simple expression that scales with a kinetic exponent z, which describes how cluster size develops with time.

1.4 Scope and Organization of Dissertation

Aggregation of particles in aerosols and colloids is important in diverse fields [11]–[13], [8] such as materials science, biology, food science, and atmospheric science. Typically, aggregation in aerosols and colloids involves clusters hitting and sticking to other clusters in what is called cluster-cluster aggregation. We endeavor through computer simulation to gain

insight into the behaviors of common aerosol and colloidal systems. In this dissertation the structure and growth kinetics of several aerosol systems will be studied. Chapter 2 will cover the algorithms and computational techniques used to build aggregation simulations. The workings of each simulation are discussed to give the reader a basic idea of how the physics of aggregation is mimicked in the code. For those who may wish to code their own simulations chapter 2 covers, in more detail, some of the "tricks of the trade" that are essential in making the simulation run efficiently. In chapter 3 the shape of cluster-cluster aggregates made under random motion is discussed in detail. The effect of the "stringiness" or shape anisotropy on the fractal dimension D_f and scaling prefactor k_o is explored and it is found that shape anisotropy has no effect on D_f but has a strong influence on the scaling prefactor k_o. Chapter 4 introduces an analytical model that predicts the shape and fractal dimension of diffusion limited cluster-cluster aggregates. A restricted hierarchical model that makes on-lattice clusters in a side to end connecting growth scheme is used to test the analytical model against the diffusive cluster-cluster aggregation. The analytical model successfully predicts DLCA cluster shape and dimensionality. Chapter 5 describes the growth kinetics of cluster-cluster aggregation that takes place in the presence of gaseous media where the system starts with ballistic motion and then transitions to diffusive motion as the aggregates grow in size. It is shown that the kinetic exponent will crossover from the ballistic values to the diffusional values and the onset of this crossover is predicted by when the nearest neighbor Knudsen number reaches unity. In chapter 6 the system starts in a molten state and all collisions cause complete coalescence then the system cools and switches over to point contact cluster-cluster aggregation. Thus fractal clusters are composed of polydispersed monomers. The kinetics of both coalescence and cluster-cluster growth stages are analyzed. Additionally, the fractal dimension and kinetic exponent is found to agree with cluster-cluster

aggregates grown from monodispersed monomers. Chapter 7 involves a colloidal system that aggregates due to a short-range depletion potential and undergoes shears applied at various strengths. Without shear the system will develop fractal aggregates similar to DLCA. The shear is turned on at a certain time and the system grows under shear from then on. Regardless of how developed the system was at the initiation of shear, it is found that the applied shear rate is the determinant factor in the system's final state. Finally chapter 8 is summary and conclusion.

Chapter 2 - Simulation Methods

2.1 Introduction

This chapter goes over various methods and algorithms used to study aggregating systems. Most of the work done in the coming chapters use different types of off-lattice Monte Carlo methods which work by finding a particle's probability of movement based on particle size and the properties of the surrounding median. Brownian Dynamics codes are also employed and work by finding particle motion from integration of the Langevin Equation which uses random variables as a surrogate for thermal fluctuations. Also for those who wish to develop their own aggregation codes, some computational "tricks of the trade" are discussed in detail. Techniques that deal with complexities such as simulation box edge effects, cluster unfolding, and optimizing particle-particle force calculations are described.

2.2 Monte Carlo Cluster-Cluster Aggregation

In Monte Carlo simulations a simulation box of length L is filled with N_m spherical monomers to reach a desired volume fraction f_v. The monomers are placed at random positions inside the simulation box. If two monomers are initially placed in overlapped positions, one of the monomers is given new random coordinates. The number of clusters N_c is tracked throughout the simulation. Clusters include not only groups of joined monomers but lone monomers as well. This means at time zero $N_c = N_m$ and the number of clusters is decreased as monomers stick together.

Clusters are randomly picked with a probability P_{pick} from the list of N_c clusters then moved a distance d with a probability P_{moved}. The values of these probabilities are determined by the physical situations that are being simulated. The use of random selection over probability

distributions makes Monte Carlo simulations well suited to study physical systems that exhibit stochastic behaviors. Thus aggregation driven by random thermal fluctuations, such as the ballistic and diffusion type aggregation, is ideal to study with Monte Carlo simulations[14].

Ballistic Limited Cluster-Cluster Aggregation (BLCA)

In the presence of low pressure gas, particles will move in linear trajectories between collisions and cluster velocity is due to the equipartition of energy. The displacement for a cluster is

$$r = \sqrt{\frac{3k_B T}{N}}\, t \tag{2.1}$$

The displacement in simulation is written as

$$r = \sum_{i}^{N_c} d_i P_{pick}(i) P_{move}(i) \tag{2.2}$$

One time step in the simulation is N_c iterations of equation 2.2. Now what needs to be done is to pick values in equation 2.2 that would mimic the behavior in equation 2.1. One way to do this is to make each cluster have the same chance to be picked, $P_{pick} = 1/N_c$; the movement chance is set to $P_{moved} = N^{-1/2}$ to mimic the thermal velocity but to also insure any monomer that gets picked will always be moved and d is set to monomer diameter regardless of cluster size. A cluster's trajectories must be stored between iterations due to the cluster's ballistic motion. If two clusters collide they are merged into a single cluster that is given a new spherically random velocity vector. This BLCA method is a proven way to simulate aggregation in the Ballistic limit[15], [16].

Diffusion Limited Cluster-Cluster Aggregation (DLCA)

With only slight adjustments the simulation can be made to mimic aggregation under diffusional motion. The motion is found by the mean-square displacement

$$\langle r^2 \rangle = 6Dt \tag{2.3}$$

The mean-square displacement in the simulation is

$$\langle r^2 \rangle = \sum_{i}^{N_c} d_i^2 P_{pick}(i) P_{move}(i) \tag{2.4}$$

As in BLCA, the values of the variables in 2.4 are chosen in a way to mimic the physics of the real world. In the DLCA case d is set equal to one monomer diameter and $P_{pick} = 1/N_c$, just like in BLCA. To ensure monomers will always move when picked the probability of moving is set to $P_{moved} = D_N/D_0$ where D_N is the diffusion constant of a cluster of size N monomers and D_0 is the diffusion constant of a single monomer. Since diffusional motion can be thought of as a random walk, every time a cluster is moved it is assigned a new spherically random velocity.

2.3 Brownian Dynamics

In Mote Carlo simulations the monomers stick on contact and no outside forces other than the random thermal force can be applied, if a more rigorous treatment of the systems physical behaviors is needed then Brownian dynamics must be employed. In Brownian dynamics the motion of each monomer is solved for by integration of the Langevin equation

$$m\ddot{r}_i = -\nabla U - \Gamma \dot{r}_i + R(t) + F \tag{2.5}$$

Where m is the mass of the monomer, r is the position, U is the monomer's potential energy, Γ is the drag coefficient, R(T) is the stochastic thermal forces and F is any added external force such as shear. The Langevin equation is simply Newton's second law with both drag and stochastic

thermal forces applied. The thermal force R(T) is random and thus averages to zero and has a correlation function of

$$\langle R(t)R(t')\rangle = 6k_B T\Gamma\delta(t-t') \tag{2.6}$$

The potential U, generally has a cutoff distance so only those monomers in the close proximity need to be incorporated for the force calculations.

The Brownian dynamics algorithm works as follows; initially the monomers are randomly placed inside the simulation box and given a velocity from the Maxwell-Boltzmann distribution at the system temperature. Then the force for each particle is calculated, using the link-cell method for efficiency. Then the Langevin equation is integrated over time step Δt and the monomers positions are updated [17], [18].

2.4 Cluster-Cluster Brownian Dynamics

Cluster-cluster Brownian dynamics uses the Langevin equation to find the motion of individual clusters. Unlike Brownian dynamics in which individual monomer trajectories are found, the cluster is treated as a whole unit. Therefore the Langevin equation is written as

$$m_a\ddot{r}_i = -\Gamma\dot{r}_i + R(t) \tag{2.7}$$

where m_a is the cluster mass. Notice there is no potential in equation 2.7. Since the integration of equation 2.7 only deals with clusters and not here constituent monomers no monomer-monomer potential can be used. The clusters stick together upon collision. The advantage of using cluster-cluster Brownian dynamics over faster DLCA or BLCA type simulations is that the type of motion the clusters experience can change as the drag forces evolve with the system without any direct intervention from the programmer. Unlike the Monte Carlo methods where any change in cluster movement must be manually put in, which in turn requires some kind of insight into the

devolvement of the system before being implemented, cluster-cluster Brownian dynamics is ideal for systems that move into transition regimes where no one limiting set of rules is dominant [19].

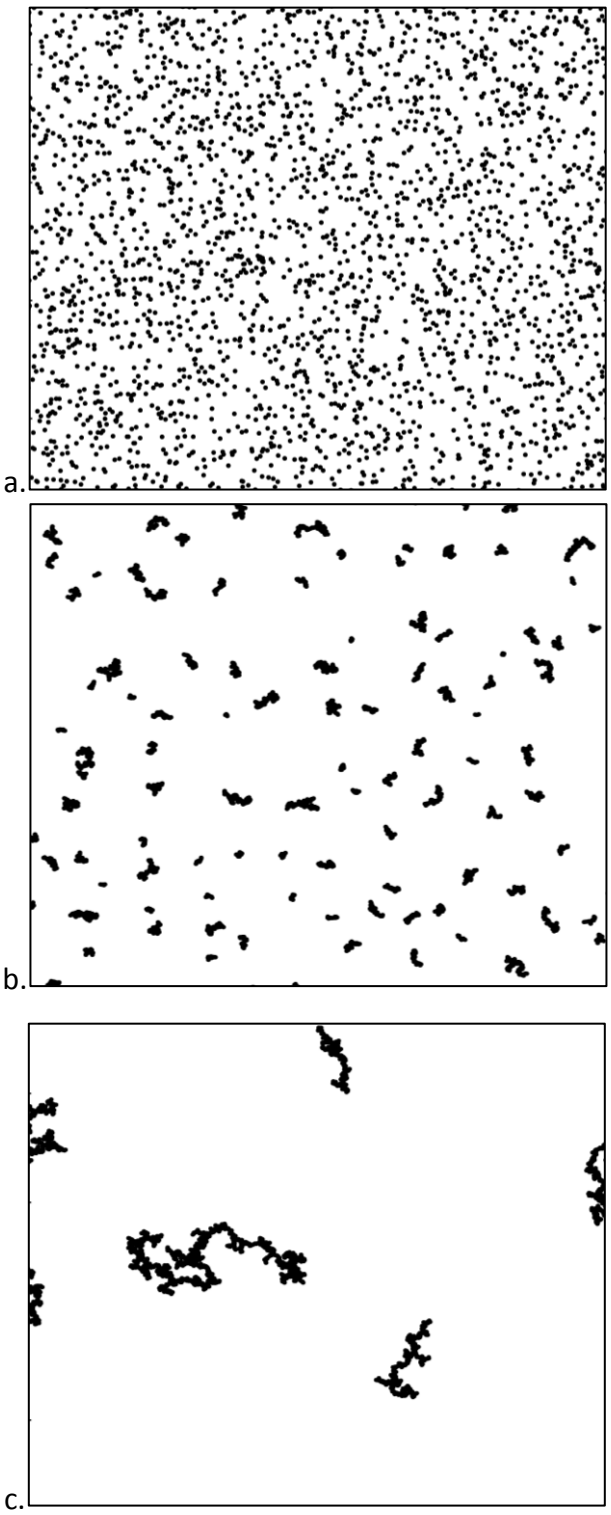

Figure 2.1 Snap shots of aggregation simulation at different times. (a) At earlier time the system is composed of monodispersed spheres. (b) As time passes small clusters form. (c) The system develops larger clusters at later times.

2.5 Link-Cell Method

Particles in simulation have short range potentials that at most extend a few monomer diameters before they can be considered zero. In the case of Monte-Carlo cluster-cluster simulations the potential is simply the condition the particles stick on contact. Therefore the potential does not need to be calculated between all other particles in the system but just those in the vicinity. Therefore it would be computationally costly and unnecessary to find all particle-particle interactions in the system. The system is broken up into several sub-volumes on a lattice with each cell of the lattice having a side length of L_c. In each sub-volume a list is made and maintained of all the particles that reside inside. When the net force acting on a particle needs to be calculated, the only particle-particle interactions that are needed are those in the home cell and all the neighboring cells. For example in Figure 2.2 the green particle needs only to make three calculations to find the net force instead of the 23 if the link-cell method were not used. Using the link-cell method makes it possible to have simulations with millions of monomers.

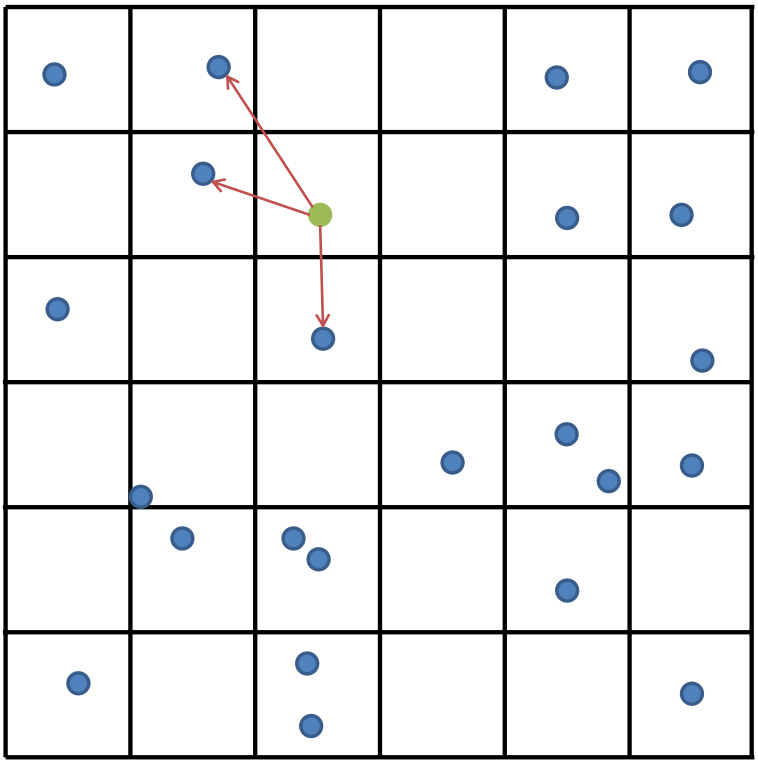

Figure 2.2. The link-cell method. The green monomer only has to do calulations on the three monomers in the nieghboring cells instead of all monomers in the system

The use of the link-cell method does require some computational overhead. For each cell a link list of occupying monomers must be kept and updated every time a monomer leaves or enters the cell. Each occupied cell has a monomer that is designated as the cell leader and one that is designated as the cell last. Other monomers in the cell are placed in lists called “NEXT” and “PREVOIUS”. The first entry in the NEXT list is the cell leader and then continues through all other monomers in the cell with the last entry being the cell last. The PREVIOUS list is the opposite of the NEXT list where the cell’s last is the first entry, the last entry is the cell leader and all other monomers are in between. Below is the pseudocode for initial monomer placement into cells.

For all cells set the First and Last to -1

For all monomers set NEXT and PREVIOUS to -1

For monomer i:

Find x_i, y_i, z_i

Find cell address (cx, cy, cz)

$cx = \text{int}(x_i / L_c)$

$cy = \text{int}(y_i / L_c)$

$cz = \text{int}(z_i / L_c)$

Is monomer i the first in cell?

If so:

First[cx, cy, cz]= i

Last[cx, cy, cz]= i

NEXT[i]= -1

PREVIOUS[i] = -1

If not:

Last_particle= Last[cx, cy, cz]

NEXT[Last_particle]= i

NEXT[i]= -1

PREVIOUS[i]= Last_particle

Last[cx, cy, cz]= i

As the particles are initially placed into the system the algorithm constructs the link-cell list. Note that -1 means that the spot in the list is empty. As the simulation runs monomers will leave their home cell and enter new ones. Below is the pseudocode for a monomer moving into a new cell.

Monomer i is moving from cell address cx_old, cy_old, cz_old to cell address cx_new, cy_new, cz_new.

old_first= First[cx_old, cy_old, cz_old]

old_last= Last[cx_old, cy_old, cz_old]

old_prev= PREVIOUS[i]

old_next= NEXT[i]

new_first= First[cx_new, cy_new, cz_new]

new_last= Last[cx_new, cy_new, cz_new]

Is First[cx_new, cy_new, cz_new] = -1 ?

If so:

First[cx_new, cy_new, cz_new]= i

Last[cx_new, cy_new, cz_new]= i

NEXT[i]= -1

PREVIOUS[i]= -1

If not:

Last[cx_new, cy_new, cz_new]= i

NEXT[i]= -1

PREVIOUS[i]= new_last

NEXT[new_last]= i

Is the old_first= i ?

If so:

First[cx_old, cy_old, cz_old]= old_next

PREVIOUS[old_next]= -1

Is old_last= i ?

If so:

Last[cx_old, cy_old, cz_old]= old_prev

NEXT[old_prev]= -1

Does i not equal old_last and old_first ?

If so:

NEXT[old_prev]= old_next

PREVIOUS[old_next]= old_prev

This algorithm always moves the new monomer to the end of new cell's list and it becomes the new "last". But if it moves into an empty cell, the monomer becomes both the first and last of its new home. Whichever spot the monomer had in its old cell the algorithm patches the hole and ensures the old cells link list remains continuous.

2.6 Periodic Boundary Conditions (PBC)

It is computationally intractable to simulate systems as large as the ones in experiments. Therefore, we employ a simulation box that has side length of L which is usually of the order of a few hundred monomer diameters. To avoid the inherent wall effects of such a small system we employ Periodic Boundary Conditions (PBC) to mimic an infinite system. Under PBC if a particle leaves the system it reenters on the opposite side. For example if a particle moves such that the x-coordinate is larger than L then the x-coordinate is subtracted by L. If one of the particles coordinates becomes less than zero then L is added to insure the particle remains inside the simulation box. Figure 2.3a shows an example of how the movement across PBC works. Using PBC the neighboring spaces to the simulation box are clones of the simulation box. In Figure 2.3b the center box is the simulation space while the neighbors are the clone spaces created under PBC, thus the apparent simulation space is infinite. Some care has to be taken when calculating distances between two objects. The space between the green and blue monomer in Figure 2.3b is not the dashed line that is completely inside the simulation box but the solid line that extends into the neighboring space. The implementation of PBC is as follows:

Pseudocode for PBC check of particle movement

Monomer new position is (x_new, y_new, z_new)

Is x_new greater or equal to L?

If so:

Set x_new= x_new- L

If not:

Is x_new less than 0?

If so:

Set x_new= x_new+ L

Repeat for y_new and z_new

Pseudocode for checking distance between two objects

Coordinates of object 1 are (x1, y1, z1)

Coordinates of object 2 are (x2, y2, z2)

$\Delta x = x1 - x2$

$\Delta y = y1 - y2$

$\Delta z = z1 - z2$

Is $|\Delta x|$ greater than $L/2$?

If so:

$\Delta x = |\Delta x| - L$

Repeat for Δy and Δz

Distance between two objects is $r = \sqrt{\Delta x^2 + \Delta y^2 + \Delta z^2}$

a.

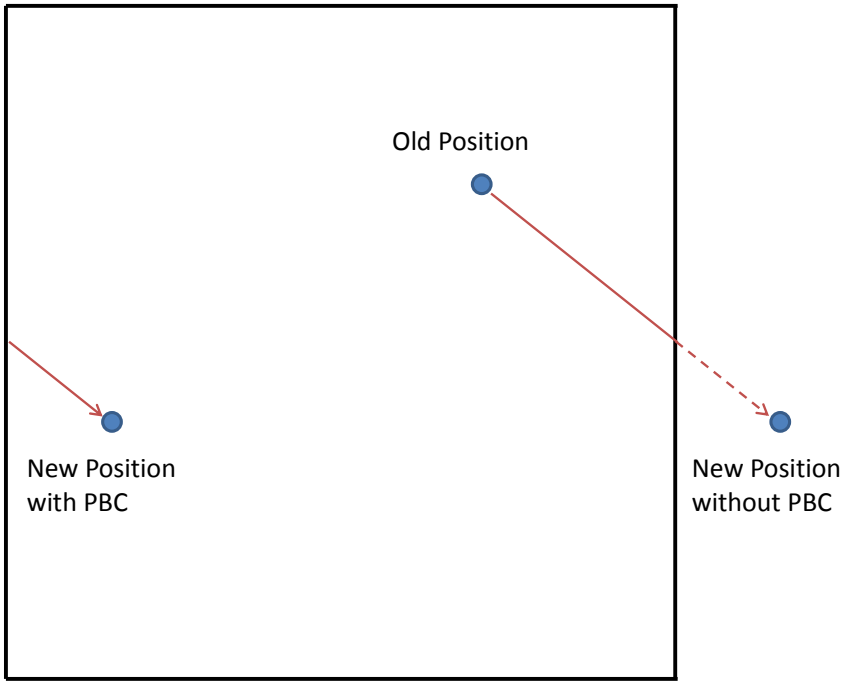

b.

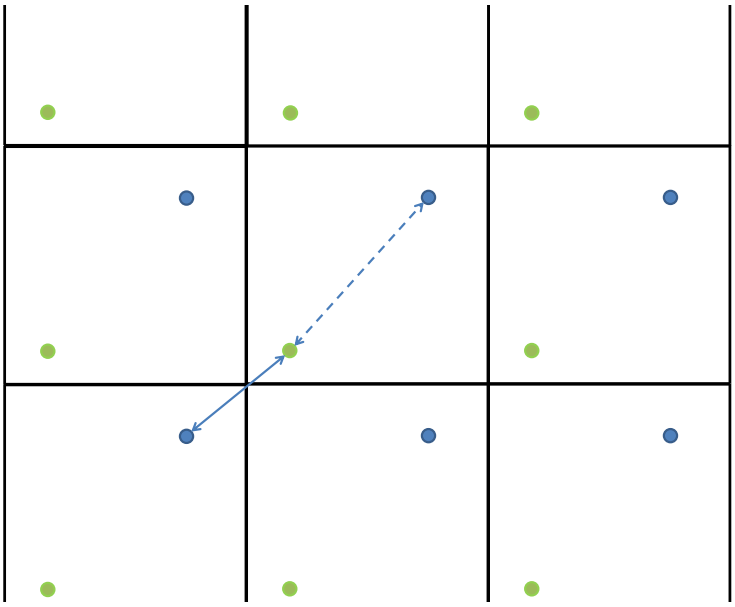

Figure 2.3 Periodic Boundary Condition (PBC). (a) Monomer movement across simulation box boundaries with and without periodic boundary conditions. (b) Cloned simulation boxes with PBC. The shortest distance between the two monomers can be across the boundary.

2.7 Cluster List

As monomers collide together they aggregate to form clusters. To extract important information from the clusters it is important to keep track of which monomers are in which cluster. To do this we use a cluster list that is very similar to the link-cell list described earlier. Each cluster has a monomer assigned as the “lead” and “last”. A list is made that starts from the lead and goes through all monomers in the cluster till the assigned last monomer. When monomers are initially placed in the simulation they are considered a cluster of one monomer and are assigned both the lead and the last positon. When two clusters stick together they form a new cluster and their cluster lists are combined. One cluster’s monomers are put at the end of the new cluster list. In the new cluster list the end cluster’s leader is assigned as the next to the last monomer of partner cluster and last of the end cluster is set to the last of the new cluster. The following pseudocode ensures that the cluster list remain continuous.

Initialization of cluster list
Set clust_lead and clust_last for ith monomer to i
Set clust_next for ith monomer to -1

Linking clust_1 and clust_2 clusters list together
Set clust_last of clust_1 to last_1
Set clust_last of clust_2 to last_2
Set clust_lead of clust_1 to lead_1
Set clust_lead of clust_2 to lead_2
Set clust_next of last_1 to lead_2
Set clust_last of all monomers in clust_1 to last_2
Set clust_lead of all monomers in clust_2 to lead_1

2.8 Unfolding

One needs to take care when making measurements on clusters that have moved across the periodic boundaries. As shown is Figure 2.4a the cluster has wrapped around the system due to PBC and complexities arise when making measurements such as finding the center of mass or radius of gyration. One must unfold the system to make measurements. Every monomer in the system has two sets of coordinates: the position of the monomer in the simulation box or folded coordinates and the unfold coordinates where all the clusters are continuous structures. The folded space is where the simulation runs, therefore the unfolded coordinates only need to be updated when data needs to be taken.

To unfold a cluster, first mark the cluster's lead monomer as unfolded and then measure the distance between the lead and the monomers of the cluster that are in the neighboring cells. If the measured distance is different when measured with the PBC method of finding distance from section 2.6 than the standard method, the monomer's unfolded coordinates are adjusted till both methods agree and the monomer is mark as unfolded. Then go down the cluster list till another monomer is found that is marked as unfolded. Measure distance between the monomer and those in neighboring cells, adjust coordinates, and mark the neighboring monomers as unfolded. If by the last monomer in the cluster not all monomers are marked as unfolded, start back with the cluster's lead monomer and repeat the process. To save time only compare monomers marked as unfolded to those marked as folded. The unfolding process will take a cluster like in Figure 2.4a and adjust it to Figure 2.4b. The pseudocode for cluster unfolding is as follows:

Mark clust_first as unfolded

Set clust_first as home_monomer

Loop though clust list

Cycle though monomers in neighboring cells and find those in cluster. Set neighbor monomer as check_monomer

If only one monomer between home_monomer and check_monomer is set to unfolded

If true, then adjust folded monomer's coordinates and mark it as unfolded

Set the next in cluster list to home_monomer

End loop when it reaches the last monomer in cluster

If not all monomers in cluster are unfolded then go through the loop again.

a.

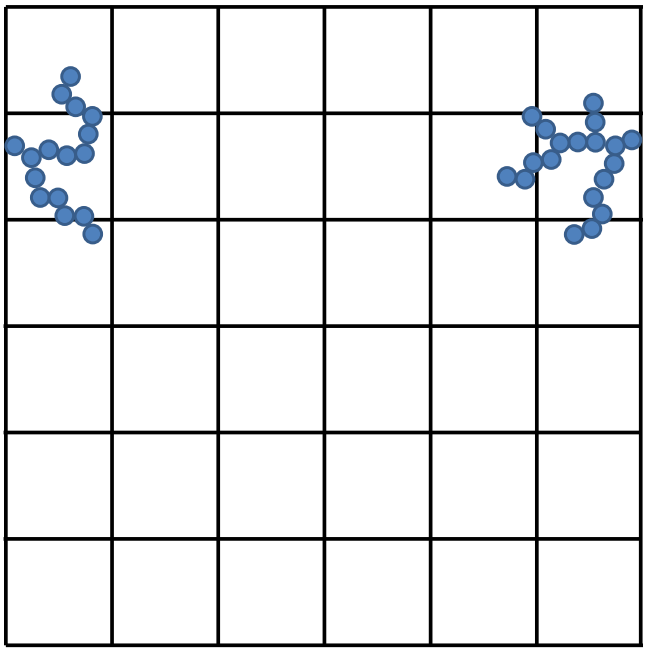

b.

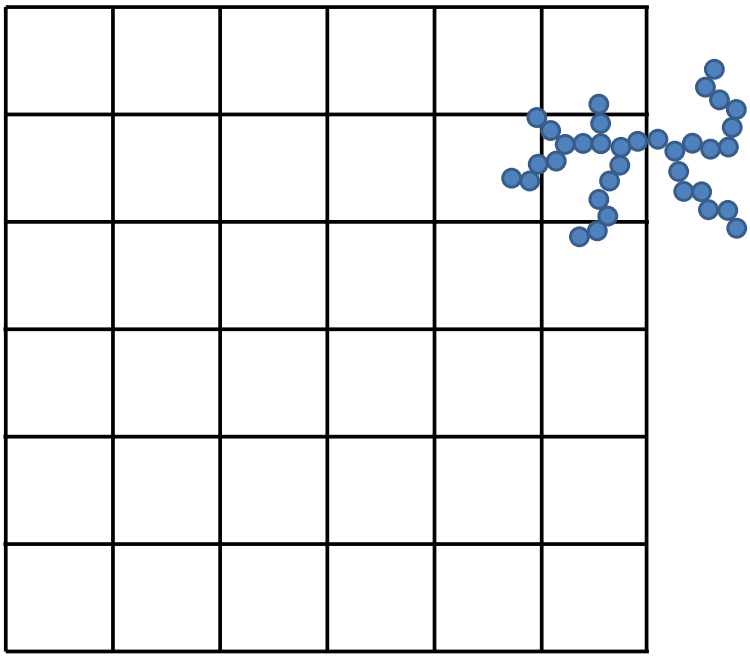

Figure 2.4 System unfolding. (a) example of cluster that has moved into the periodic boundary. (b) cluster after unfolding.

Chapter 3 - Diffusion Limited Cluster-Cluster Aggregation: Scaling Prefactor and Shape.

3.1 Introduction

This work was motivated by recent experiments of soot formation in premixed flames where a minority population of the "stringy" aggregates is found to have a fractal dimension as low as 1.2 instead of the DLCA value of 1.8 [20]. This led to the question: is there a distribution of fractal dimensions in a given ensemble of aggregates and does shape anisotropy or "stringiness" of clusters control the fractal dimension? To answer that question we present the results of our research into the shape of aggregates made in aerosols and colloidal systems. Typically aggregation in aerosols and colloids consist of spherical monomers colliding and sticking to form clusters. These resulting clusters then touch and stick to other clusters forming larger clusters and so on. The motion between collisions in this cluster-cluster aggregation system is most commonly diffusive. Clusters made under diffusion limited cluster-cluster aggregation (DLCA) are fractal in nature due to their scale invariant self-similar structure. The size of such aggregates is described by the radius of gyration R_g which is the root mean square radius. Since fractal aggregates display self-similarity, the size develops with a power law functionality. The number of monomers N in a cluster scales as a power law with R_g as

$$\mathrm{N} = k_0 \left(\frac{R_g}{a}\right)^{D_f} \tag{3.1}$$

where, a is the monomer radius, D_f is the fractal dimension and k_o is the scaling prefactor. Equation 3.1is very useful in describing the morphology of fractal aggregates but does not address aggregate shape. How does the aggregate shape affect the parameters in equation 3.1?

3.2 Shape Anisotropy

The anisotropy or "stringiness" of an aggregate is explored in this chapter but to do that one needs to be able to quantify an aggregate's shape. Shape is quantified by first measuring the inertia tensor T and finding the eigenvectors and the corresponding eigenvalues [21]. For a three dimensional cluster of N discrete masses the inertia tensor T is

$$\mathrm{T} = \sum_{i=1}^{N} \begin{pmatrix} y_i^2 + z_i^2 & -x_i y_i & -x_i z_i \\ -x_i y_i & x_i^2 + z_i^2 & -y_i z_i \\ -x_i z_i & -y_i z_i & x_i^2 + y_i^2 \end{pmatrix} \tag{3.2}$$

The eigenvectors give the aggregate's principle axes and can be considered to point along the long axis, medium axis and short axis of the cluster. The smallest eigenvalue corresponds to the longest axis eigenvector and the largest eigenvalue corresponds to the smallest axis eigenvector. Aligning the cluster so the longest axis is along the z-axis and the shortest axis is along the x-axis diagonalizes the inertia tensor as follows

$$\mathrm{T} = \begin{pmatrix} R_1^2 & 0 & 0 \\ 0 & R_2^2 & 0 \\ 0 & 0 & R_3^2 \end{pmatrix} \tag{3.3}$$

and yields the principle radii $R_1 \geq R_2 \geq R_3$. The radius of gyration is related to the principle radii by

$$R_g^2 = \frac{1}{2}(R_1^2 + R_2^2 + R_3^2) \tag{3.4}$$

Shape anisotropy is defined as

$$A_{13} = \frac{R_1^2}{R_3^2} \tag{3.5}$$

and is a quantifiable measure of aggregate shape.

Simulations started with 10^6 monomers at a volume fraction of $f_v=0.001$ and aggregated under DLCA till the number of clusters in the system was $N_c=7000$ including lone monomers. Figure 3.1 shows the distribution of shape anisotropy in a semi-log plot. The distribution is asymmetric about a peak near 2.5 with a long, exponential tail extending to high values of A_{13} described by $n(A_{13})\approx\exp[-\mu A_{13}]$ with $\mu=0.45$.

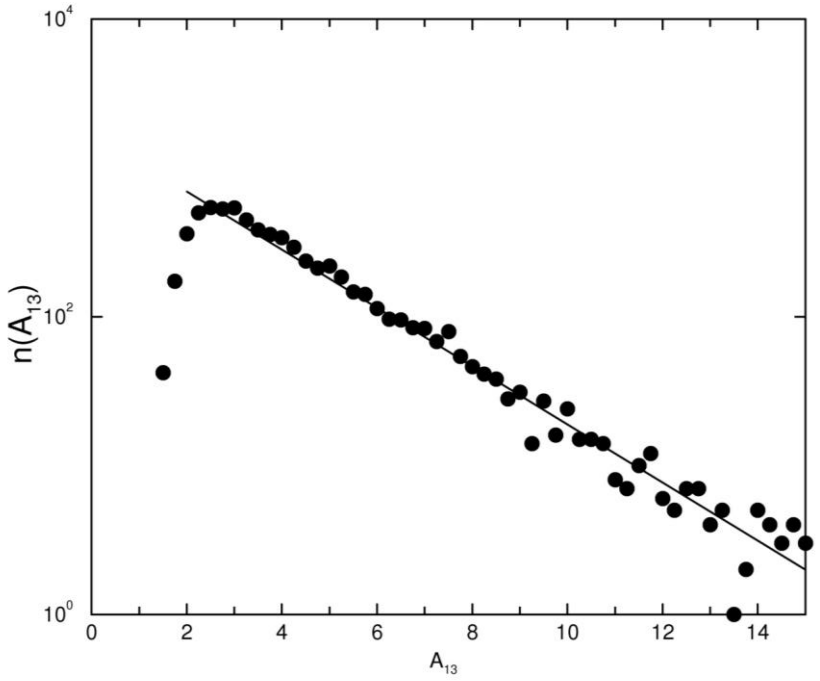

Figure 3.1 Number density $n(A_{13})$ of clusters with anisotropy A_{13}, for 3d DLCA model with monomer volume fraction of $f_v=0.001$. The peak of the distribution is near 2.5 with a long, exponential tail extending to high values of A_{13}. This exponential tail is described by $n(A_{13})\approx\exp[-\mu A_{13}]$ with $\mu = 0.45$.

3.3 Prefactor k_0 Versus Shape Anisotropy via R_g vs N

Clusters are divided into bins according to their A_{13} value, e.g., all cluster with $A_{13}< 3$ are in the first bin, cluster with $3 \leq A_{13} < 6$ are in the next bin and so on. In Figure 3.2 an ensemble method for measuring D_f is used in which N versus R_g/a (normalized radius of gyration) is plotted on a log-log plot. For each anisotropy range and for all the aggregates an

average R_g was found for every size N. Using equation 3.1 one finds D_f from the linear fit of the ensemble of points. The most striking feature of Figure 3.2 is each bin's ensemble runs parallel in the log-log plot thus D_f for each bin is the same independent of shape. Yet as A_{13} becomes larger the data points move lower, yielding smaller values for the prefactor k_0. We conclude that the aggregates in these simulations are well described by $D_f = 1.80 \pm 0.02$ and that k_0 is inversely proportional to shape anisotropy with an average value of $k_0 = 1.39 \pm 0.10$. This dependence can be understood by using equation 3.1. For a given N, as the cluster becomes more non-spherical, the radius of gyration increases, and then by equation 3.1 k_0 must decrease.

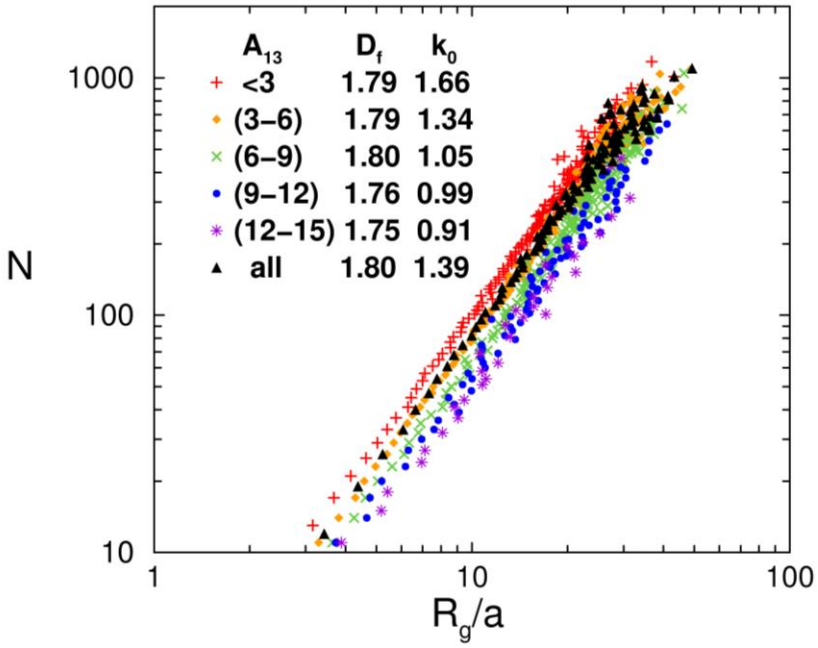

Figure 3.2 Number of monomers versus normalized radius of gyration for all the aggregates and groups of aggregates classified by anisotropy, A_{13}.The legend gives each bin's A_{13} range, prefactor k_0 and fractal dimension D_f. By the relation $N = k_0(R_g/a)^{D_f}$ fractal dimension, D_f is the linear fit to a bin's ensemble of points. Note that results for each bin runs parallel and goes as $D_f = 1.8$.

3.4 A ‘‘Bottom Up Approach’’ to Fractal Aggregate Structure

While the ensemble method uses a cluster’s overall mass and R_g to find the dimensionality and scaling prefactor, it is limited in that it ignores the structure of the aggregate at its smallest level, that of the monomer. By starting with the manner in which spherical monomers can pack in space we can take what we call a ‘‘bottom up approach’’ to the fractal aggregate structure. From this the monomer pair correlation function is derived after which an analytical formalism developed by Nicolai et al is followed to find relationships between the fractal dimension, prefactor, shape and monomer packing. The bottom up approach starts with the packing of spheres in space [22]. The number of spherical monomers of radius a in a volume V(r) is

$$\mathrm{N}(r) = \varphi\left(\frac{r}{a}\right)^3 \tag{3.6}$$

where φ is the packing fraction. For fractals, where the dimensionality is $D_f(\neq 3)$ we generalize this formulation to

$$\mathrm{N}(r) = \varphi\left(\frac{r}{a}\right)^{D_f} = \left(\frac{r}{r_0^*}\right)^{D_f} \tag{3.7}$$

This equation defines a rescaled monomer radius in the notation of Nicolai et al [22].

$$r_0^* = \mathrm{a}\varphi^{-1/D_f} \tag{3.8}$$

The monomer pair correlation function is the probability that another monomer center will be found a distance r from a given monomer center. In isotropic systems the correlation function g(r) is constrained by the normalization condition

$$\int \rho\, \mathrm{g}(r) 4\pi r^2 \mathrm{dr} = \mathrm{N} \tag{3.9}$$

where ρ is a constant density. In fractals, however, ρ is a function of r. One thus writes a working definition of g(r) as proportional to the average number of monomers in a shell of radius r and thickness dr.

$$\mathrm{g}(r) \approx \langle \frac{monomers\ in\ dV}{4\pi r^2 \mathrm{dr}} \rangle \tag{3.10}$$

Consequently the normalization becomes

$$\int \mathrm{g}(r) 4\pi r^2 \mathrm{dr} = \mathrm{N} \tag{3.11}$$

With this working definition of g(r) and with the self-similar nature of fractal aggregates, the monomer from which the pair correlation function is measured is completely arbitrary. The structure around each monomer will be on average the same so equation 3.10 is an ensemble average. With equations 3.7 and 3.10 and the proper normalization, the pair-correlation is

$$\mathrm{g}(r) = \frac{dN}{4\pi r^2 \mathrm{dr}} = \frac{D_f}{4\pi r_0^{*D_f}} r^{D_f - 3} \tag{3.12}$$

Equation 3.12 applies for clusters of infinite size, but for finite sizes the pair correlation function must have a cutoff function. It has become customary to assume a stretched exponential, which we will use here, to modify equation 3.12 to

$$\mathrm{g}(r) = \frac{D_f}{4\pi r_0^{*D_f}} r^{D_f - 3} exp[-(r/\xi)^{\gamma}] \tag{3.13}$$

Equation 3.13 introduces the stretching exponent γ and is consistent with Nicolai, Durand and Gimel except that we remove the rescaled monomer radius in favor of the actual monomer radius

and the packing fraction. It is important to note that beyond the two length scales a and ξ, the pair correlation function is specified by three parameters, D_f, φ and γ. The length scale ξ in the stretched exponential takes into account the finite size of the cluster. The stretched exponential implies an assumed spherical symmetry. The stretching exponent γ is a measure of how sharply the pair correlation cuts off at ξ; an infinite γ represents a sharp boundary. Real aggregates have diffuse boundaries and are not spherically symmetric. It is important to realize that the g(r) for a non-spherical object with a sharp boundary, a rugby ball for example, when rotationally averaged would appear to have a diffuse boundary hence have a cutoff function with a finite γ. This would also be true for the ensemble averaged g(r) for a set of rugby balls with random orientations. Thus it appears that the stretching exponent γ for an aggregate can have both an intrinsic source due to the diffuse nature of the surface and a source due to rotationally averaging. The later could be eliminated but at the expense of the additional complication of requiring a correlation function for all three spatial dimensions. We opt not to do this. Thus we anticipate that the stretching exponent γ will be related to shape anisotropy, a fact that will be demonstrated below.

The real space structure of the aggregate can now be calculated using

$$R_g^2 = \frac{2\pi}{N}\int g(r) r^4 dr \tag{3.14}$$

And in conjunction with equation 3.1 gives the prefactor

$$k_0 = \left[\frac{2\Gamma\left(D_f/\gamma\right)}{\Gamma\left[\left(D_f+2\right)/\gamma\right]}\right]^{D_f/2} \frac{\varphi D_f \Gamma\left(D_f/\gamma\right)}{\gamma} \tag{3.15}$$

Equation 3.15 shows that the prefactor is a function of three parameters, D_f, φ and γ. The reciprocal space structure of the aggregate is described by the structure factor which is the

Fourier transform of the pair correlation function and an important measurable quantity. For a spherically symmetric g(r) the structure factor is given by

$$\mathrm{S(q)} = \frac{P(q)}{N}\left[1 + 4\pi \int_0^\infty g(r) r^2 \frac{\sin(qr)}{qr} dr\right] \tag{3.16}$$

where P(q) is the form factor of the monomer. In this work we will study the regime in which q^{-1} is large compared to the monomer radius and P(q) = 1. Substitution of equation 3.13 into 3.16 yields for large q

$$\mathrm{S(q)} = \frac{b}{N}(q)^{-D_f}, \quad r_0^* \ll q^{-1} \ll \xi \tag{3.17}$$

where, in the notation of Nicolai et al [22].

$$\mathrm{b} = r_0^{*-D_f} D_f \Gamma\left(D_f - 1\right) \sin\left[\frac{\pi}{2}\left(D_f - 1\right)\right] \tag{3.18}$$

Equation 3.17 has a $1/\mathrm{R_g}$ dependence due to the limits $\mathrm{r_0^* \ll q^{-1} \ll \xi}$. The characteristic size ξ is related to $\mathrm{R_g}$ by equation 3.13 and 3.14. Equation 3.17 does not collapse to one trend at a fixed value of N but shifts on the x-axis based on $1/\mathrm{R_g}$. Using $\mathrm{R_g}$ as a normalization for the Fourier variable q leaves only the γ dependence in the coefficient of S(q). Use of equations 3.1, 3.8 and 3.18 in equation 3.17 yields

$$\mathrm{S(q)} = D_f \Gamma\left(D_f - 1\right) \sin\left[\frac{\pi}{2}\left(D_f - 1\right)\right] \varphi k_0^{-1} \left(qR_g\right)^{-D_f} \tag{3.19}$$

which will be useful below. Application of equation 3.15 gives

$$\mathrm{S(q)} = \left[\frac{\Gamma(D_f - 1)}{\Gamma\left(D_f/\gamma\right)}\right]\left[\frac{\Gamma\left(\left(D_f + 2\right)/\gamma\right)}{2\Gamma\left(D_f/\gamma\right)}\right]^{D_f/2} \gamma \sin\left[\frac{\pi}{2}\left(D_f - 1\right)\right] \left(qR_g\right)^{-D_f} \tag{3.20}$$

Notice that the structure factor has no φ dependence. The coefficient of the $(\mathrm{qR_g})^{-\mathrm{D_f}}$ depends only on $\mathrm{D_f}$ and γ the latter of which, as we will see, varies with the shape of the cluster.

3.5 Results

Values for the packing fraction φ and stretching exponent γ were found by fitting the pair correlation function g(r) of each individual aggregate to the analytical form of equation 3.13. The fit involved multiplication of g(r) by r^{3-D_f}. Then the intercept of this form at r = 0 yields the product of D_f and φ. Two examples are shown in Figure 3.3.

The small r limit of the pair correlation plots in Figure 3.3 yields the product of D_f and φ. Taking $D_f = 1.80$, the limits from the fits to ca. 100 aggregates yield a packing fraction of $\varphi = 0.68 \pm 0.03$, independent of the shape of the aggregate. Also packing fraction was measured by the application of equation. 3.19 on the same ca. 100 aggregates and was found to be the same, within one percent, as the pair correlation packing fraction. This reinforces the concept that φ describes structure at the small aggregate length scales whereas A_{13} describes aggregate structure at large length scales. It is interesting to note that this packing fraction value is very close to the value found for random packing of spheres in three dimensions. It is also similar to a previously determined value in work done to understand packing of spheres in non-integer dimensionality spaces [23]. The corresponding value of r_0^*/a is found to be 1.24 ± 0.03.

The two examples of Figure 3.3 also indicate that the shape, as quantified by the anisotropy parameter A_{13}, affects the stretching exponent γ. Analysis of ca. 100 aggregates yields the data in Figure 3.4 which shows γ as function of A_{13}. The concept that the stretching exponent would have both an intrinsic component, due to the aggregate surface structure, and a shape component, that appears upon rotationally averaging the aggregate, was anticipated above and is supported here.

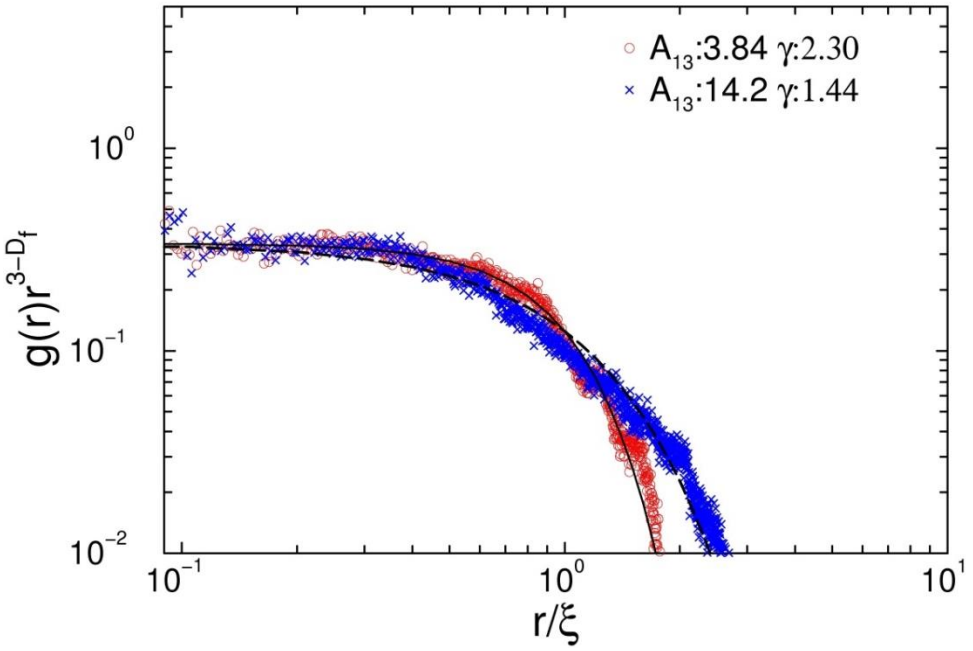

Figure 3.3 Pair correlation function g(r) of two N=500 aggregates with fits from equation 3.13. Notice the cluster with the larger A_{13} a less steep exponential decline.

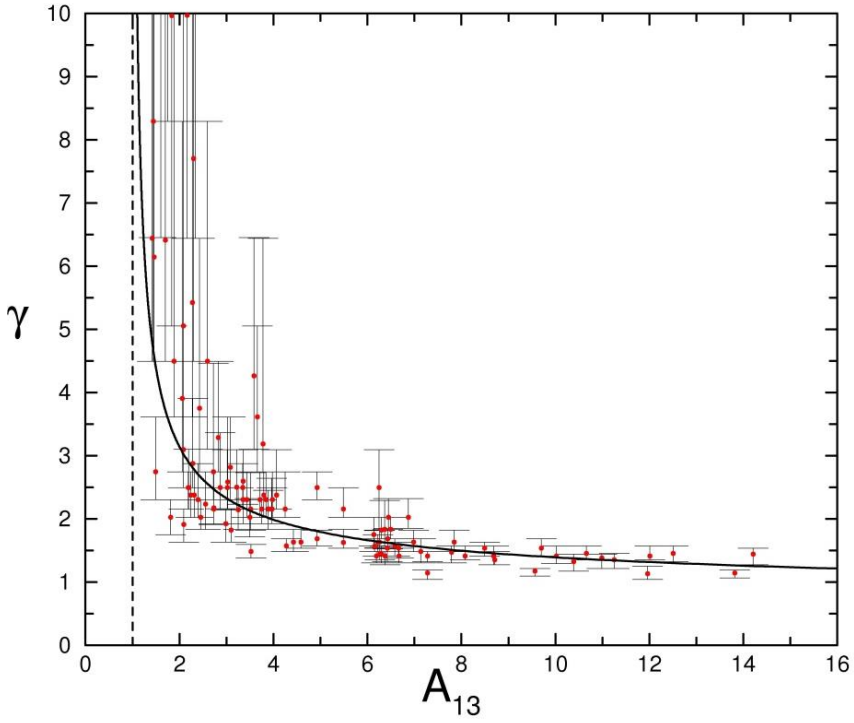

Figure 3.4 The stretching exponent γ versus anisotropy parameter A_{13}. Individual aggregates of N≥500 are plotted. Data points are individual DLCA aggregates. Error bars represent a range of gamma values for a given aggregate. The solid line is the combination of equation 3.15 and 3.23. The dashed line represents spherical clusters with the lowest possible value of A_{13}=1.

With φ=0.68 and $D_f = 1.80$, equation 3.15 provides a description of the how the prefactor k_0 changes with γ. This is tested against the simulation data in Figure 3.5. The limit of equation 3.15 can be evaluated as

$$\lim_{\gamma\to\infty} k_0 = \varphi\left(2 + {}^{4}/_{D_f}\right)^{D_f/2} \tag{3.21}$$

For $D_f = 1.80$ and φ=0.68, $\log_{\gamma\to\infty} k_0$=2.48. This limit is included in Figure 3.5.

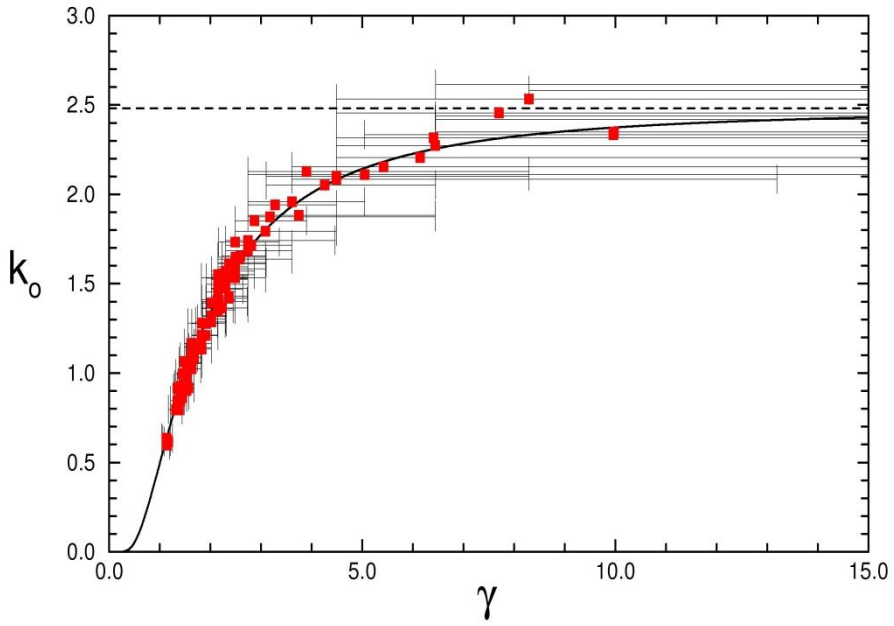

Figure 3.5 The prefactor k_0 versus exponent γ. Individual aggregates of N≥500 are plotted. Data points are individual DLCA aggregates. Error bars represent a range of gamma values for a given aggregate. The solid line represents equation 3.15 the dashed line is the limit of equation 3.21, $\log_{\gamma\to\infty} k_0$=2.48, both using φ=0.68 and $D_f = 1.80$.

Section 3.3 showed that the prefactor k_0 was a function of shape anisotropy, as specified by A_{13}, whereas the fractal dimension was not. Since A_{13} and γ are coupled together, equation 3.19 and 3.20 show that the coefficient of the fractal power law of the structure factor is a

function of shape anisotropy as well. In particular equation 3.19 for $D_f = 1.80$ and $\varphi=0.68$ yields

$$S(q) = C\left(qR_g\right)^{-D_f} = \frac{1.35}{k_o}\left(qR_g\right)^{-D_f} \quad (3.22)$$

This equation is tested in Figure 3.6 where the structure factor of clusters in various anisotropy (A_{13}) ranges is explored. Aggregates with $N \geq 50$ were divided into groups according to A_{13} as was done above for Figure 3.2. The structure factor for the clusters in each group were averaged and k_0 was found using equation 3.22. For all A_{13} ranges a fractal dimension of $D_f = 1.80$ accurately describes the data. The structure factors in Figure 3.6 show, once again, an anticorrelation between A_{13} and k_0 quantitatively consistent with that found in the real space analysis of Figure 3.2. This is demonstrated in Figure 3.7. A fit to all the individual clusters yields a quantitative description of this anticorrelation that can be best described as

$$k_0 = 2.48(A_{13})^{-0.45} \quad (3.23)$$

The system average prefactor was measured to be $\langle k_0 \rangle = 1.35$, hence the coefficient C = 1.00, as found previously [24]. Given this average prefactor, $D_f = 1.80$ and $\varphi = 0.68$, equation 3.15 yields $\langle \gamma \rangle = 2.02$, a value consistent with previous results [25], [26]. From equation 3.15 and 3.23 or equivalently the solid line in Figure 3.4, $\langle A_{13} \rangle = 3.86$.

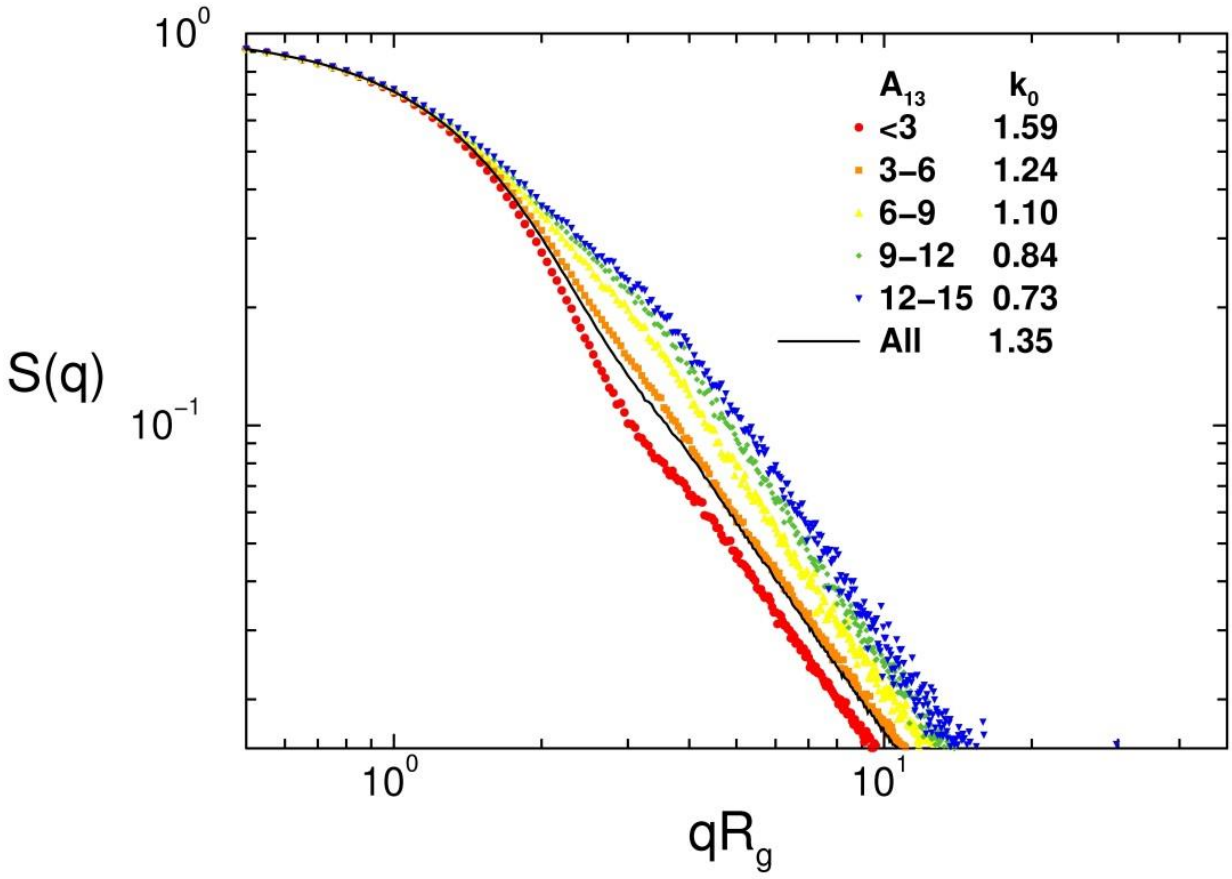

Figure 3.6 Structure factors for all the aggregates and groups of aggregates classified by anisotropy, A_{13}. Structure factors were calculated from squaring the Fourier transform of the spatial coordinates of the monomers and normalizing by N^2. Aggregates were divided into groups according to A_{13} and structure factor for the clusters in each group were averaged. Just like in Figure 3.2 all runs are parallel indicating a D_f=1.80. Also the inverse proportionality of A_{13} to k_0 is strongly evident.

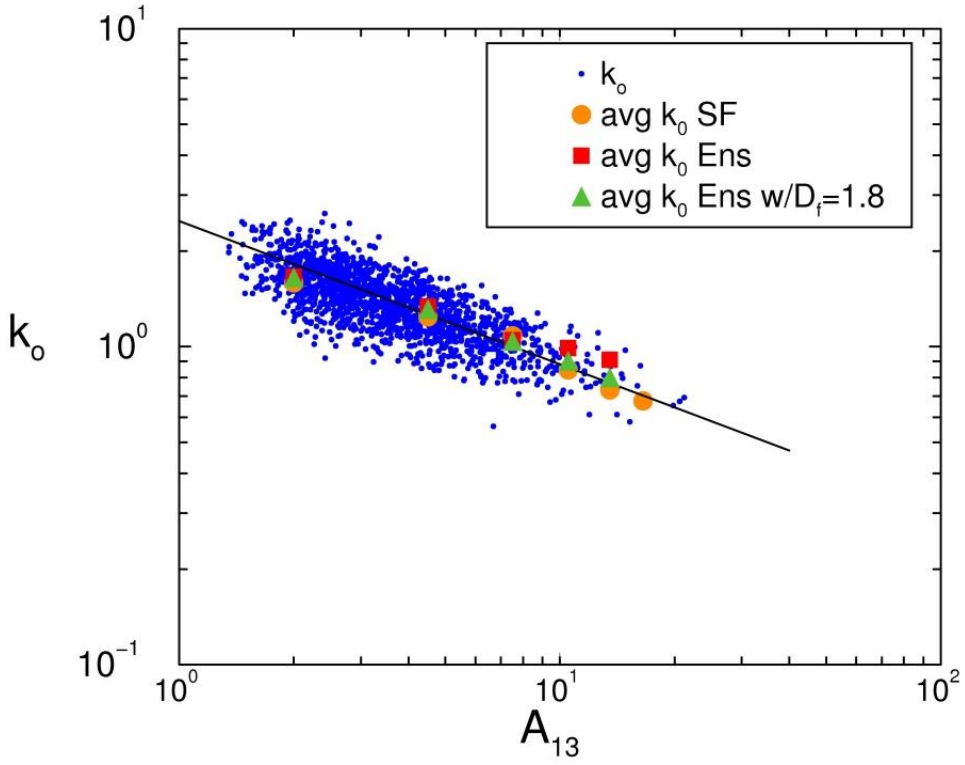

Figure 3.7 Large circles are the k_0 values for different A_{13} groups from structure factor (SF). The large squares are k_0 values for different A_{13} groups from the N versus R_g data of Figure 3.2 and triangles are the same data forced to D_f=1.80. Small circles are k_0 versus A_{13} for individual clusters and follow the trend line $k_0=2.48(A_{13})^{-0.45}$

3.6 Concluding Remarks

Numerous experimental studies of aggregates formed via DLCA have consistently found fractal dimensions of about 1.8 [5], [27], in agreement with the simulations presented here and many previous simulations [4], [25], [28]–[31]. On the other hand prefactors and shape have been measured less frequently. The only experimental prefactor work of which we are aware is for carbonaceous soot in flames which has been shown to have a fractal structure with dimensions on the order of 1.8 but with prefactors ranging from $k_0=1.23$ to well over 2 [32]–[34]. Unlike the idealized point contacting spheres of simulation, however, soot can show significant ‘‘necking’’ between connecting monomers. It has been proposed that this necking or

overlap is the reason for some of the soot prefactors to be larger than those of DLCA simulations [34], [35]. One possible patch to the theory here would be to try to quantify monomer overlap with a variable packing fraction φ. Then via equation 3.15, k_0 could be made bigger. At this time, however, we are uncertain how to quantify overlap and justify its use in equation 3.7.

The theoretical work presented here affirms that an adequate description of the morphology of a fractal aggregate is contained in the pair D_f and k_0. The fractal dimension D_f describes the scaling of mass with linear dimension and the prefactor k_0 contains aggregate shape information. However, we find that a more fundamental and perhaps more complete description of morphology lies with the three parameters fractal dimension, D_f, the monomer pair correlation function stretching exponent, γ, and the monomer packing fraction, φ. The fractal prefactor k_0 is a function of these three parameters via equation 3.15. The aggregate anisotropy A_{13} is directly related to the stretching exponent γ and thus an equivalent descriptor. We found that the packing fraction, like the fractal dimension, was constant. But it would seem to be wise to be wary that it, like the fractal dimension, might be a function of the aggregation mechanism, monomer overlap or, in simulations, whether the process is performed on or off lattice. These questions open avenues for future study. In addition, we have focused here only on irreversible aggregation with an infinitely deep potential well describing the monomer–monomer interactions. For short-ranged potentials with a finite but deep well, one can have a hybrid structure of fractal morphology (‘‘fat fractals’’) [36] leading to a different set of D_f, γ and φ. Finally, this work illustrates the effects of shape on both real space analysis, involved in the application of equation 3.1, and reciprocal space analysis via the structure factor.

Chapter 4 - The Restricted Hierarchical Model of Diffusion Limited Cluster-Cluster Aggregates and Divine Proportion Shape Invariance

4.1 Introduction

In the last chapter the shape and structure of clusters made under Diffuse limited cluster-cluster aggregation was discussed in detail. While DLCA does a good job of mimicking the kinetics and structure of aggregates in aerosol systems, it does not provide a complete analytic theory that can accurately predict the morphology of the aggregates. For example, why do DLCA clusters have fractal dimension of $D_f=1.8$? We review a simple analytical model, the Restricted Hierarchical Model (RHM), which can correctly calculate the fractal dimension of DLCA aggregates[37] and show that the RHM can correctly predict the prefactor and shape as well. Thus the simple RHM provides an accurate and complete three parameter description of DLCA aggregates with analytical predictions of the fractal dimension and shape. Also in this chapter we delve further into quantifying aggregate shape by using a method based on circumscribing rectangles and show that this yields a better description than the ratio of principle radii.

4.2 Review of the Restricted Hierarchical Method

The Restricted Hierarchical Method (RHM) builds monodisperse clusters in a hierarchical fashion as first proposed by Botet et al.[38]. We introduced a "restriction" to the model by only allowing side to end connections, as described below, between clusters[37]. In the simulation a dimer was made of two circular (spherical) monomers. This dimer was circumscribed with a rectangle. One of the rectangle's two longest sides, called the sides, and two shortest sides, called the ends, were chosen at random. The aggregate was cloned and the chosen end was linked with the clone's chosen side. Then the cloned aggregate was moved down the side of the original aggregate until a monomer-monomer connection was made, thus forming

a new aggregate. This process was repeated to make larger aggregates. At later stages, the aggregates were open (not compact) and the algorithm often needed to try all combinations of ends and sides before a connection could be found. This process continued until a target mass was achieved. Sometimes a connection could not be found and the aggregate was set aside before it reached a target mass. Randomly selecting the sides to be joined insured that the clusters had some variety in their structure. Examples of both d = 2, 3 DLCA and RHM aggregates are shown in Figure 4.1.

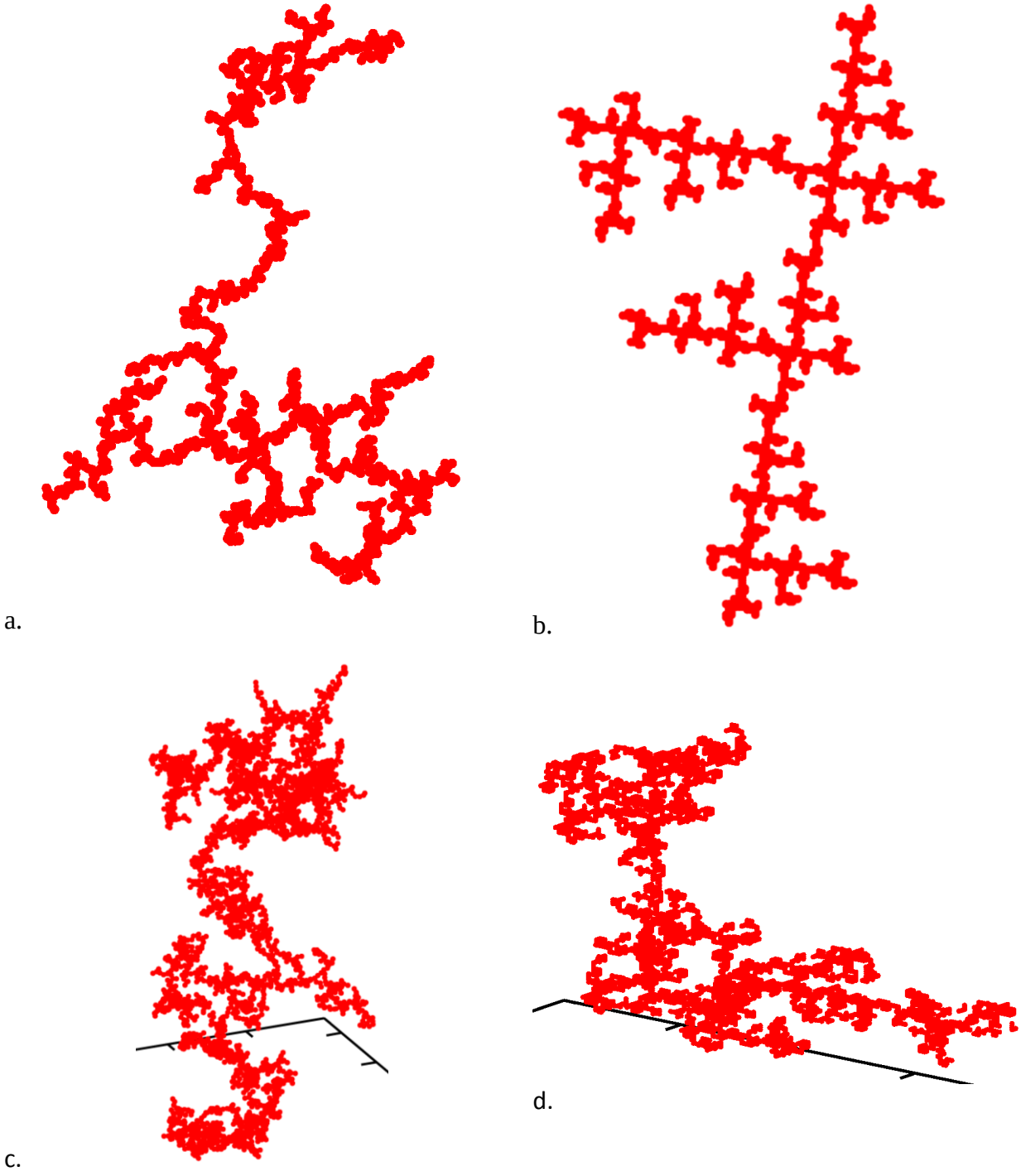

Figure 4.1 (a) 2d cluster made with diffusion limited cluster-cluster aggregation (DLCA). (b) 2d cluster made with Restricted Hierarchical Method (RHM). (c) 3d DLCA cluster. (d) 3d RHM cluster

4.3 Comparison of Shape Measurements

Before we discuss how the shape of RHM clusters compare to the shape of DLCA clusters we first must have ways to quantitatively measure shape, a task that can be difficult when dealing with randomly shaped aggregates. To quantify cluster shape we start by finding lengths along the object's principle axes and then take the ratios of those lengths. The principle axes were found by calculating the eigenvectors of the inertia tensor T [21], [39]. For a cluster of N discrete monomers the inertia tensor is given by equation 3.2

$$\mathrm{T} = \sum_{i=1}^{N} \begin{pmatrix} y_i^2 + z_i^2 & -x_i y_i & -x_i z_i \\ -x_i y_i & x_i^2 + z_i^2 & -y_i z_i \\ -x_i z_i & -y_i z_i & x_i^2 + y_i^2 \end{pmatrix} \tag{3.2}$$

and when dealing with two dimensional space we set $z_i = 0$. In the last chapter the lengths of these principle axes were taken to be the corresponding eigenvalues to the inertia tensor's eigenvectors. These eigenvalues are called the principal radii of the cluster. The ratios of the principal radii R_i were found to be $R_1/R_2 = 2.25$ for $d=2$ and as seen in Figure 4.2d, $R_1/R_2 = 1.03$, $R_2/R_3 = 1.53$ and $R_1/R_3 = 1.63$ for $d=3$. Note that for $d=3$ the ratios of consecutive R_i are not equal implying a surprising lack of symmetry for the shape. One would expect that since these clusters aggregate under random motion the ratios of their principle radii would show geometric behavior. That is, the distance from R_1 to R_2 would equal the distance from R_2 to R_3. To investigate the source of this asymmetry we calculated the principal radii for a $d=3$ rectangular solid with dimensions 1x2x4, a geometric progression. The resulting ratios are $R_1/R_2 = 1.085$, $R_2/R_3 = 1.84$ and $R_1/R_3 = 2.00$. This result shows a very similar asymmetry to

the d=3 DLCA aggregates despite the fact that the rectangle had geometric proportions. We conclude that the magnitudes of the principal radii are in general poor descriptors of shape.

The rectangular solid example suggests that aggregate shape could be well described by constructing a circumscribing rectangular solid with sides parallel to the principal radii, but with magnitudes determined by the condition that the circumscribing rectangle is the smallest one that contains every monomer of the aggregate. This certainly works for a rectangle. This circumscribing rectangle shape analysis was applied to the DLCA clusters to yield side lengths L_i

Figure 4.2a shows that the side ratio for d = 2 DLCA aggregates peaks at $L_1/L_2 = 1.63 \pm 0.34$ (widths determined via lognormal fits). This value is very close to the classical Divine Proportion (the Golden Mean) [40], [41] as indicated by the arrow. Figure 4.2b shows that for *d* = 3 DLCA the ratios of circumscribing rectangle consecutive sides are peaked at $L_1/L_2 = 1.46 \pm 0.27$ and $L_2/L_3 = 1.35 \pm 0.24$ and the ratio of the longest to shortest side has a peak at $L_1/L_3 = 2.14 \pm 0.27$. The near equality of the consecutive size ratios, within the uncertainty of distribution breadth, and the fact that $\sqrt{2.14} = 1.46$ implies that the intermediate side length is the geometric mean of the longest and shortest sides.

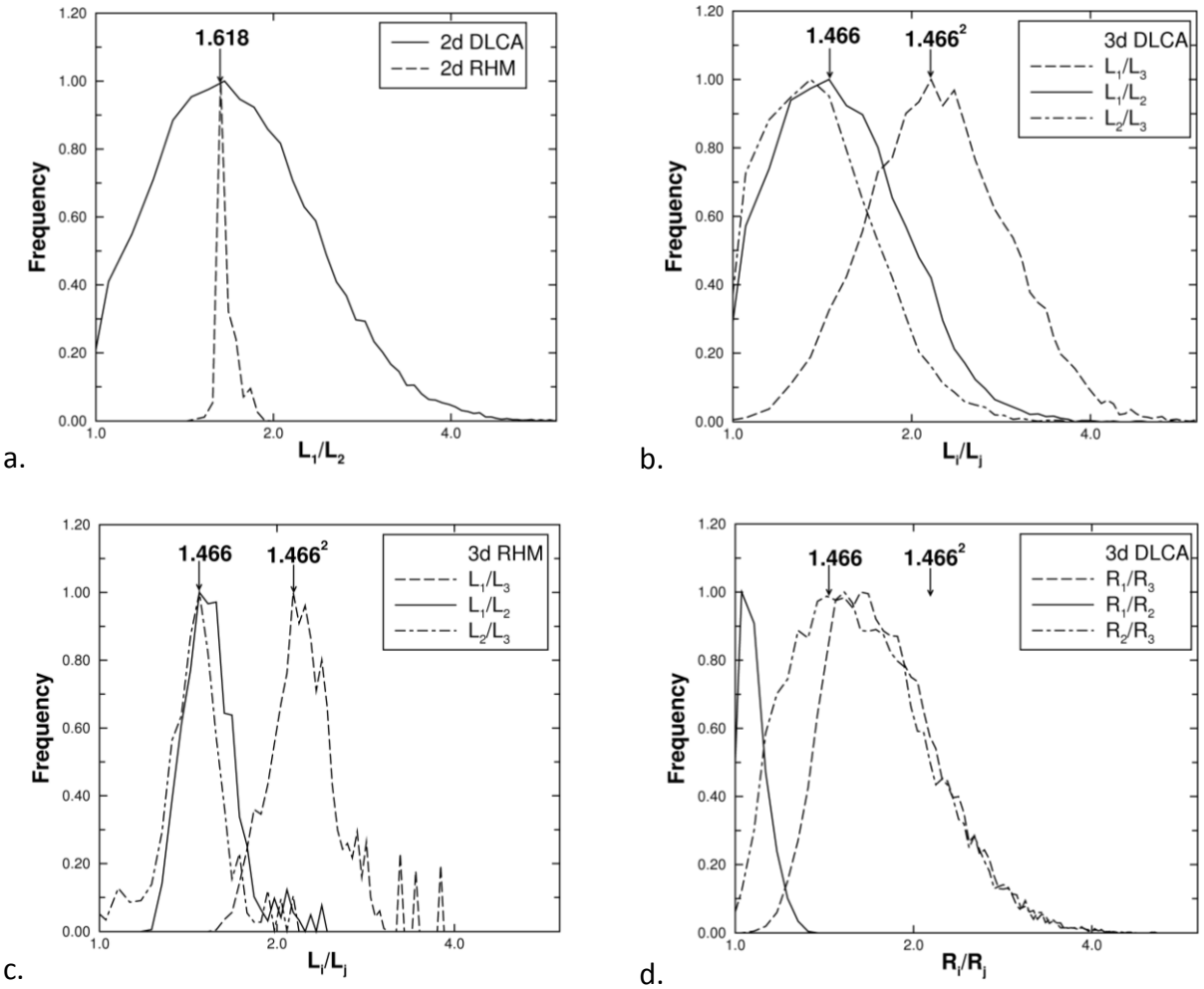

Figure 4.2 Shape as described by the ratios of principle lengths. (a)Distribution of L_1/L_2 for 2d DLCA and RHM. The distribution peak for both is 1.618, very close to the Golden Mean. (b) Distribution of L_1/L_2 , L_2/L_3 and L_1/L_3 for 3d DLCA. The ratio of consecutive lengths peak at 1.466 and L_1/L_3 peaks at 1.466^2. (c) Distribution of L_1/L_2 , L_2/L_3 and L_1/L_3 for 3d RHM. As in part (b) the peaks are at the 3d Divine Proportion of 1.466 for the ratio of consecutive lengths and $1.466^2$for L_1/L_3. (d) The ratios of the principle radii of the inertia tensor. The principle radii are not geometrically spaced and are not a good descriptor of shape.

4.4 Comparison between RHM and DLCA

As described above, the RHM assumes an on-lattice hierarchical growth in which aggregates of equal size come together to form larger aggregates. Thus the number of monomers in an aggregate after the nth iteration is 2^n. Monomers can have any shape and the lattice can have any symmetry. Here the concepts are illustrated with circular or spherical monomers on a

square lattice. Confined to a square lattice, the clusters can be circumscribed by a rectangular solid; the longest edge of this rectangle is defined as the side, the shortest as the end. End-to-end aggregations lead to straight chains with a fractal dimension of 1. Side-to-side aggregations lead to dense aggregates with a fractal dimension of d. But restriction to side-to-end aggregations leads to aggregates as drawn in Figure 4.1b for d=2 and Figure 4.1d for d=3. This side-to-end restriction is essentially the same as the T model restriction that Warren and Ball [42] applied to the hierarchical model. The dimensions of the circumscribing rectangles for d=2 aggregates follow the Fibonacci series [40], [41] with increasing size as illustrated in Figure 4.4

$$f_n = 1, 1, 2, 3, 5, 8, 13, 21, 34, 55, \ldots \tag{4.1}$$

In each RHM aggregation step, the linear dimensions of the aggregates increase by the ratio of consecutive Fibonacci numbers, which in the large size limit is the Divine Proportion φ.

$$\varphi = \lim_{n\to\infty} \frac{f_{n+1}}{f_n} = 1.618 \ldots \tag{4.2}$$

The number of monomers increases by a factor of two with each step. Thus the fractal dimension of these aggregates formed in two spatial dimensions D_2 is

$$D_2 = \frac{log(2)}{log(\varphi)} = 1.44 \tag{4.3}$$

For d spatial dimensions the Fibonacci series is generalized to

$$f_{n+1,d} = f_{n,d} + f_{n-d,d} \tag{4.4}$$

For example: d=1 equation 4.4 goes as $f_{n,1}$=1, 2, 4, 8, 16, ..., and is the geometric series; for d=3 equation 4.4 is $f_{n,3} = 1, 1, 1, 2, 3, 4, 6, 9, 13, 19, \ldots$. These d-dimensional Fibonacci series [37] are known mathematically as Narayana's cow sequences [43].

The ratio of consecutive d-dimensional Fibonacci numbers was defined as the d-dimensional Divine Proportion [37]

$$\varphi_d = \lim_{n\to\infty} \frac{f_{n+1,d}}{f_{n,d}} \tag{4.5}$$

For d=3 $\varphi_3 = 1.46557\ldots$. Equation 4.3 generalizes to

$$D_d = \frac{log(2)}{log(\varphi_d)} \tag{4.6}$$

Equation 4.6 successfully calculates the fractal dimensions for DLCA aggregates for d ≤ 6 including $D_3 = 1.815$ [37].

Another RHM rule is that no part of the circumscribing rectangles of two joining aggregates extend within or beyond the limits of the other. With this the RHM predicts the shape of the circumscribing d-dimensional rectangles to have consecutive side length ratios equal to the generalized Divine Proportion φ_d. Thus for d = 2 the side ratio is predicted to be $L_1/L_2 = \varphi_2 = 1.618$ (now the two dimensional Divine Proportion) and for d = 3 $L_1/L_2 = L_2/L_3 = \varphi_3 = 1.466$ (the three dimensional Divine Proportion). These predicted ratios are in excellent agreement with the peak values for both 2d and 3d DLCA aggregates shown in Figure 4.2.

Figure 4.2a and c show the frequency distributions of circumscribing rectangle side length ratios for the RHM simulation. The peaks are consistent with the analytical values of the generalized Divine Proportions. The distributions are narrower than those for DLCA, as expected. Nevertheless, the predictions of the RHM for the shape of the DLCA aggregates are very accurate.

Figure 4.3 shows N versus R_g/a for both the DLCA simulation (closed circles) and the RHM (open squares) hence tests the same scaling relation as in the last chapter

$$\mathrm{N} = k_0 \left(\frac{R_g}{a}\right)^{D_f} \tag{3.1}$$

Values for the prefactor and fractal dimension from fits to the data for both 2d and 3d are given in Figure 4.3 and Table 4.1 and agree well with previous work [4]–[6], [23], [27]–[29], [44]–[51]. The RHM simulation creates an ensemble of aggregates that are monodisperse in N, but for a given N are polydisperse in R_g. Despite this, the predictions of the model are essentially identical graphically to the DLCA simulation for both spatial dimensions. This is seen numerically for D_f and k_0 in Table 4.1 and displayed in Figure 4.3. The RHM accurately predicts the dimensionality, scaling prefactor and shape of DLCA aggregates and thus successfully describes the complete structure on DLCA aggregates.

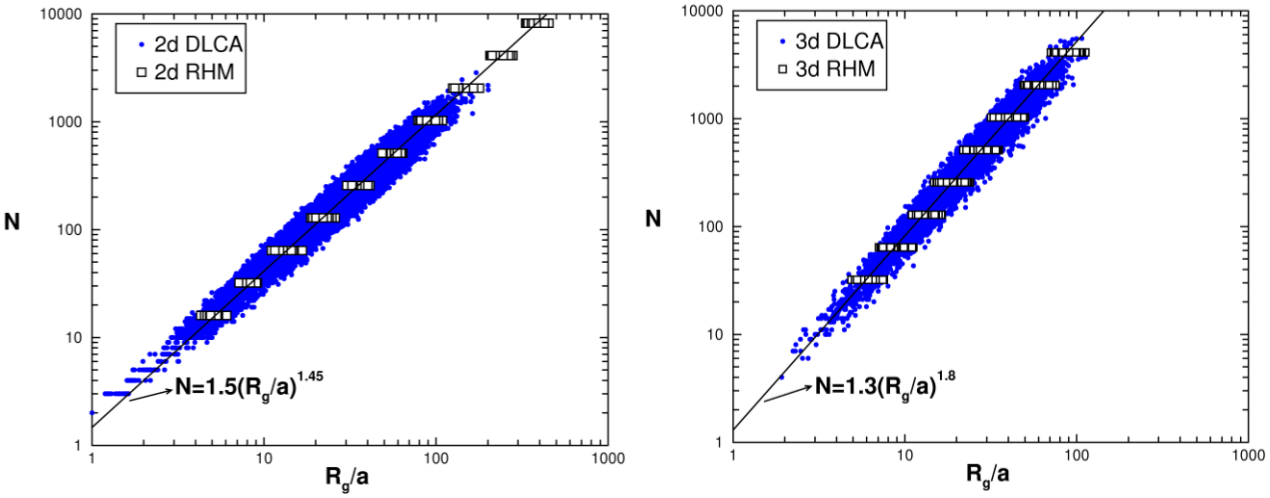

a. b.

Figure 4.3 N vs. R_g/a on a log-log plot for both DLCA and RHM. (a) 2d DLCA in closed circles and RHM in open squares. The data sets fall on top of each other and follow the guide line of $1.5(R_g/a)^{1.45}$. (b) 3d DLCA in closed circles and RHM in open squares. As in part (a), the data sets fall on top of each but follow the guide line of $1.3(R_g/a)^{1.8}$.

	2d DLCA Simulation	2d RHM Simulation	3d DLCA Simulation	3d RHM Simulation	2d RHM Analytic	3d RHM Analytic
k_0	1.50 ± 0.20	1.50 ± 0.10	1.30 ± 0.10	1.20 ± 0.10	---	---
D_f	1.45 ± 0.03	1.45 ± 0.03	1.80 ± 0.05	1.80 ± 0.05	1.440	1.815

Table 4.1 Values for the prefactor and fractal dimension from fits to the data for both 2d and 3d DLCA and RHM.

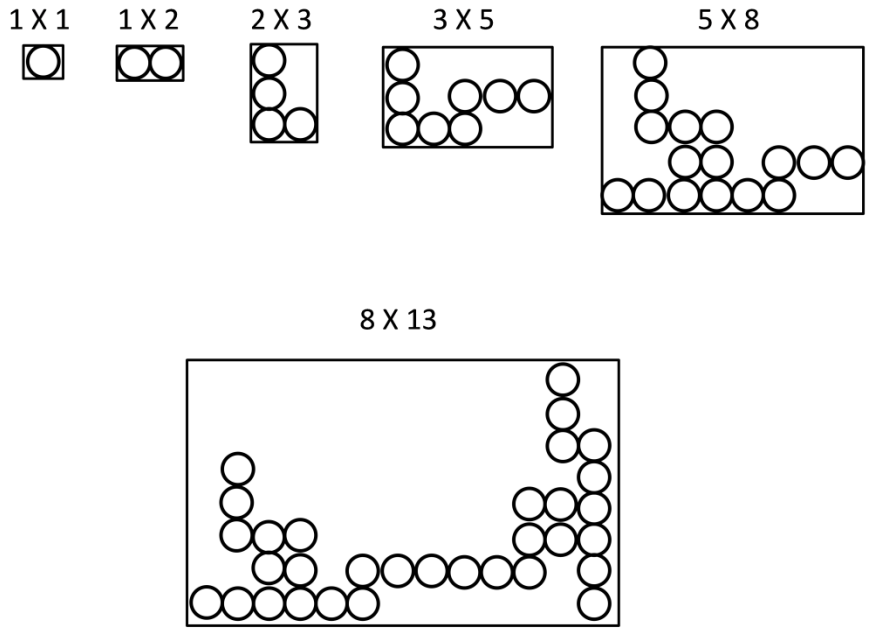

Figure 4.4 Several steps in the 2d RHM. The lengths of the circumscribing rectangle follow the Fibonacci series.

4.5 Concluding Remarks

The Restricted Hierarchical Model provides a complete, three-parameter description of DLCA aggregates to include an analytic calculation of the fractal dimension and aggregate shape. In its simplicity lies the essence of diffusion limited cluster aggregation. A remarkable outcome of the RHM and DLCA simulations is that the aggregate shape is described by the Fibonacci series and the Divine Proportion and their generalizations into an arbitrary number of spatial dimensions.

It is useful to ask why such a simple model is so successful. No doubt the statistical nature of aggregation helps the simple model. In reality two aggregates of different sizes come together from any direction. However, at any point during the aggregation of an ensemble of particles, collision of mean sized aggregates is the most common. Regarding the direction of approach, note that in two dimensions solely end-to-end collisions lead to D= 1 and solely side-to-side collisions lead to D = 2. The geometric mean of the two cases is 1.41, very close to D_2 (See also [52]). To continue, if during aggregation one makes the reasonable assumption that end-to-end and side-to-side occurred at ¼ probability and side-to-end at ½ probability then, the predicted fractal dimension would again be very close to D_2 for this simple extension of the present RHM. Similar arguments can be used for higher dimensions but are not really worthwhile. We have not made detailed comparison of the RHM to other forms of aggregation such as reaction limited and ballistic aggregation. These have fractal dimensions 5 to 10% larger than DLCA so the agreement is qualitative but not exact.

Chapter 5 - Crossover from Ballistic to Epstein Diffusion in the Free-Molecular Regime

5.1 Introduction

We investigate, through simulation, a system of aggregating particles in the free molecular regime that undergoes a crossover from ballistic to diffusive motion. In a gaseous medium the pressure, temperature, and molecular mass of the gas are determining factors of a particles motion. The initial particle volume fraction is also a factor in determining particle motion and can be adjusted over a large range, from the very dilute to very dense. The variation of these and other parameters leads to the limiting cases of either ballistic or diffusive type motion. All particles dispersed into a medium experience drag forces. If the particles are dispersed in a dense medium, the paths of the medium molecules impinging on the surface of the dispersed particle will be severely affected by those leaving the surface. This produces a "stick" boundary condition at the particle surface in what is known as the continuum regime and is described by the Stokes-Einstein drag. Stokes-Einstein drag is proportional to the particle's effective mobility radius, which is the geometric radius if the particle is sphere or the radius of gyration R_g for a cluster. If the particles are dispersed in a rarefied medium, the paths of the impinging medium molecules are essentially unaffected by those leaving the particle surface. This produces a "slip" boundary condition at the particle surface in what is known as the free molecular regime which has an Epstein drag. Epstein drag is proportional to the effective cross sectional area of the particle with a mobility radius squared functionality.

5.2 Classifying Aggregate Motion

The parameter that quantifies the continuum to free molecular regime change is the Knudsen number, $\mathrm{Kn} = \mathrm{mfp}/a$, where mfp is the mean free path of the medium molecules and a

is the radius of the suspended particle. When Kn→0, the system is in the continuum regime and when Kn→∞, the system is in the free molecular regime. Separate from frictional drag behavior of the median, the motion of the aggregate must also be classified. A common parameter used to describe aggregate motion is the diffusional Knudsen number Kn_D, which is the ratio of a suspended particle's persistence length, l_a to some other characteristic length. The persistence, $l_a$is the stopping distance used to calculate the Stokes number [53] when the velocity has the equipartion value. An aggregate's motion is taken to be on a straight line over a distance equal to its persistence length.

When $Kn_D \rightarrow \infty$ the persistence length dominates all other length scales and the motion is considered ballistic. When $Kn_D \rightarrow 0$ the persistence length is small compared to the system's other length scales and the motion is considered diffusive. The crossover between these two limits occurs when $Kn_D \approx 1$. When the system is cluster dilute, the only characteristic length scale is the linear size of the aggregates [31]. In this work we use a definition of Kn_D similar to that used by Rogak and Flagan [54] and Gopalakrishnan and Hogan [55], in the dilute limit

$$Kn_D = \frac{\sqrt{k_B T \mu_{ij}}}{\Gamma_{ij}\left(R_{g,i} + R_{g,j}\right)} \tag{5.1}$$

where k_B is the Boltzmann constant, T is temperature, μ_{ij} is the reduced mass between an aggregate and its collision partner, $R_{g,i}$ is the radius of gyration of the ith cluster and Γ_{ij} is the reduced drag coefficient between these two aggregates defined as $\Gamma_{ij} = \Gamma_i \Gamma_j / \left(\Gamma_i + \Gamma_j\right)$ where Γ_i is the drag coefficient of the ith cluster. The jth aggregate is the collision partner for a given cluster is assumed to be its nearest neighbor. This definition of Kn_D is equivalent to the ratio of the collision partners' reduced persistence length to their combined size.

As the system becomes more crowded, the nearest neighbor separation R_{nn} becomes another important length scale [31]. If the persistence length of the aggregate l_a is large compared to the nearest neighbor separation then the movement of aggregates between collisions would be on a straight line, that is, ballistic motion. But if $l_a$is small compared to R_{nn}, the aggregate will have to travel many such l_a's, which follow each other randomly, before it collides with another aggregate; then the movement is diffusive. This is illustrated in Figure 5.1 the where in part (a), the light shaded cluster moves ballistically whereas in part (b) it moves diffusively. With this physical picture in mind, we introduce a new diffusional Knudsen number based on the nearest neighbor separation as a characteristic length scale:

$$Kn_n = \frac{l_a}{R_{nn}} \tag{5.2}$$

To distinguish it from the traditional diffusional Knudsen number, we will refer this new one as the nearest neighbor Knudsen number from here on [31]. We anticipate that the nearest neighbor Knudsen number would be a better descriptor of the crossover from ballistic to Epstein diffusive motion as the system becomes cluster dense or when the mean persistence length an aggregate travels becomes close to the nearest neighbor distance.

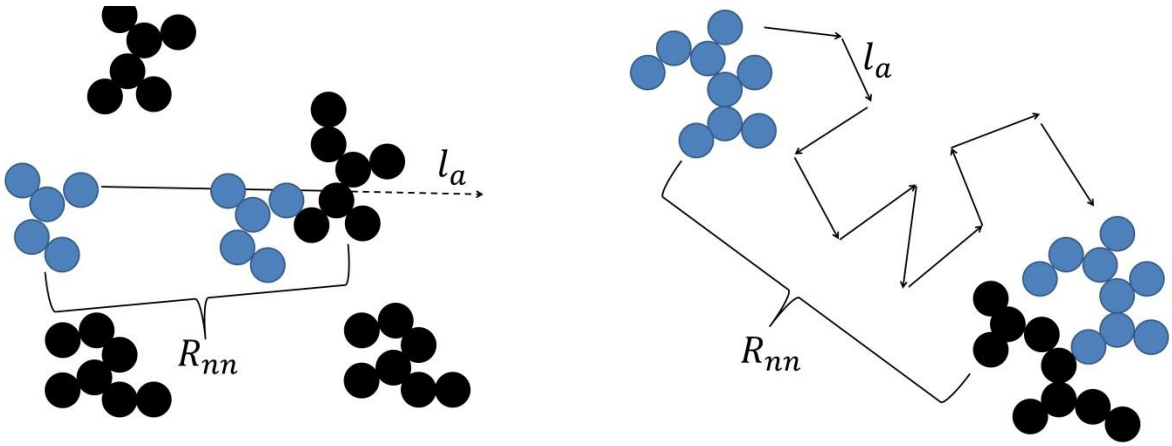

a. b.

Figure 5.1 (a) Illustration of a ballistic collision where the light shaded cluster does not make one full persistence length before colliding with its neighbor. (b) Illustration of a diffusive collision where the light shaded cluster makes several persistence lengths before colliding.

5.3 Simulation Methods

Two simulation models, Brownian dynamics and Monte Carlo cluster-cluster aggregation, are used in this chapter. While Brownian dynamics simulations have been used in the past to describe aggregation in the free molecular regime [55]–[58], they are computationally expensive. We have developed a Monte-Carlo (MC) method for the crossover study similar to ones used in the past for continuum regimes [31], [51]. This MC method has the advantage of being computationally very efficient. Both simulations are constructed so that the crossover from ballistic to Epstein diffusive motion occurs as aggregation proceeded and the aggregate size increased. While the simulations differ in the mechanisms of aggregate movement, they share similar starting points. All simulations start with 100,000 monomers of radius a, diameter $\sigma=2a$ and mass m_0 that are placed at random in a 3D simulation box. The desired volume fraction was

obtained by adjusting the box size. If a monomer was placed in overlap with another, it is given a new set of random coordinates. Work presented here was done at volume fraction of $f_v = 10^{-2}$, 10^{-3}, and 10^{-4} Periodic boundary conditions are in place to negate edge effects.

Brownian Dynamics

In this part, we integrate the Langevin equation for an aggregate:

$$m_a \ddot{r} = -\Gamma \dot{r} + R(t) \tag{5.3}$$

where m_a is the aggregate mass, Γ is the drag coefficient, R(t) the stochastic thermal force and r the position of a given aggregate center of mass. Aggregate mass can also be written as $m_a = N m_0$ where N is the number of monomers in an aggregate. The system is set to a constant temperature initially through the assignment of monomer velocities via the Maxwell- Boltzmann distribution. Solving equation 5.3 one finds [59]:

$$r(t) = t_c \left(v(0)\left(1 - e^{-\frac{t}{t_c}}\right) + \int_0^t \left(1 - e^{-\frac{t'-t}{t_c}}\right) \frac{R(t')}{m_a} dt' \right) \tag{5.4}$$

Here, the initial aggregate velocity is v(0) and the characteristic time, $t_c = m_a/\Gamma$ is a measure of how long an aggregate will move along a ballistic trajectory before it feels the influence from the medium.

Integration of equation 5.4 is done at time steps of $\Delta t = 0.1$ in reduced units of $2a(m_0/k_B T)^{1/2}$. Reduced units of monomer mass $m_0 = 1$, monomer radius $a = 1$ and $k_B T = 1$ are used to simplify the integration. When two aggregates collide they irreversibly stick, the total number of aggregates N_c is decremented by 1 and the new aggregate moves with a thermal velocity determined by equipartition.

Simulations presented here set out to model aerosol systems at low background gas densities often induced by high temperature and therefore are firmly in the free molecular drag regime. The free molecular drag coefficient is given as

$$\Gamma = 4\pi\delta P\sqrt{\frac{m_g}{3k_BT}}R_m^2 \tag{5.5}$$

In equation 5.5, δ is the accommodation coefficient, P is pressure, m_g is the mass of a gas medium molecule and R_m is mobility radius of the aggregate. Experiments and previous simulations have shown that the mobility radius for fractal aggregates is

$$R_m = aN^x \tag{5.6}$$

where the mobility-mass exponent x=0.46 [60], [61]. Now the drag coefficient becomes

$$\Gamma = 4\pi\delta P\sqrt{\frac{m_g}{3k_BT}}a^2N^{2x} \tag{5.7}$$

The ballistic motion persists over a distance given by the product of the characteristic time, t_c and thermal velocity $c=\sqrt{3k_BT/m_a}$. Thus, the persistence length is written as

$$l_a = \frac{3k_BT}{4\pi\delta P}\sqrt{\frac{m_0}{m_g}}a^{-2}N^{\frac{1}{2}-2x} \tag{5.8}$$

Notice that both the drag coefficient and persistence length have a power law dependence on N. Setting N=1 yields the monomer persistence length

$$l_0 = \frac{3k_BT}{4\pi\delta P}\sqrt{\frac{m_0}{m_g}}a^{-2} \tag{5.9}$$

Rescaling equations 5.7 and 5.8 by l_0 provides a more compact from of Γ and l_a

$$\Gamma = \frac{\sqrt{3k_B T m_0}}{l_0} N^{2x} \tag{5.10}$$

$$l_a = l_0 N^{\frac{1}{2}-2x} \tag{5.11}$$

From equation 5.10 it is clear that l_0 and N define the drag coefficient and therefore are necessary to solve the Langevin equation. Thus, l_0 along with f_v and number of monomers, becomes a primary input in the simulation. All l_0 values are given are in units of monomer diameter σ. Values of l_0=1, 10, 50, 200, 10,000 were used in this work. We will show that when l_0=1 the system acts as Epstein diffusion while l_0=10,000 leads to purely ballistic motion.

Monte Carlo Cluster-Cluster Aggregation

Instead of solving the Langevin equation to move the aggregates, the Monte Carlo CCA method picks an aggregate at random, calculates a probability of movement $P_m$to determine if the aggregate moves, and then increments time by $1/N_c$where N_c is the number of aggregates in the system including lone monomers. When the aggregate moves, it travels a distance of one monomer diameter σ. This model is standard for aerosol Monte-Carlo simulations in the continuum regime, where we differ is how P_m is calculated. In ballistic (BLCA) systems P_m is proportional to the aggregate velocity and is set as [31]

$$P_{m,B} = N^{\frac{1}{2}}. \tag{5.12}$$

For Epstein diffusion the probability of movement is proportional to the aggregate's drag coefficient Γ and is set as

$$P_{m,D} = N^{-2x}. \tag{5.13}$$

Our proposed crossover P_m must let an aggregate move ballistic on the scale of its persistence length l_a and diffusively on length scales larger than l_a. Also as an aggregate grows, its persistence length will decrease until $l_a = 1$ via equation 5.11. Since in our simulation the minimum step size is one, at the $l_a = 1$ point, P_m must also crossover from ballistic to diffusive. Our proposed $P_m$is a linear combination of inverse of $P_{m,B}$ and inverse $P_{m,D}$, that is, a harmonic sum of two probabilities.

$$P_m^{-1} = c_1 P_{m,B}^{-1} + c_2 P_{m,D}^{-1} \tag{5.14}$$

Normalizing so monomers have P_m=1 and crossover happens at l_a=1 equation 5.14 becomes

$$P_m^{-1} = \left(1 - \frac{\sigma}{l_0}\right) N^{\frac{1}{2}} + \frac{\sigma}{l_0} N^{2x} \tag{5.15}$$

where $1 \leq l_0 \leq \infty$.

We must note that the procedure for selecting P_m represented in equation 5.15 is purely *ad hoc*. However, it captures the physics of the aggregate motion. We will test it by comparing to the Langevin result. Equation 5.15 determines if an aggregate will move but does not say anything about the direction of movement. Since an aggregate must move on average a distance of l_a before it randomly changes direction due to the influence of the medium molecules, we calculate a probability of random direction change, P_r that is checked every time an aggregate is moved. We chose to use the inverse of l_a for the probability of direction change:

$$P_r = \frac{1}{l_a}. \tag{5.16}$$

As in equation 5.15, P_r is purely ad hoc but still captures the physics of the system. Care must be taken how time is incremented in this hybrid system where a cluster can move either ballistically or diffusively. The time, τ_D for an aggregate to move one monomer diameter by diffusion is given by the mean square displacement equation $\langle \sigma^2 \rangle = 6\tau_D k_B T/\Gamma$ which yields

$$\tau_D = \sqrt{\frac{m_a}{3k_B T}} \frac{\sigma^2}{l_a}. \tag{5.17}$$

Comparing the time to move ballistically one monomer diameter

$$\tau_B = \sigma \sqrt{\frac{m_a}{3k_B T}} \tag{5.18}$$

to τ_D and setting N=1 and l_0=1, the ratio of Equation 5.17 to equation 5.18 is

$$\frac{\tau_{B,0}}{\tau_{D,0}} = \frac{2}{\sigma} \tag{5.19}$$

In Monte Carlo simulations a cluster moves a distances of σ and time is incremented by $1/N_c$ but when the movement is diffusive the time scale needs to be normalized by equation 5.19.

5.4 Aggregation Kinetics

The kinetics of aerosol aggregation is governed by the Smoluchowski equation, which describes how the number concentration of clusters of size N monomers, $n_N(t)$, changes with time [10].

$$\frac{dn_N}{dt} = \sum_{i=1}^{N-1} K(i, N-1)\, n_i n_{N-1} - n_N \sum_{i=1}^{\infty} K(i, N) n_i \tag{5.20}$$

The aggregation kernel K(i,j) is the collision rate between aggregates made up of i monomers with aggregates of j monomers. K(i,j) is assumed to be a time-independent homogeneous function of particle size. To simplify the scaling we work under the assumption that the aggregation is between like-sized clusters, then the Smoluchowski equation becomes

$$\frac{dn_N}{dt} = -n_N^2 K(N,N) \tag{5.21}$$

Since K is homogeneous, one can write equation 5.21 as

$$\frac{dn_N}{dt} = -n_N^2 N^{\lambda} K(1,1) \tag{5.22}$$

where λ is the degree of homogeneity, and K(1,1) is the kernel for a monomer–monomer collision. The aggregate size N changes with time and the concentration can be written as,

$$n_N(t) = \frac{n_1(0)}{N(t)} \tag{5.23}$$

Then equation 5.22 becomes

$$N(t)^{-\lambda} dN = K(1,1) n_1(0) dt \tag{5.24}$$

Finally, integration yields

$$N(t) = [1 + (1-\lambda) K(1,1) n_1(0) t]^{\frac{1}{1-\lambda}} \tag{5.25}$$

or

$$N(t) \approx [t_0 + t]^z \tag{5.26}$$

with a kinetic exponent, z as first seen by van Dongen and Ernst [62]

$$z = \frac{1}{1-\lambda} \tag{5.27}$$

and

$$t_0 = \frac{z}{K(1,1)n_1(0)} \tag{5.28}$$

Expanding equation 5.26 for small time $t<t_0$ one finds that $N(t) \propto t$. After this, small transient time, there is a transition when $t \approx t_0$, and then ultimately at large time when $t>t_0$, the cluster size increases with power law $N(t) \propto t^z$. If the crossover happens during the linear transient regime, then information about the homogeneity will be absent. To avoid this below we simply graph average aggregate size $\bar{N}(t)$ versus $t+t_0$; a process that by equation 5.26 linearizes a double logarithmic graph.

5.5 Scaling Analysis of the Aggregation Kernel

The previous section discussed how aggregation governed by the Smoluchowski equation yielded an average cluster size that increased with time via a power law with the kinetic exponent. Here, we present a simple scaling analysis that describes how the collision kernel and its homogeneity determine the kinetics for different regimes of motion. Beginning with the general statement that K is proportional to the colliding particles relative collision cross-sectional area, A and relative velocity, v, we write

$$K \sim Av \tag{5.29}$$

Ballistic Regime

In the ballistic regime velocity $v \sim N^{-1/2}$ is due to equipartition of energy and since $R_g \sim N^{1/D_f}$ one finds from equation 5.29:

$$\lambda_{ballistic} = \frac{2}{D_f} - \frac{1}{2} \tag{5.30}$$

Using the accepted value of fractal dimension, D_f=1.9, in the ballistic limit [63] the homogeneity is found to be $\lambda_{ballistic}$=0.55 and via equation 5.30, hence the kinetic exponent is $z_{ballistic}$=2.2.

Epstein Diffusion Regime

In the diffusion regime, the characteristic velocity is $v\sim(\Gamma R_c)^{-1}$, where R_c is a characteristic diffusional length scale. In the dilute limit, the only length scale is R_c=R_g and from equation 5.29 one finds the homogeneity as

$$\lambda_{Epstein;dilute} = \frac{1}{D_f} - 2x \tag{5.31}$$

Aggregates in the Epstein diffusion regime have a fractal dimension of D_f=1.8 which yields $\lambda_{Epstein;dilute}$=-0.36 and $z_{Epstein;dilute}$=0.73. As the system becomes more crowded the relevant length scale becomes R_c=R_{nn}. The nearest-neighbor separation is $R_{nn}\sim N_c$ where N_c is the number of clusters in the system. The total number of monomers, N_m is constant and equals N_m=$\bar{N}N_c$, thus $R_{nn}\sim\bar{N}^{1/3}$and the homogeneity is

$$\lambda_{Epstein;dense} = \frac{2}{D_f} - \frac{1}{3} - 2x \tag{5.32}$$

In the Epstein limit, as the system becomes crowded, then, by equation 5.32 homogeneity is $\lambda_{Epstein;dense}$=-0.14 and the kinetic exponent is $z_{Epstein;dense}$=0.88.

5.6 Scaling Analysis of the Cluster Size Distribution

As aggregation proceeds in the system, the aggregate size distribution develops a scaling form given by $n(N)s^2=M_1\varphi(x)$where $n(N)$ is the number concentration of aggregates of size N, M_1 is the 1st moment of the size distribution and s is the average size [62]. The scaling variable is $x=N/s$ and the scaled distribution function, $\varphi(x)$ has the form $\varphi(x)=Ax^{-\lambda}e^{-(1-\lambda)x}$ for large sizes ($x > 1$) [64]. Thus,

$$n(N)s^2 = M_1 A x^{-\lambda} e^{-(1-\lambda)x} \tag{5.33}$$

5.7 Results

The aggregation kinetics for both Brownian dynamics and Monte Carlo simulations are shown in Figure 5.2a–f. The graphs shown the inverse number of clusters N_c^{-1}versus $t+t_0$ for various l_0's. Since the number monomers remains constant, N_c^{-1} is directly proportional to average cluster size. The constant t_0 was calculated by Equation 5.28. The monomer aggregation kernel K(1,1) and z used in equation 5.28 were decided based on the initial Kn_D and Kn_n.

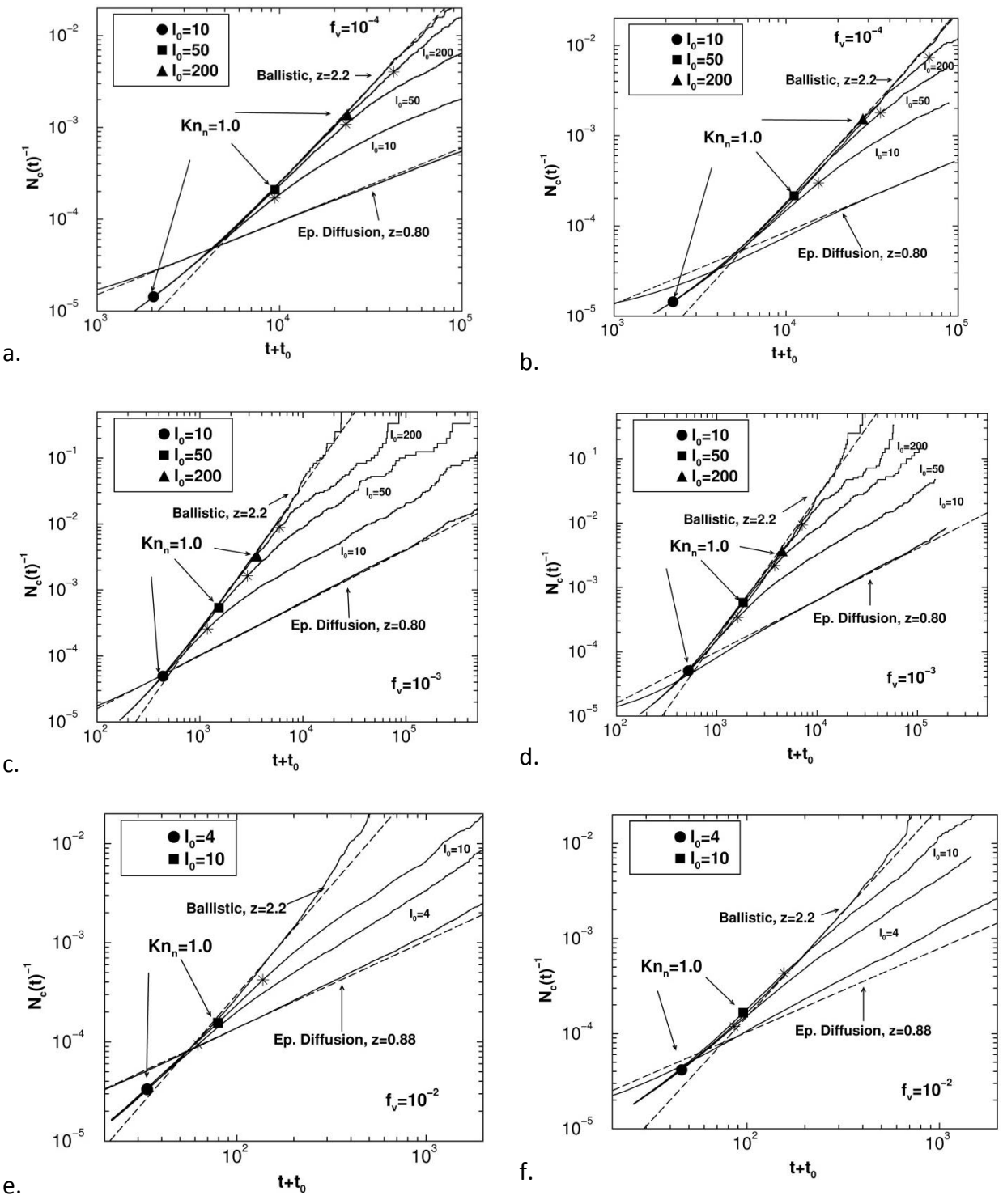

Figure 5.2 Inverse cluster count versus $t=t_0$. t_0 was found from equation 5.28. The lower dashed guide line has a kinetic exponent z=0.80, 0.88 and the upper guide line has z=2.2. The points where $Kn_n=1$ are marked and noted in the legend. The points where $Kn_D=1$ are noted as stars in their respective runs. (a) Monte Carlo simulation at $f_v=10^{-4}$ (b) Brownian Dynamics simulation at $f_v=10^{-4}$ (c) Monte Carlo simulation at $f_v=10^{-3}$ (d) Brownian Dynamics simulation at $f_v=10^{-3}$

(e) Monte Carlo simulation at $f_v=10^{-2}$ (f) Brownian Dynamics simulation at $f_v=10^{-2}$. Notice that in (e) and (f) the Epstein diffusion exponent is $z=0.88$ as expected when in the cluster dense regime. Also of note in (e) and (f) the trend has upward curvature do to the onset of gelation.

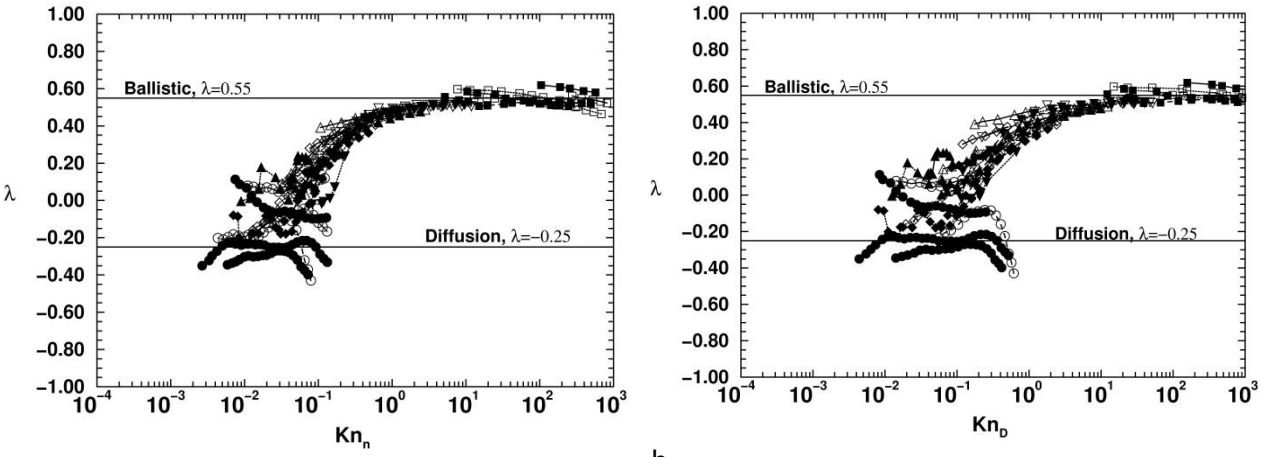

Figure 5.3 (a) Aggregation kernel homogeneity λ versus nearest neighbor Knudsen number Kn_n for all Monte Carlo and Brownian Dynamic simulations. (b) The diffusive Knudsen number Kn_D versus homogeneity λ for all Monte Carlo and Brownian Dynamic simulations. Both measurements show similar behavior and provide a means of detecting the crossover.

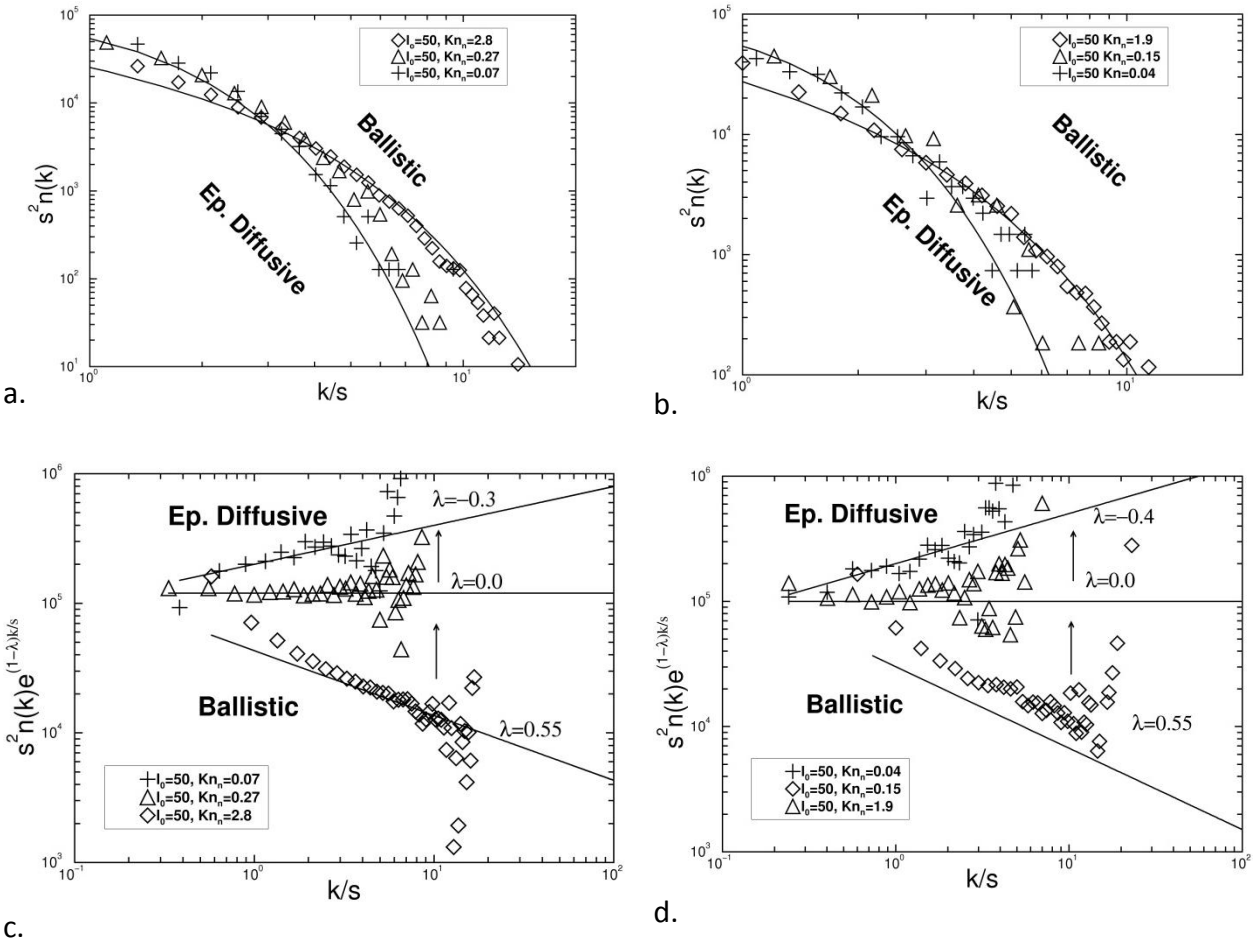

Figure 5.4 Aggregate size distribution from Brownian Dynamics with l_0= 50 and f_v= 10^{-3}. Lines represent fits from equation 5.33. The system starts off with ballistic λ then enters an intermediate regime during the crossover and finally at late time and small Kn_n reaches a diffusive λ. (a) Size distribution from Monte Carlo simulations; (b) size distribution from Brownian Dynamics simulations; (c) rescaled data from (a), here the homogeneity λ transition from ballistic to diffusive can be clearly seen. The system starts with ballistic homogeneity of λ=0.55±0.1 then changes to λ=-0.30±0.20, consistent to other values of λ reported for Epstein diffusion. (d) Rescaled data from (b), the system starts with ballistic homogeneity of λ=0.55±0.1 then changes to λ=-0.40±0.20, consistent with Epstein diffusion.

Diffusive and nearest neighbor Knudsen numbers were found for each aggregate by equations 5.1 and 5.2, respectively, then averaged to obtain Kn_D and Kn_n for the system. For runs with l_0=1 both Kn_D and Kn_n were less than unity and firmly in the diffusive regime, so values of diffusive K(1,1) and z were used to find t_0. All other runs started with larger Kn_D and

Kn_n and therefore ballistic values of K(1,1) and z were used to find t_0. When $l_0=1$, the system is entirely diffusive due to both Kn_D and Kn_n being less than unity and yields a kinetic exponent of $z=0.8$ for $f_v=10^{-3}$ and 10^{-4} and $z=0.88$ for the dense $f_v=10^{-2}$. Both these values are consistent with predicted values of $z=0.73$ for dilute Epstein diffusion and $z=0.88$ for dense Epstein diffusion, respectively [65].

At large l_0, Figure 5.2's parts all show for both types of simulation a kinetic exponent of $z=2.2$ as expected for ballistic motion at all f_v [31]. The intermediate values of l_0 initially follow the ballistic track then evolve to the diffusive z exponents. For all intermediate l_0 runs, the places where $Kn_D=1$ are marked by a star and places where $Kn_n=1$ are marked by symbols. While both Knudsen numbers fall within the crossover Kn_n does a better job of marking the beginning of the transition.

Figure 5.3 plots the aggregation kernel homogeneity λ versus either diffusional Knudsen number. By numerically finding z from the data in Figure 5.2 and using equation 5.27 to find λ, we compare Kn_n to λ in Figure 5.3a and Kn_D to λ in Figure 5.3b. Closed symbols represent data from Monte Carlo simulations and open symbols are data from Brownian dynamics. All runs follow the same trend with a ballistic like upper limit of $\lambda=0.55$ and an Epstein diffusional lower limit between $\lambda=-0.36$ for cluster dilute systems with $f_v=10^{-4},10^{-3}$ and $\lambda=-0.14$ for cluster dense systems with $f_v=10^{-2}$. A crossover present when either Knudsen number is in the 0.1 to 10 range.

In Figure 5.4a and b the size distributions at different times for the system at $l_0=50$ and $f_v=10^{-3}$ are shown for Brownian Dynamics and Monte Carlo simulations, respectively. The homogeneity is found from fitting equation 5.33. At early times when $Kn_n > 1$, the homogeneity is $\lambda=0.55\pm0.1$ consistent with ballistic motion, and at late time when $Kn_n < 1$, the system

moves to λ=-0.4$\pm$0.2 for the Brownian Dynamics runs and to λ=-0.3$\pm$0.2 for the Monte Carlo runs, both of which are in the range of previous reported values of λ=-0.36 to -0.14 for Epstein diffusion [31]. The transition of λ can be seen more clearly by scaling equation 5.33 by $e^{(1-\lambda)x}$. Figure 5.4c and d show the rescaled mass distributions at different Kn_n values for runs of l_0=50. Again as in Figure 5.4a and b, λ moves from a ballistic value to diffusive with changing Kn_n.

5.8 Concluding Remarks

We have performed simulations of the common yet previously unexplored aerosol situation in which the motion of the aggregates transforms from ballistic to Epstein diffusive while in the Free Molecular regime. Two algorithms were used. First, a slow but rigorous Brownian Dynamics method that solved for aggregate motion through the integration of the Langevin equation. Second, a less exact but faster Monte Carlo method that decides aggregate movement through use of an *ad hoc* probability of movement and probability of random walk. The probability of movement is a combination of the well-established probability of movements from ballistic and diffusive simulations and a probability of random walk insures aggregates on average move in a ballistic a distance of l_a. All simulations over all l_0's produced fractal aggregates of dimension 1.8 except for the very large l_0=10,000 that yielded fractal dimension of 1.9. Both systems were in good agreement with regard to the time evolution of the nearest neighbor and diffusion Knudsen number.

Volume fractions used went from the light $f_v=10^{-4}$ to a dense $f_v=10^{-2}$ to highlight the importance of R_{nn} as the dominant length scale in dense systems. To our surprise we found that at all volume fractions studied both nearest neighbor separation and aggregate size were equally adequate at describing the crossover. In the future, simulations must be done with both denser

and lighter systems to determine if both length scales do indeed remain markers of aggregation kinetics.

One physical situation in which the results of this chapter would apply is dense high temperature aerosols. Consider, for example, air at STP with a mean free path of 66 nm which means monomers of radius $a=10$ nm would experience Epstein drag. Using an accommodation coefficient of $\delta=1.36$ for N2 gas yields by equation 5.9 $l_0=30$ nm. If these monomers had a volume fraction of $f_v=10^{-6}$ then one finds $Kn_n=0.03$, placing the system in the Epstein diffusion regime. As the aggregates grow from these initial conditions, the system would move to the continuum regime which is not accounted for in our simulations. Raising the temperature to that of typical flame experiments, $T=2100$ K, the persistence length of the monomers grows to $l_0=210$ nm yielding a $Kn_n=0.21$, placing the system in the crossover regime between ballistic and diffusive motion, see Figure 5.3. Raising the volume fraction in the flame to $f_v=10^{-4}$ lowers the nearest neighbor separation which in turn gives a $Kn_n=1.00$, in the middle of the ballistic to diffusive crossover. These latter conditions have been studied experimentally in the past 15 years [66]–[68]. Finally, we remark that the reverse crossover from diffusive to ballistic aggregation can occur in dense systems near the gel point [30].

Chapter 6 - Aggregation with Consecutive Coalescence and Non-Coalescence Stages in Aerosols

6.1 Introduction

In this chapter, our focus will be on simulation of aggregation in a system where during the aggregation process particles at first coalesces to spherical particles and then subsequently the coalescence stops and the particles continue to aggregate to form ramified, fractal aggregates. This two stage model was motivated by experiments that created ultralow density, porous, high specific surface area materials via gelation of nanoparticles in the aerosol phase [69]–[71] . These aerosol gels are composed of carbon or silica. Carbonaceous soot aerosols were created by exploding a mixture of acetylene (C_2H_2) and oxygen in a closed, cylindrical combustion chamber while silica aerosol gels have been created in a similar manner with silane, SiH_4.

Experiments show that the primary particle size of the SiO_2 aerosol particles could be changed by changing the mass of the inert background gas [72]. With no background gas present, a thin, white "paint" of silica was found on the inner walls of the explosion chamber. This indicates that after their creation in the explosive reaction of silane and oxygen the hot silica molecules moved ballistically in the absence of an inert background gas and "splashed" on the chamber walls. When nitrogen was used as a background gas, particles formed that subsequently formed ramified aggregates leading to the formation of an aerosol gel. Helium as a background gas yielded larger particles, mean diameter of 100 nm compared to 16 nm for N_2 as a background gas. The particles with He as background gas were found to be more spherical than those for N_2 but the distribution of particle size was more polydisperse than for N_2. These particles also subsequently aggregate and form an aerosol gel. It is reasonable to conclude that aerosol gel formation is the result of a two-step process. First aggregation to complete

coalescence occurs during the brief, ca. 30 msec, high temperature, ca. 5000 K, explosion phase. This is followed by a second phase with no coalescence or sintering to form ramified, fractal aggregates which eventually gel (ca. 100 s). For the first stage it appears that the role of the inert background gas is to remove the large kinetic energy of the hot silica molecules and particles. These observations indicate that the hot, spherical particles of silica stay hot longer in the He than in the N_2 and thus coalesce upon collision for a longer time to form larger spherical particles. These experimental results engender the following question: What happens when during the aggregation process particles coalesce at first and then subsequently these coalesced clusters form ramified aggregates? Particle sintering, incomplete coalescence, was first described by Ulrich and Subramanian [73]. Studies by Koch and Friedlander [74]considered the relative time scales of sintering and aggregation but did not account for the possible ramified nature of the aggregates. Pratsinis and coworkers [75]–[79] have used both experimental and computational studies to describe the kinetics and resulting morphologies of the aggregates when both aggregation and sintering are at work during flame synthesis of particles. In more recent work, Schmid et al.[80] and Sander et al. [81] have studied detailed models of sintering of agglomerates by solving population balance equations. In these model calculations, sintering takes place over a long period of time. Although these models are well developed for studying sintering and aggregation in flame synthesis, they do not apply to our explosive aerosol generation process described above. In flame aggregation the system is at temperatures ranging from 1000 to 2500 K. In this temperature regime sintering occurs during aggregation. In our explosive generation method, on the other hand, the system starts with a gaseous precursor in the presence of an inert background gas. Then the precursor is ignited and explodes. Temperatures jumps to about 5000 K for a short time and then rapidly cools. At such high temperatures it is

assumed that sintering happens completely and coalescence is instantaneous. A short time later, on the order of 30 msec, the system goes through rapid cooling and sintering stops and aggregation proceeds to form ramified aggregates. The main parameter in determining how long the system stays in the high temperature regime is the background gas. We estimated that the temperature of the silica nanoparticles radiatively cools down to below 1000 K (when sintering practically stops) in times scales of the order of milliseconds. Thus a simulation model where the regime of coalescence and the regime of fractal aggregation separated in time scales is relevant for the experimental study mentioned in the chapter. We separate the time scales of sintering and aggregation by allowing first aggregation with complete sintering, i.e., coalescence to spherical particles, followed by aggregation with no sintering to yield ramified, fractal aggregates. We find that both the coalescence and ramified aggregation stages exhibit characteristic kinetics, morphologies, and size distributions that can be explained with mean field aggregation theory, and the end result is hybrid aggregates reflecting these stages. This model is the first attempt at modeling aggregates made from an explosive process. Though it is relatively simple compared to simulations used for flame aggregates, our model presents a non-material specific scaling description while capturing the essential features of aerosol gelation in the presence of different background gases.

6.2 Simulation Method

There were two distinct stages of the simulations. First was the coalescence stage. In the coalescence stage when monomers collided they merged into a coalesced spherical cluster with a volume equal to sum of the parent particle volumes. The second stage was canonical diffusion limited cluster-cluster aggregation (DLCA). The maximum number of particles used in the simulation is five million.

Coalescence Stage

In the coalescence stage, particles are hot and molten and are expected to move either ballistically [58], [82] or diffusively depending on the pressure of the background gas [31]. We model these movements in the following ways:

(a) *Ballistic Coalescence*: At a time t, we choose a coalesced cluster of size N randomly from the available number of clusters $N_c(t)$. The probability of movement (p) of that cluster is then calculated based on the thermal velocity of the cluster and one can write $\sim N^{1/2}$. This probability of movement is then compared to a random number between 0 and 1. If the random number is smaller than the probability of movement, the cluster is moved a distance of one monomer diameter σ. Whether the cluster moves or not, time is incremented by $N_c^{-1}(t)$ [5]. If the cluster happens to move it does so on a straight line in a random direction. This direction of movement stays constant till a collision occurs and at that point another direction is randomly chosen for the newly formed coalesced cluster to move also on a straight line.

(b) *Diffusive Coalescence*: The probability of cluster movement (p) for the diffusive case is defined as a cluster's relative diffusion constant $p \sim D_n/D_0$ where D_n is the diffusion constant of the cluster and D_0 is the diffusion constant of a monomer. In the continuum limit, this probability of movement can be written as $p \sim 1/R_g$ where $R_g$is the radius of gyration of the cluster.

Coalescence phase continues until a predetermined time t_D is reached. Beyond this point, the simulation moves over to the DLCA phase.

DLCA Stage

Simulation in the DLCA stage starts from the polydisperse system of coalesced clusters obtained at t_D. The motion is solely diffusive. A time step consists of randomly picking a ramified cluster of size N from the available $N_c(t)$ clusters. The probability of cluster movement (p) is based on the cluster's radius of gyration as $p \propto 1/R_g$ and as before, whether the cluster is moved or not time is incremented by $N_c^{-1}(t)$. If the cluster does move, it moves in a random direction for a distance of one monomer diameter σ.

6.3 Scaling Analysis

Scaling Analysis of the Aggregation Kernel

The Aggregation Kernel, K, describes the rate at which two clusters collides and is proportional to their relative collision cross-sectional area A and relative velocity, v, yielding $K \sim Av$, consistent with the units of $[L^3t]$. As we saw before, if one assumes that the cluster size distribution is approximately monodisperse, one can write the appropriate collision kernel as:

$$K \sim N^{\lambda} \tag{6.1}$$

Also the kinetic exponent z, which characterizes the power-law growth with time of the average cluster size, $N(t) \sim t^z$,is related to the homogeneity λ by:

$$z = \frac{1}{1-\lambda} \tag{6.2}$$

One typically writes this as $A \sim R_g^2$. For a fractal cluster, $R_g \sim N^{1/D_f}$ where D_f is the fractal dimension of the cluster while for a compact, spherical cluster (appropriate in the coalescence stage) $R_g \sim N^{1/3}$. In addition, since $N_c N = N_m$ where N_m is the number of monomers, one easily finds that $R_g(t) \sim N^{\nu}$ where $\nu = z/D_f$ for fractal clusters and $\nu = z/3$ for spherical cluster.

In the ballistic regime, $v \sim N^{-1/2}$ via the equipartition of energy. Since $R_g \sim N^{1/3}$ here, one finds that $K \sim N^{1/6}$ or $\lambda = 1/6$, $z = 1.2$ and $\nu = z/3 = 0.4$ (Coalescence with a ballistic motion). In the diffusive case, one can still use the dimensionally correct form $K \sim Av$ but now v becomes a characteristic velocity relevant for diffusion. This velocity must scale as

$$v \sim \frac{D}{R_c} \tag{6.3}$$

where D is the diffusion constant and R_c is a characteristic diffusional length-scale. In the dilute limit of the Stokes-Einstein diffusion, R_g is the only relevant length-scale in the system and one can write $v \sim D/Rg$. In addition, $A \sim R_g^2$. Thus one finds $K \sim D\,Rg$, a result originally derived by Smoluchowski in a more rigorous fashion. In the continuum limit $D \sim 1/Rg$ which implies that K is a constant which in turn leads to $\lambda = 0$ and $z = 1$ in the dilute limit of Stokes-Einstein diffusion. These results will be valid whether the resulting clusters are fractal or compact.

6.4 Simulation Results

Coalescence Stage

The coalescence stage was studied using two different growth models; ballistic and diffusive. Both were studied with monomer volume fraction of $f_v = 0.001$. In Figure 6.1 we show 2d projection snapshots of part of the system at 0, 5000, and 40,000 time steps, respectively. Here, monomers moved ballistically which yields an average diameter of 7σ at 40,000 time steps.

In Figure 6.2 we plot the number of coalesced clusters $N_c(t_D)$ versus time t_D in a log-log graph during coalescence with ballistic movement of the particles. The slope of the straight line

yields the kinetic exponent z = 1.2 in excellent agreement with a scaling analysis presented before. We also note that the average size of the coalesced clusters $< R(t_D) >$ when plotted versus t_D in a log-log graph yields an exponent of $\nu = 0.4$ in excellent agreement with scaling results. In contrast, for coalescence with a diffusive motion of clusters we obtain z = 1 (Figure 6.3) in agreement with scaling results.

In Figure 6.4 we have plotted the scaled size distributions for both ballistic and diffusive coalescence at t_D for a number of different values of t_D. For the range $x > 1$, excellent agreement with the scaling prediction is found as shown in Figure 6.4

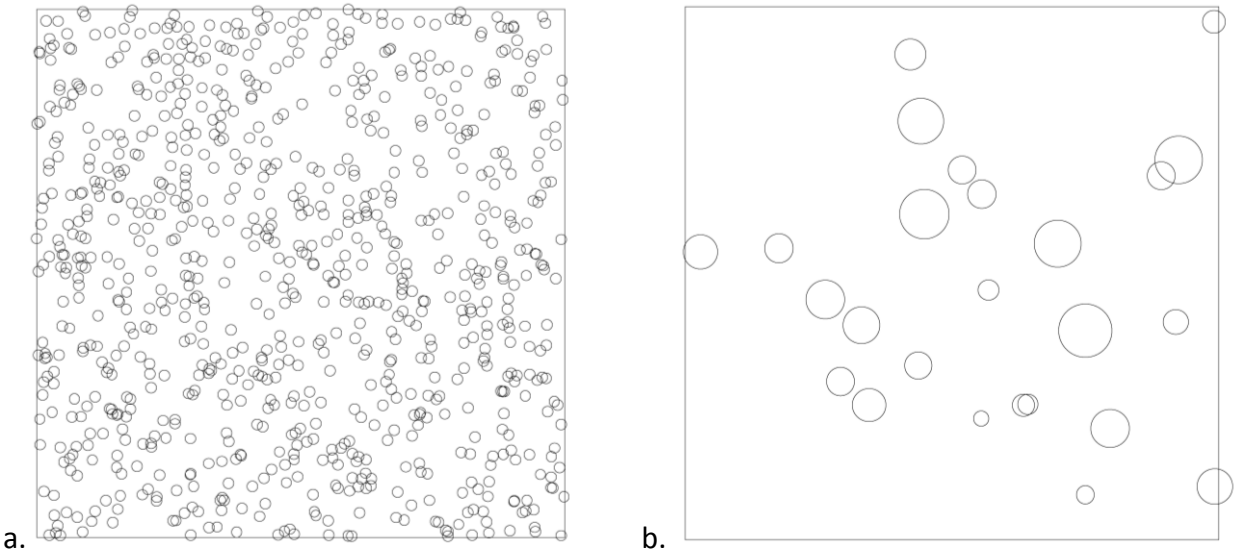

a. b.

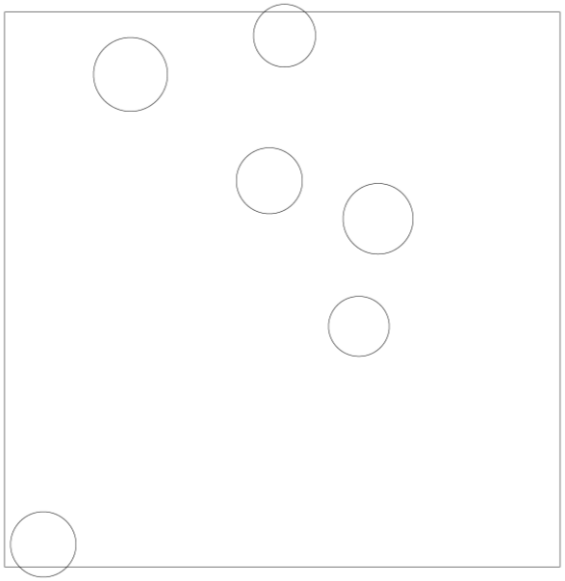

c.

Figure 6.1 Snapshots of the system during the ballistic coalescence phase. The volume fraction if $f_v=0.001$. 2d projections of part of the system are shown at Monte Carlo time steps 0, 5000, 40,000, respectively. The apparent overlap is due to projection of the 3d volume onto a 2d surface; all clusters are spherical.

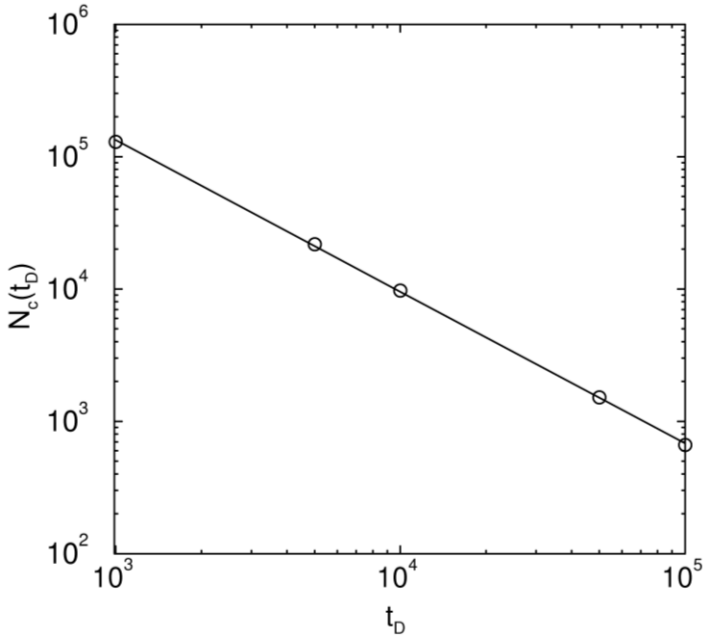

Figure 6.2 Number of particles $Nc(t_D)$ versus time t_D shown in a log-log plot during coalescence with a ballistic movement of the particles. The slope of the straight line yields the kinetic exponent $z = 1.2 \pm 0.05$.

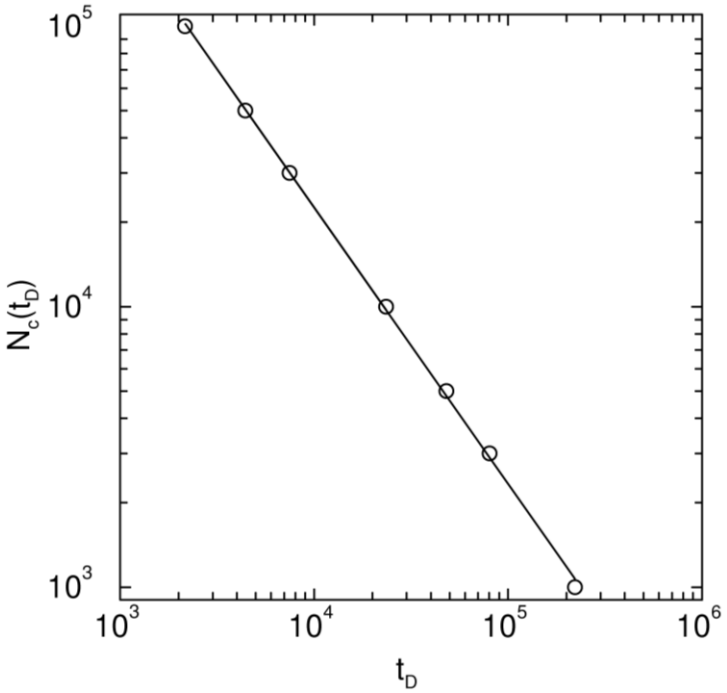

Figure 6.3 . Number of particles $Nc(t_D)$ versus time t_D shown in a log-log plot during coalescence with a diffusive movement of the particles. The slope of the straight line yields the kinetic exponent $z = 1 \pm 0.05$.

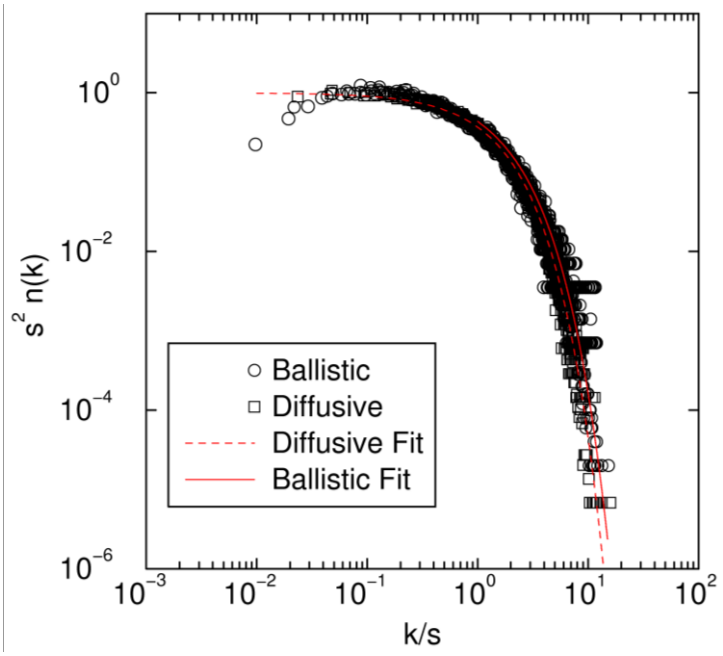

Figure 6.4 Scaled form of ballistic and diffusive particle size distributions at t_D for various values of t_D. The scaled distribution has the functional form $\varphi(x) = Ax^{-\lambda}e^{-\alpha x}$ for large sizes ($x>1$) with $\alpha = 1 - \lambda$ with λ (ballistic coalescence)$= 1/6$ and λ (diffusive coalescence)$=0$.

DLCA Stage

After the coalescence phase, there are 10,000 polydisperse monomers present in the simulation box at t_D. Diffusive limited cluster-cluster aggregation goes on to make fractal aggregates beyond time t_D. The initial monomer size distribution in DLCA is thus a set of poly-disperse coalesced clusters obtained from either ballistic or diffusive aggregation with coalescence. Figure 6.5 shows an example of a ramified cluster formed with polydisperse coalesced clusters from ballistic coalescence as monomers.

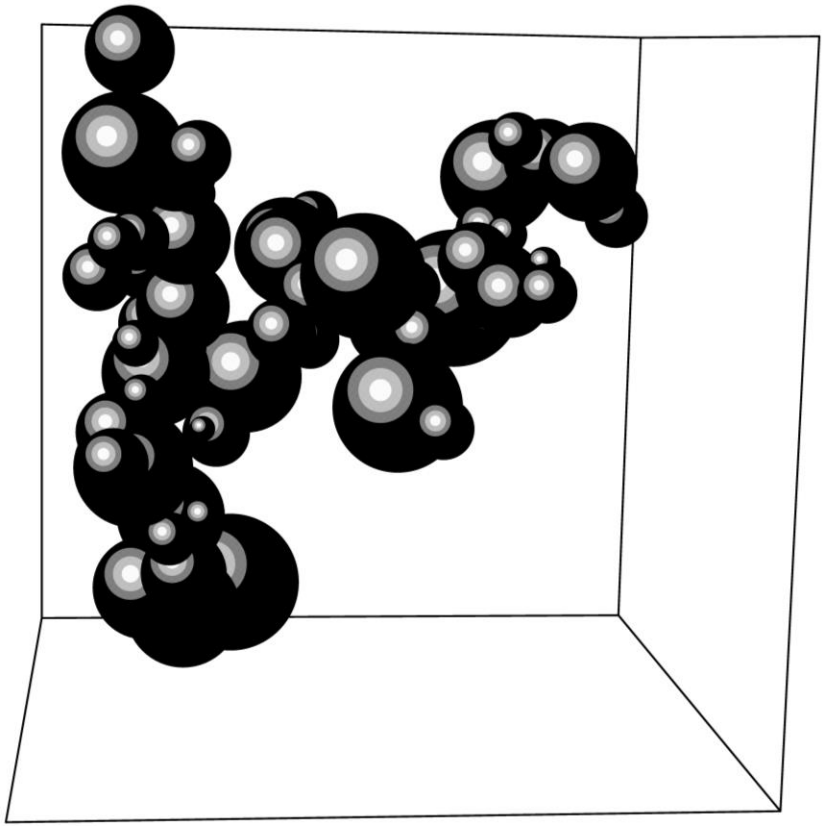

Figure 6.5 A typical cluster formed from DLCA with ballistic monomer mass distribution. This snapshot was taken at 2,000,000 time steps.

Since the number of monomers at this DLCA stage is much smaller than in the coalescence phase, we compute inverse cluster count $N_c^{-1}(t)-N_c^{-1}(0)$ instead of just the cluster

number $N_c(t)$. In Figure 6.6 we show $N_c^{-1}(t)-N_c^{-1}(0)$ versus time t in a log-log plot for mono-disperse DLCA and DLCA with polydisperse distributions originating from both ballistic and diffusive coalescence as discussed before. Slope for each of these curves yields $z = 1$ in agreement with diffusive scaling. The slight increase in slope seen for the pure DLCA case at late times originates from cluster crowding [83].

Figure 6.7 shows log-log plots of average radius of gyration of clusters $\langle R_g \rangle$ versus time t for mono-disperse DLCA and DLCA with poly-disperse distributions originating from both ballistic and diffusive coalescence. The straight line part for all three curves yields an exponent of $\nu = 0.55$. Note that the radius of gyration of the clusters is smaller when DLCA process starts with a poly-disperse distribution.

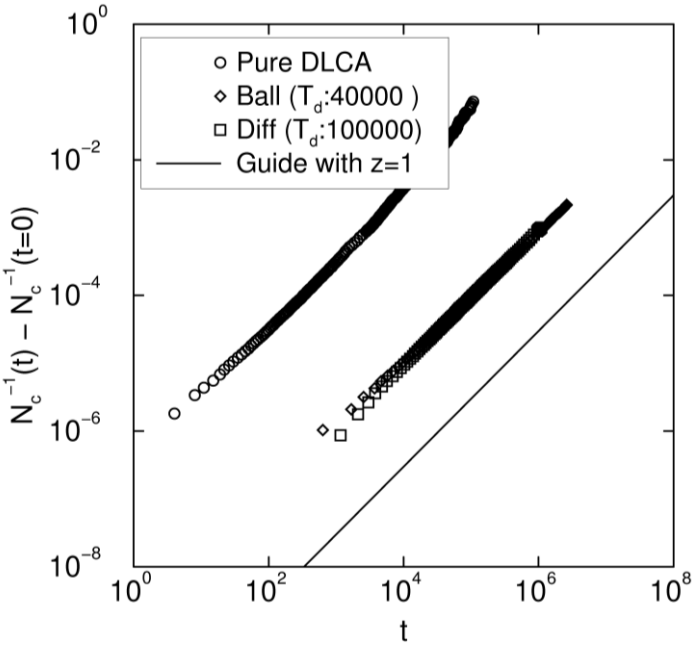

Figure 6.6 . Log-log plot of inverse cluster count $N_c^{-1}(t)-N_c^{-1}(0)$ versus time t for mono disperse DLCA and DLCA with poly-disperse distributions originating from both ballistic and diffusive coalescence as discussed before. Slope for each of these curves yields $z = 1$ in agreement with diffusive scaling. At final times ($t_D = 100{,}000$ for diffusive coalescence and t_D = 40,000 for ballistic coalescence) both diffusive and ballistic coalescence yield an average particle diameter of 7σ.

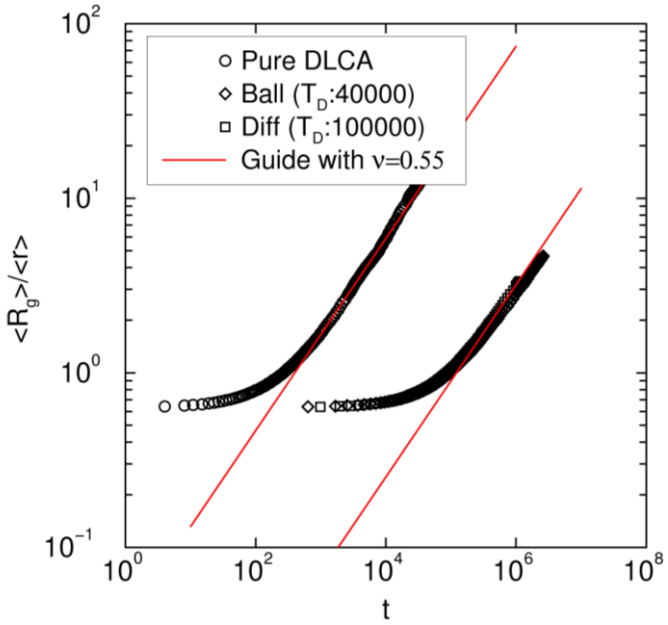

Figure 6.7 Log-log plots of average radius of gyration of clusters <Rg> versus time t for mono-disperse DLCA and DLCA with poly-disperse distributions originating from both ballistic and diffusive coalescence. The straight line part for all three curves yield an exponent of $\upsilon = 0.55$.

Next we study the fractal dimension of the clusters formed in the DLCA process. In Figure 6.8a and b, we show a log-log graph of mass of the clusters M at various times rescaled by the average particle mass versus the radius of gyration of the clusters (R_g) rescaled by the average particle radius for both ballistic and diffusive coalescence initial particle distributions, respectively. There are two distinct zones in this graph. Below $R_g/<r> = 1$ the clusters are compact (dimers, trimers, and other small nonfractal clusters) and yield an exponent of $D_f = 3$. For $(R_g/<r>) > 1$, the straight line fit to the data yields $D_f = 1.7 \pm 0.1$ in each case. The prefactor k_0 obtained from this study ($k_0 = 1.5 \pm 0.1$) is consistent with previous simulation studies [23], [31], [35] of DLCA aggregation in both lattice and off-lattice geometries.

The scaling form for both DLCA with ballistic and diffusive coalescence is shown in Figure 6.9. The scaling function $\varphi(x) = Ax^{-\lambda}e^{-\alpha x}$ with $\alpha=1-\lambda$ and for DLCA a homogeneity of $\lambda = 0$ was plotted with the mass distribution data and shows excellent agreement.

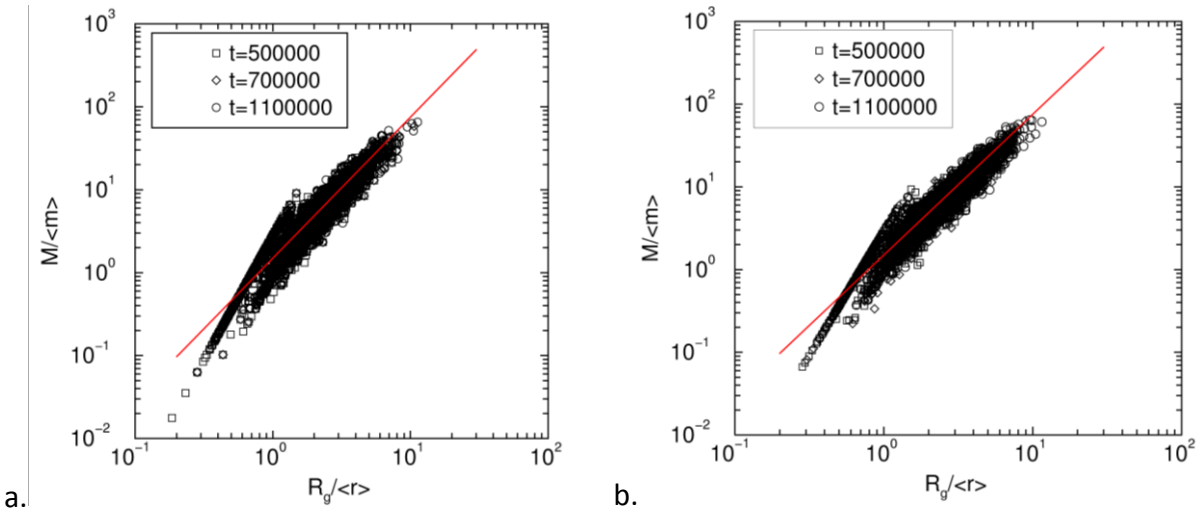

Figure 6.8 (a) Log-log graph of mass of the clusters *M* rescaled by the average particle mass <m> versus the radius of gyration of the clusters rescaled by the average particle radius <r> for ballistic coalescence initial particle distributions. There are two distinct zones in this graph. Below $R_g/\langle r\rangle = 1$ the clusters are compact (dimers, trimers, and other small non-fractal clusters) and yield an exponent of $D_f = 3$. Above this value of $R_g/\langle r\rangle$, the straight line fit to the data yields $D_f = 1.7 \pm 0.1$. (b) Same as in 8 (a) except for diffusive coalescence initial particle distributions. As before, there are two distinct zones in this graph. Below $R_g/\langle r\rangle = 1$ the clusters are compact (dimers, trimers, and other small nonfractal clusters) and yield an exponent of $D_f = 3$. Beyond this value of $R_g/\langle r\rangle$, the straight line fit to the data yields $D_f = 1.7 \pm 0.1$.

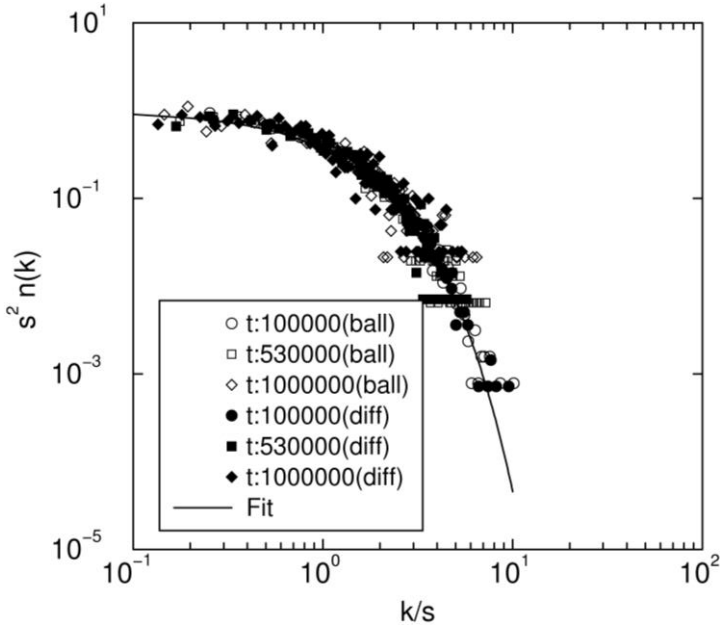

Figure 6.9 Scaling of DLCA with ballistic and diffusive monomer mass distributions. Scaling function is $\varphi(x)=Ax^{-\lambda}e^{-\alpha x}$ with $\lambda = 0$ agrees well with the data.

6.5 Concluding Remarks

In summary, we have carried out computer simulation of aggregation in a system where during the aggregation process, particles coalesce at first and then subsequently these coalesced clusters stop coalescing and form ramified, fractal aggregates. In the coalescence stage, particles move either ballistically or diffusively up to a certain time t_D. Next these coalesced clusters move diffusively and aggregate to form ramified aggregates.

We have found the kinetic exponent z in the coalescence stage depends on the type of cluster motion (ballistic or diffusive). Results for z in each case are in agreement with a scaling description developed by us. However, once the system moves over to the DLCA stage, one recovers pure DLCA results for both the kinetic exponent and the fractal dimension of the ramified clusters. Thus the coalescence induced polydispersity of the primary particles for the DLCA stage does not affect the DLCA stage outcomes.

The polydispersity of the coalesced clusters is determined by the mean field aggregation kinetics. Thus both the primary particle kinetics of growth and size distribution in a fractal aggregate could be used as indicator of a previous regime of particle-particle aggregation with coalescence and thereby distinguished from other mechanisms of primary particle formation such as nucleation and surface growth.

Chapter 7 - Shear History Independence in Colloidal Aggregation

7.1 Introduction

In this chapter we have carried out detailed simulations of aggregation in the presence of shear in a model colloidal system with a short-range attractive potential. Many experimental and theoretical studies have been carried out to investigate the effect of shear flow on the kinetics of aggregation, [84]–[97] the resulting size distributions, and structures of particle aggregates. To summarize these findings, previous shear experiments have seen either fragmentation because of shear, restructuring as indicated by fractal dimensions larger than the diffusion-limited cluster aggregation (DLCA) value of $D_f = 1.8$ or experienced both fragmentation and restructuring. Often the shear fragmentation was eventually balanced by the aggregation, and a steady state was reached. The shear aggregation in these studies was dominant over Brownian aggregation.

The numerical simulations presented in this chapter have been stimulated by two experiments in our laboratory, which strongly suggest that there is a great bounty of new phenomena that have neither been explored nor possibly even discovered when a dispersion of colloidal particles undergoes aggregation under the influence of shear[98], [99]. Experiments show that for modest shears, as indicated by the Péclet number being in the range of unity (unlike any previous work), shear can enhance the aggregation and gelation rate but the aggregates formed under shear can be either fractal or hybrid mixed fractal structures [99].

Our results provide the first theoretical support to these scattered clues seen in experiments on complex systems. Simulation results are clean and deal with a simple aggregating system in the presence of shear with a well-studied short-range attractive potential. Shear rates employed in the simulations can be attained in laboratory experiments, as confirmed by computing the dimensionless Péclet numbers for the simulation studies. For weak shear rates

(characterized by Péclet numbers less than unity), we find that the shear enhanced the aggregation and that the long-time state of the system is independent of the shear history. For strong shear rates, precipitous fragmentation occurred after the shear was turned on and, after an induction period, in which numerous runs were shown to be stochastic, the aggregation quickly rebounded in a manner similar to classical nucleation phenomena. However, the long-time state of the system is, once again, independent of the shear history, as if the shear rate was a state variable of the aggregating system.

7.2 Simulation Method

We have performed simulations using a three-dimensional (3D) Brownian dynamics model in the presence of a steady shear flow. This involved solving the Langevin equation

$$m\ddot{r}_i = -\nabla U_i - \Gamma\dot{r}_i + W_i(t) + \Gamma\dot{\gamma}\left(y_i - \frac{L}{2}\right)\hat{z} \qquad (7.1)$$

where U_i is the pair particle interaction, Γ is the drag coefficient, $W_i(t)$ is the random force acting on a particle, $\dot{\gamma}$ is the shear rate, y_i is the y component of the position vector of the ith particle, $\hat{z}$ is the unit vector along the z axis, and L is the box length [18]. Hydrodynamic interactions, including lubrication forces, are ignored in the simulation [100]. We note that an equivalent Smoluchowski equation or a "Liouville equation on the diffusive time scale" can be written for the probability density function of the position coordinates of the Brownian particles in the system [101].

The interparticle potential considered here is a short-range attractive potential. As a prototype, we consider the well-studied Asakura−Oosawa (AO) [102] short-range depletion potential. In particular, the potential U acting upon each colloidal particle has a 2-fold

contribution: the two-body depletion potential U_{AO} plus a repulsive hard-core-like interaction U_{hc} given by the following expressions:

$$U(r_{ij}) = U_{AO}(r_{ij}) + U_{hc}(r_{ij}) \tag{7.2}$$

where

$$\frac{U_{AO}}{kT} = \phi_p \left(\frac{1+\zeta}{\zeta}\right)^3 \left[\frac{3r_{ij}}{2(1+\zeta)} - \frac{1}{2}\left(\frac{r_{ij}}{1+\zeta}\right)^3 - 1\right] \text{ for } r_{ij} < 1 + \zeta \tag{7.3a}$$

$$\frac{U_{AO}}{kT} = 0 \text{ for } r_{ij} < 1 + \zeta \tag{7.3b}$$

and

$$\frac{U_{hc}}{kT} = r_{ij}^{-\alpha} \tag{7.4}$$

In equation 7.3, ζ is the size ratio between a polymer coil and a colloidal particle, which controls the range of the depletion interaction in the AO model and ϕ_p is a parameter that controls the strength of the interaction. All of our simulations are for $\zeta = 0.1$.

In the hardcore-like repulsive interaction given by equation 7.4, we have set $\alpha = 36$. Exponents $\alpha < 36$ are reported to lead to anomalies when a hardcore mimic is required in the potential [103]. The total pair potential $U = U_{AO} + U_{hc}$ passes through a minimum value (U_{min}) that depends upon ζ and ϕ_p. In what follows, we will often characterize the strength of the potential in terms of the absolute value of the minimum potential depth, $U_m = |U_{min}|$, which is 10 kT in our simulations.

Our simulations used a set of reduced units, where $m = 1$, monomer diameter $\sigma = 1$, and $kT = 1$. We choose $\Gamma = 0.5$, shear rates between $\dot{\gamma} = 0.1$ and 1.0, and time step $\Delta t = 0.0001\text{-}0.005$ in reduced time units of $\sigma(m/kT)^{1/2}$. For this choice of Γ, particle motion in the absence of shear is purely diffusive for $t \gg 1/\Gamma$; i.e., $t \gg 2$ in our units. In one unit of this reduced time, a "free" monomer would diffuse a distance of $12^{1/2}\sigma$ for the value of Γ used here. A total of 40 000 monomers were randomly placed in a box of length L = 128 to yield a monomer volume fraction of $f_v = 0.01$. For the deep quench considered here ($U_m = 10$ kT) and in the absence of any shear, the system shows DLCA behavior similar to an irreversible, aggregating system [104]. Lees−Edwards boundary conditions were used, which is standard for shear simulations [105]. The system was allowed to develop without shear until a shear start time t_s, and then shear was turned on. Three shear start times were used: $t_s = 0$, 250, and 500. For each shear rate and shear start time, the system was allowed to reach a steady state at long times. This was monitored by the aggregation kinetics and the shape and structure of the aggregates themselves.

7.3 Results

Figure 7.1a shows the average aggregate size in terms of the number of monomers per aggregate N versus time since the onset of shear. There is a zero shear rate curve, and then at three different start times (0, 250, and 500), a shear of 0.1 is turned on. This figure shows two important facts: (1) The shear enhanced the aggregation, and (2) the long-time state of the system is independent of the shear history. Figure 7.1b is similar to Figure 7.1a; only now the shear rate is 1.0. Figure 7.1b shows three important facts: (1) Precipitous fragmentation occurred after the shear was turned on; (2) after an induction period, in which numerous runs were shown to be stochastic, the aggregation quickly rebounds in a manner similar to classical nucleation

phenomena to a regrowth period; and (3) after this regrowth, the long-time state of the system is, once again, independent of the shear history!

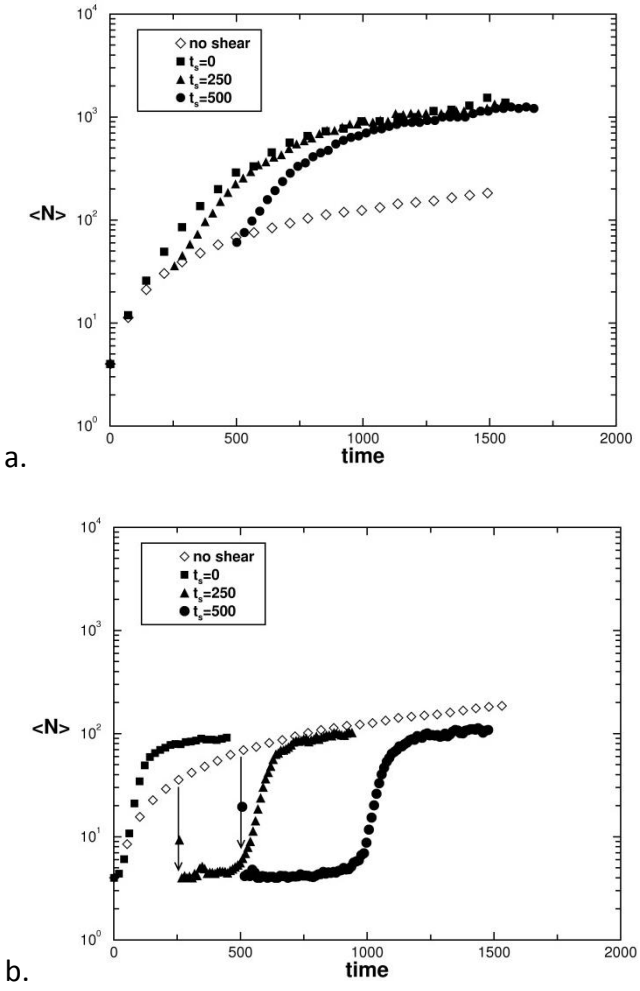

Figure 7.1 Average number of monomers per aggregate versus rescaled time with shear of (a)$\dot{\gamma}$=0.1 and (b) $\dot{\gamma}$=1.0 turned on at t_s =0, 250, and 500.

Other shear rates show these general features as well but with different degrees of intensity. Figure 7.2 shows results for a range of shears between 0 and 1.0, all with a start time of 250. As shear starts, the aggregates fragment to a minimum monomer number (mass). This minimum mass decreases systematically with shear and reaches total system breakdown with a shear rate of 1.0. We also note that the average aggregate mass at the steady state seems to scale with shear rate, highlighting the interplay between fragmentation and enhanced aggregation.

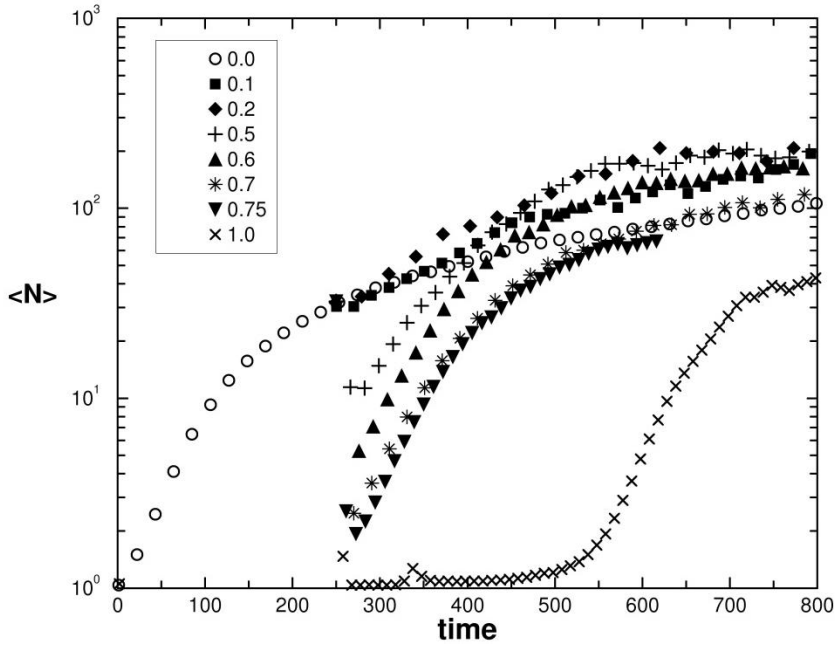

Figure 7.2 Average number of monomers per aggregate versus rescaled time for a variety of shear rates all turned on at $t_s=250$.

The structure of the aggregates can be discerned via direct real space visualization, analysis of bond-orientational order parameters, and Fourier transformation to yield the structure factor. The latter has the advantage of yielding an ensemble average and is realizable experimentally with light scattering. Zero shear yields a hybrid structure, which we have termed "fat fractals"[36], [106]; the monomers form dense clumps over short length scales, and then these clumps form open aggregate structure with the classic DLCA fractal dimension of $D_f=1.8$. Sheared systems continue to yield fat fractals but with denser aggregates, as identified by larger fractal dimensions. A shear of 0.1 yields fractal dimensions of 2.6, as shown in Figure 7.3a, and a strong shear of 1.0 yields compact objects, as indicated by a Porod q^{-4} functionality for the structure factor shown in Figure 7.3b. However, we have not addressed large-scale anisotropy in the cluster scale in this work.

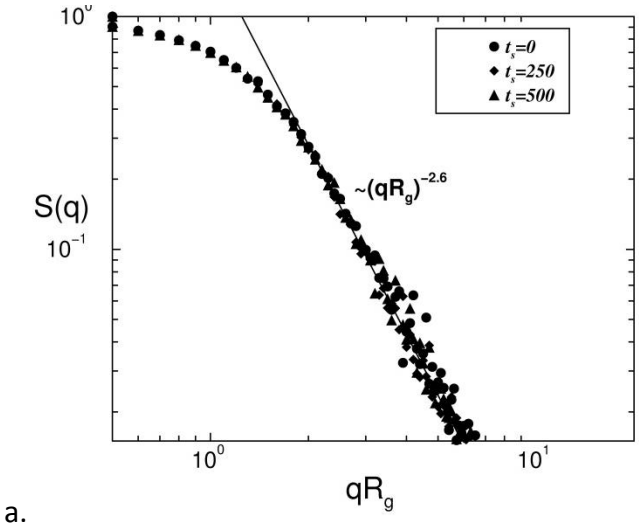

a.

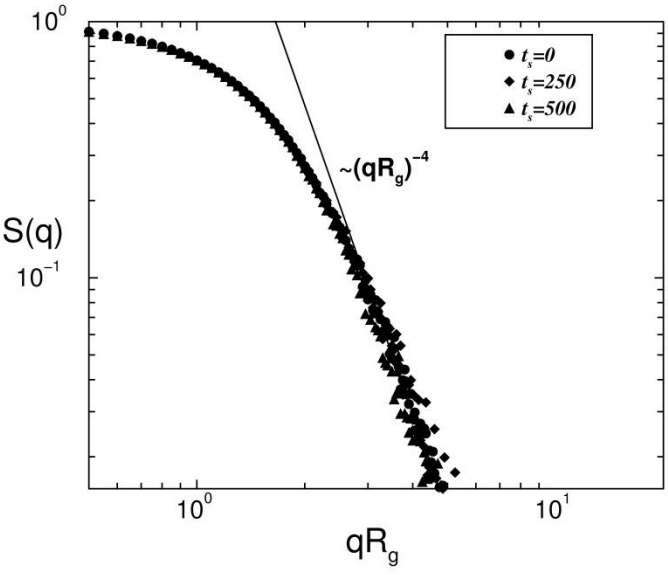

b.

Figure 7.3 Structure factor for shear rate (a) $\dot{\gamma}=0.1$ and (b) $\dot{\gamma}=1.0$ with three different t_s values. In panel a, the guide line has a slope of −2.6. In panel b, aggregates are compact, indicated by the Porod q^{-4} functionality.

To further analyze the details of the aggregate morphology and to differentiate between the liquid- and solid-like particles in the aggregates, we use the scalar product definition of the bond orientational order parameter q6 for the ith particle with the neighboring j particles [107]. First, we define the connected neighbors. Two neighbors are considered to be connected if the above scalar product is greater than some threshold value (chosen to be 0.65 as used in the

literature [108]). For a distinction between solid- and liquid-like particles, one can set another threshold value for the number of connections. Following ref [108], any particle that has more than seven connections is considered solid-like; particles with less than or equal to seven connections are considered as liquid-like. Once the solid- or liquid-like behavior of the particles is determined, we further assign the crystalline identity to each solid-like particle i. Figure 7.4 shows examples of aggregates and their crystalline structure. We observe that typical "fat fractal" aggregates in the absence of any shear is mostly liquid-like. However, aggregates corresponding to a weak shear rate of $\dot{\gamma}=0.1$ are more compact than the fat fractal aggregate and show large pockets of crystalline order. For a much larger shear rate of $\dot{\gamma}=0.1$, the aggregates are very compact and ordered but much smaller in size because of fragmentation.

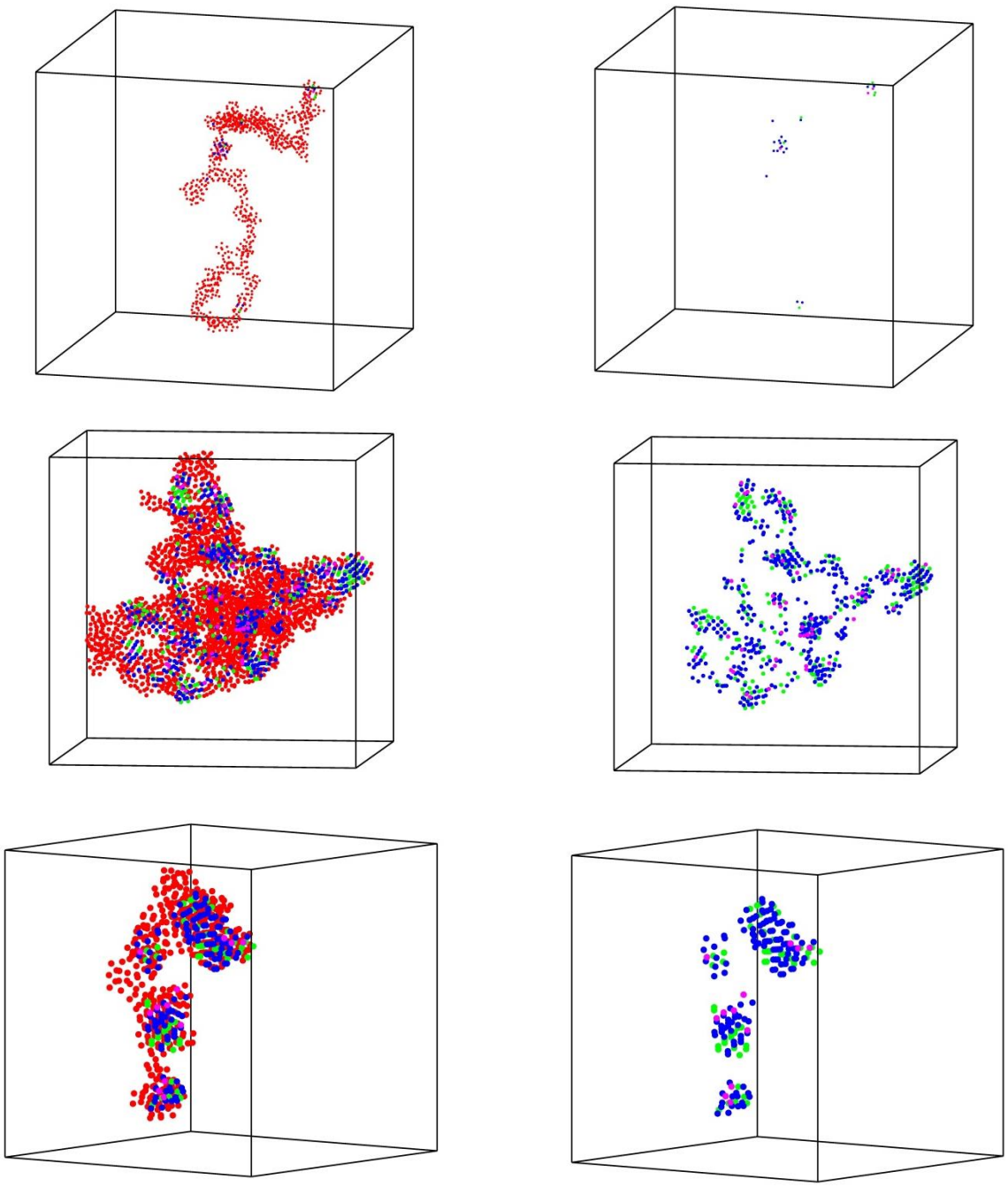

Figure 7.4 Red particles are liquid-like; green have face-centered cubic (fcc) structure; blue particles have hexagonal close-packed (hcp) structure; and pink particles have some other ordering. (a) Typical "fat fractal" aggregate when no shear is applied. (b) Only the crystalline particles of the aggregate shown in panel a are shown. (c) Aggregate formed under a shear rate of $\dot{\gamma}=0.1$. Note that the aggregate is more compact than the fat fractal aggregate and also shows large pockets of crystalline order. (d) Only the crystalline particles of the aggregate shown in panel c are shown. (e) Aggregate formed under a shear rate of $\dot{\gamma}=1.0$. Now the aggregate has pockets of crystalline order, but it is smaller in size than $\dot{\gamma}=0.1$ aggregates because of fragmentation. (f) Only the crystalline parts of the aggregate shown in panel e are shown.

It is very important to see if these fascinating numerical simulation results have anything to do with real systems. The "Rosetta Stone" to allow us to connect between the simulation and real world is the Péclet number. The Péclet number Pe is a dimensionless number that is the product of the time that it takes a particle to diffuse one diameter and the shear rate. It is a measure of the relative importance of the contributions of fluid shear and Brownian motion to the collision frequency of disperse phase clusters and monomers. Whether those collisions result in aggregation (or even breakage) events depends upon many other factors, such as the strength of the particle attractive forces and the morphology of the colliding aggregates. Generally speaking, when Pe > 1, shear is dominant, and when Pe < 1, diffusion is dominant. The dimensionless nature of Pe provides a very useful link between experimental and numerical simulations. The Péclet number is commonly written as

$$Pe = \frac{6\pi\eta R_m^3 \dot{\gamma}}{kT} \tag{7.5}$$

where η is the viscosity, R_m is the particle mobility radius, and $\dot{\gamma}$ is the shear rate. The drag coefficient Γ is related to the viscosity by $\Gamma = 6\pi\eta R_m$. Thus, the Péclet number becomes

$$Pe = \frac{\Gamma R_m^2}{kT}\dot{\gamma} \tag{7.6}$$

In our simulation, Γ=0.5, kT = 1, and $\dot{\gamma}$= 0.1-1. When shear is turned on from the beginning, we use R_m=0.5 to yield Pe =0.0125−0.125. In the other extreme, for start times of 500, Rm begins around 2.3 to yield Pe = 0.26−2.6. These Péclet numbers are well in the range accessible to experiments to imply that the remarkable results seen in the simulation should appear in real

world experiments as well. For example, the Péclet numbers for the experimental studies cited in the Introduction [98], [99]range from 0.01 to 260.

7.4 Concluding Remarks

In summary, numerical simulations of aggregation in the presence of shear in a model colloidal system characterized by short-range attractive potential shows that weak shear enhances the aggregation process, while strong shear leads to fragmentation and subsequent nucleation and rebound in cluster growth after an induction time. A detailed energetic and entropic theory of aggregation that can explain these phenomena is lacking at present. However, a few general comments can be made. To restructure or break up flocs under shear flow, local stresses must create forces on a pair of particles stronger than the interparticle attraction. For relatively mild shears, apparently clusters can simply undergo rearrangement into structures with sufficient strength to prevent breakage. Above some threshold of shear, fat fractal aggregates are simply too fragile to survive and, consequently, are destroyed and eventually replaced by compact, pseudo-crystalline aggregates. We should further note that Brownian dynamics ignores the effect of the particles on the flow, producing a “free-draining” floc. That produces stronger stresses within the flow and weaker stresses on the periphery, which should have implications on the breakup. What is striking though is that, in each case, the long-time state of the system is independent of the shear history, to imply that the shear rate acts as a state variable of the aggregating system. We expect our results to be valid for general short-range attractive potentials with a deep well depth. Further studies are needed to elucidate how the depth and range of this attractive potential affect the shear induced aggregation and breakup.

Chapter 8 - Conclusion and Summary

The goal of this dissertation was to gain further insight into some fundamental behaviors of aerosol and colloidal systems that develop fractal aggregates. These systems are important in many fields from climate research [109] to theories on the formation of planets [110]. Using computational techniques that simulate the motion and subsequent aggregation of particles in aerosol and colloidal systems, we have explored in depth many common but not well studied systems. The work presented here falls under two camps: study of cluster structure and study of cluster growth.

In diffusive driven aggregation, the previously overlooked cluster shape and monomer packing were described in detail. The monomer packing describes the structure of the aggregate at its smallest level while the cluster shape is a large scale characteristic of the cluster. Both were found to have significant impact on real world analysis via the dependence on structure factor and the scaling prefactor k_0. Thus both are put on equal footing with the fractal dimension D_f as necessary descriptors of a fractal cluster. An analytical theory to describe cluster shape, packing, and dimensionality was used that successfully predicted, through use of a restricted hierarchical model, cluster shape and dimensionality. The shape was described by a circumscribing rectangular with sides parallel to the principal radii. Then the ratios of the lengths were used to measure shape. It was predicted by the restricted hierarchical model and confirmed through DLCA simulation that the cluster shape is described by the Fibonacci series and the Divine Proportion, generalized into the given spatial dimension.

Cluster growth kinetics were studied in the transition regime were the motion of the aggregates transforms from ballistic to Epstein diffusion as the aggregates grow and was simulated by two different algorithms: the first, a slow but rigorous Brownian Dynamics method

that solved for aggregate motion through the integration of the Langevin equation and a second, less exact but faster Monte Carlo method that decided aggregate movement through use of an ad hoc probability of movement. For a given volume fraction both simulations found the same crossover behavior in the kinetic exponent. To our surprise we found, at all volume fractions studied, both the nearest neighbor separation and the aggregate size were equally adequate at describing the crossover.

Motivated by experiments in which aggregation is initiated with a high temperature explosion [69]–[71], aggregation simulations were carried out in which molten particles first coalesce into spheres and then subsequently these polydispersed monomers cool and coalescence stops. Motion then becomes diffusive and monomers stick at point contacts to form fractals. The growth kinetics of the coalescence stage was tracked and found to be in agreement with theory. The kinetic exponent and overall cluster structure in the diffusive cluster-cluster stage was found be in agreement with DLCA that started with monodispersed monomers.

Finally, stimulated by two experiments that showed for modest shears an enhancement of the aggregation and gelation rate occured but the aggregates formed under these conditions had either fractal or hybrid mixed fractal structures[98], [99]. Simulations of aggregation in the presence of shear were carried out. A colloidal system characterized by short-range attractive potential showed that weak shear enhanced the aggregation process, while strong shear led to fragmentation and subsequent nucleation as cluster growth rebounded after an induction time. For relatively mild shears clusters undergo rearrangement into structures with sufficient strength to prevent breakage. Above some threshold of shear, fractal aggregates are too fragile to survive and, consequently, are destroyed and eventually replaced after some time by compact, pseudo-crystalline aggregates.

Future avenues for research on cluster shape and growth kinetics are numerous. For example, the importance of aerosolized fractal clusters for earth's radiative budget especially those from carbon sources such as forest fires and man-made pollution has become a subject of great importance [111]–[114]. The effect that shape and dimensionality has on extinction cross-section is only recently been look at and yet to be fully understood. The work presented in this dissertation provides a good starting point in selecting what cluster parameters to use for theoretical studies of light scattering and absorption in atmospheric aggregates.

References

[1] B. B. Mandelbrot, *Fractals: Form, Chance and Dimension*, 1st edition. San Francisco: W.H.Freeman & Company, 1977.
[2] M. N. Angeja, *fractal_tree*. 2011.
[3] Abe Bingham, *Fractal Tree*. 2006.
[4] P. Meakin, "Formation of Fractal Clusters and Networks by Irreversible Diffusion-Limited Aggregation," *Phys. Rev. Lett.*, vol. 51, no. 13, pp. 1119–1122, Sep. 1983.
[5] R. Jullien and R. Botet, *Aggregation and Fractal Aggregates*. Singapore: World Scientific Pub Co Inc, 1987.
[6] F. Family, *Kinetics of Aggregation and Gelation*. Amsterdam a.o: Elsevier Science Ltd, 1985.
[7] D. Stauffer and A. Aharony, *Introduction To Percolation Theory: Revised Second Edition*, 2 edition. London: Taylor & Francis, 1994.
[8] P. Meakin, "A Historical Introduction to Computer Models for Fractal Aggregates," *J. Sol-Gel Sci. Technol.*, vol. 15, no. 2, pp. 97–117, Aug. 1999.
[9] P. Meakin, "Off Lattice Simulations of Cluster Cluster Aggregation in Dimensions 2-6," *Phys. Lett. A*, vol. 107, no. 6, pp. 269–272, 1985.
[10] S. K. Friedlander, *Smoke, Dust, and Haze: Fundamentals of Aerosol Dynamics*, 2 edition. New York: Oxford University Press, 2000.
[11] F. Family, *Kinetics of Aggregation and Gelation*. Amsterdam a.o: Elsevier Science Ltd, 1985.
[12] S. K. Friedlander, *Smoke, Dust, and Haze: Fundamentals of Aerosol Dynamics*, 2 edition. New York: Oxford University Press, 2000.
[13] R. Jullien and R. Botet, *Aggregation and Fractal Aggregates*. Singapore: World Scientific Pub Co Inc, 1987.
[14] A. Hasmy and R. Jullien, "Sol-Gel Process Simulation by Cluster-Cluster Aggregation," *J. Non-Cryst. Solids*, vol. 186, pp. 342–348, Jun. 1995.
[15] F. G. Pierce, "Aggregation in colloids and aerosols," 2007.
[16] D. J. Fry, "Aggregation in dense particulate systems," 2003.
[17] W. F. van Gunsteren and H. J. C. Berendsen, "Algorithms for brownian dynamics," *Mol. Phys.*, vol. 45, no. 3, pp. 637–647, Feb. 1982.
[18] J. J. Cerdà, T. Sintes, C. Holm, C. M. Sorensen, and A. Chakrabarti, "Shear effects on crystal nucleation in colloidal suspensions," *Phys. Rev. E*, vol. 78, no. 3, p. 031403, Sep. 2008.
[19] R. D. Mountain, G. W. Mulholland, and H. Baum, "Simulation of aerosol agglomeration in the free molecular and continuum flow regimes," *J. Colloid Interface Sci.*, vol. 114, no. 1, pp. 67–81, Nov. 1986.
[20] R. K. Chakrabarty, H. Moosmüller, W. P. Arnott, M. A. Garro, G. Tian, J. G. Slowik, E. S. Cross, J.-H. Han, P. Davidovits, T. B. Onasch, and D. R. Worsnop, "Low Fractal Dimension Cluster-Dilute Soot Aggregates from a Premixed Flame," *Phys. Rev. Lett.*, vol. 102, no. 23, Jun. 2009.

[21] D. Fry, A. Mohammad, A. Chakrabarti, and C. M. Sorensen, “Cluster Shape Anisotropy in Irreversibly Aggregating Particulate Systems,” *Langmuir*, vol. 20, no. 18, pp. 7871–7879, Aug. 2004.
[22] T. Nicolai, D. Durand, and J.-C. Gimel, “Static structure factor of dilute solutions of polydisperse fractal aggregates,” *Phys. Rev. B*, vol. 50, no. 22, pp. 16357–16363, Dec. 1994.
[23] C. M. Sorensen and G. C. Roberts, “The Prefactor of Fractal Aggregates,” *J. Colloid Interface Sci.*, vol. 186, no. 2, pp. 447–452, Feb. 1997.
[24] C. M. Sorensen and G. M. Wang, “Size distribution effect on the power law regime of the structure factor of fractal aggregates,” *Phys. Rev. E*, vol. 60, no. 6, pp. 7143–7148, Dec. 1999.
[25] M. Lattuada, H. Wu, and M. Morbidelli, “Hydrodynamic radius of fractal clusters,” *J. Colloid Interface Sci.*, vol. 268, no. 1, pp. 96–105, Dec. 2003.
[26] C. M. Sorensen, “Light Scattering by Fractal Aggregates: A Review,” *Aerosol Sci. Technol.*, vol. 35, no. 2, pp. 648–687, Jan. 2001.
[27] M. Y. Lin, H. M. Lindsay, D. A. Weitz, R. C. Ball, R. Klein, and P. Meakin, “Universality in colloid aggregation,” *Nature*, vol. 339, no. 6223, pp. 360–362, Jun. 1989.
[28] P. Meakin, “Fractal aggregates,” *Adv. Colloid Interface Sci.*, vol. 28, no. 4, pp. 249–331, Jun. 1988.
[29] M. Kolb, R. Botet, and R. Jullien, “Scaling of Kinetically Growing Clusters,” *Phys. Rev. Lett.*, vol. 51, no. 13, pp. 1123–1126, Sep. 1983.
[30] C. M. Sorensen and A. Chakrabarti, “The sol to gel transition in irreversible particulate systems,” *Soft Matter*, vol. 7, no. 6, pp. 2284–2296, 2011.
[31] F. Pierce, C. M. Sorensen, and A. Chakrabarti, “Computer simulation of diffusion-limited cluster-cluster aggregation with an Epstein drag force,” *Phys. Rev. E*, vol. 74, no. 2, Aug. 2006.
[32] J. Cai, N. Lu, and C. M. Sorensen, “Analysis of Fractal Cluster Morphology Parameters: Structural Coefficient and Density Autocorrelation Function Cutoff,” *J. Colloid Interface Sci.*, vol. 171, no. 2, pp. 470–473, May 1995.
[33] ü. ö. Köylü, G. M. Faeth, T. L. Farias, and M. G. Carvalho, “Fractal and projected structure properties of soot aggregates,” *Combust. Flame*, vol. 100, no. 4, pp. 621–633, Mar. 1995.
[34] A. M. Brasil, T. L. Farias, and M. G. Carvalho, “Evaluation of the Fractal Properties of Cluster?Cluster Aggregates,” *Aerosol Sci. Technol.*, vol. 33, no. 5, pp. 440–454, Nov. 2000.
[35] C. Oh and C. M. Sorensen, “The Effect of Overlap between Monomers on the Determination of Fractal Cluster Morphology,” *J. Colloid Interface Sci.*, vol. 193, no. 1, pp. 17–25, Sep. 1997.
[36] A. Chakrabarti, D. Fry, and C. M. Sorensen, “Molecular dynamics simulation of the transition from dispersed to solid phase,” *Phys. Rev. E*, vol. 69, no. 3, Mar. 2004.
[37] C. M. Sorensen and C. Oh, “Divine proportion shape preservation and the fractal nature of cluster-cluster aggregates,” *Phys. Rev. E*, vol. 58, no. 6, pp. 7545–7548, Dec. 1998.
[38] R. Botet, R. Jullien, and M. Kolb, “Hierarchical Model for Irreversible Kinetic Cluster Formation,” *J. Phys. -Math. Gen.*, vol. 17, no. 2, pp. L75–L79, 1984.
[39] W. R. Heinson, C. M. Sorensen, and A. Chakrabarti, “A three parameter description of the structure of diffusion limited cluster fractal aggregates,” *J. Colloid Interface Sci.*, vol. 375, pp. 65–69, Jun. 2012.
[40] H. S. M. Coxeter, *Introduction to Geometry*, 2nd edition. New York: Wiley, 1989.

[41] H. E. Huntley, *The Divine Proportion: A Study in Mathematical Beauty*, 1st edition. New York: Dover Publications, 1970.
[42] P. Warren and R. Ball, "Anisotropy and the Approach to Scaling in Monodisperse Reaction-Limited Cluster-Cluster Aggregation," *J. Phys. -Math. Gen.*, vol. 22, no. 9, pp. 1405–1413, May 1989.
[43] N. J. A. Sloane, "The On-Line Encyclopedia of Integer Sequences," *The On-Line Encyclopedia of Integer Sequences*. [Online]. Available: https://oeis.org/.
[44] D. Weitz and M. Oliveria, "Fractal Structures Formed by Kinetic Aggregation of Aqueous Gold Colloids," *Phys. Rev. Lett.*, vol. 52, no. 16, pp. 1433–1436, 1984.
[45] D. Schaefer, J. Martin, P. Wiltzius, and D. Cannell, "Fractal Geometry of Colloidal Aggregates," *Phys. Rev. Lett.*, vol. 52, no. 26, pp. 2371–2374, 1984.
[46] J. Martin, D. Schaefer, and A. Hurd, "Fractal Geometry of Vapor-Phase Aggregates," *Phys. Rev. A*, vol. 33, no. 5, pp. 3540–3543, May 1986.
[47] R. Samson, G. Mulholland, and J. Gentry, "Structural-Analysis of Soot Agglomerates," *Langmuir*, vol. 3, no. 2, pp. 272–281, Apr. 1987.
[48] R. Dobbins and C. Megaridis, "Morphology of Flame-Generated Soot as Determined by Thermophoretic Sampling," *Langmuir*, vol. 3, no. 2, pp. 254–259, Apr. 1987.
[49] H. Zhang, C. Sorensen, E. Ramer, B. Olivier, and J. Merklin, "Insitu Optical Structure Factor Measurements of an Aggregating Soot Aerosol," *Langmuir*, vol. 4, no. 4, pp. 867–871, Aug. 1988.
[50] M. Lattuada, H. Wu, and M. Morbidelli, "A simple model for the structure of fractal aggregates," *J. Colloid Interface Sci.*, vol. 268, no. 1, pp. 106–120, Dec. 2003.
[51] W. R. Heinson, C. M. Sorensen, and A. Chakrabarti, "Does Shape Anisotropy Control the Fractal Dimension in Diffusion-Limited Cluster-Cluster Aggregation?," *Aerosol Sci. Technol.*, vol. 44, no. 12, pp. i–iv, Nov. 2010.
[52] P. Meakin, "Off Lattice Simulations of Cluster Cluster Aggregation in Dimensions 2-6," *Phys. Lett. A*, vol. 107, no. 6, pp. 269–272, 1985.
[53] P. Kulkarni, P. A. Baron, and K. Willeke, Eds., *Aerosol Measurement: Principles, Techniques, and Applications*, 3 edition. Wiley, 2011.
[54] S. N. Rogak and R. C. Flagan, "Coagulation of aerosol agglomerates in the transition regime," *J. Colloid Interface Sci.*, vol. 151, no. 1, pp. 203–224, Jun. 1992.
[55] R. Gopalakrishnan and C. J. Hogan, "Determination of the Transition Regime Collision Kernel from Mean First Passage Times," *Aerosol Sci. Technol.*, vol. 45, no. 12, pp. 1499–1509, Dec. 2011.
[56] M. S. Bogdan Nowakowski, "Brownian coagulation of aerosol particles by Monte Carlo simulation," *J. Colloid Interface Sci.*, vol. 83, no. 2, pp. 614–622, 1981.
[57] R. D. Mountain, G. W. Mulholland, and H. Baum, "Simulation of aerosol agglomeration in the free molecular and continuum flow regimes," *J. Colloid Interface Sci.*, vol. 114, no. 1, pp. 67–81, Nov. 1986.
[58] G. W. Mulholland, R. J. Samson, R. D. Mountain, and M. H. Ernst, "Cluster size distribution for free molecular agglomeration," *Energy Fuels*, vol. 2, no. 4, pp. 481–486, Jul. 1988.
[59] W. F. van Gunsteren and H. J. C. Berendsen, "Algorithms for brownian dynamics," *Mol. Phys.*, vol. 45, no. 3, pp. 637–647, Feb. 1982.
[60] G. M. Wang and C. M. Sorensen, "Diffusive mobility of fractal aggregates over the entire knudsen number range," *Phys. Rev. E*, vol. 60, no. 3, pp. 3036–3044, Sep. 1999.

[61] C. M. Sorensen, “The Mobility of Fractal Aggregates: A Review,” *Aerosol Sci. Technol.*, vol. 45, no. 7, pp. 765–779, Jul. 2011.
[62] P. van Dongen and M. Ernst, “Dynamic Scaling in the Kinetics of Clustering,” *Phys. Rev. Lett.*, vol. 54, no. 13, pp. 1396–1399, Apr. 1985.
[63] D. J. Fry, “Aggregation in dense particulate systems,” 2003.
[64] C. Oh and C. M. Sorensen, “Light scattering study of fractal cluster aggregation near the free molecular regime,” *J. Aerosol Sci.*, vol. 28, no. 6, pp. 937–957, Sep. 1997.
[65] F. G. Pierce, “Aggregation in colloids and aerosols,” 2007.
[66] C. Sorensen, W. Hageman, T. Rush, H. Huang, and C. Oh, “Aerogelation in a Flame Soot Aerosol,” *Phys. Rev. Lett.*, vol. 80, no. 8, pp. 1782–1785, Feb. 1998.
[67] W. Kim, C. M. Sorensen, and A. Chakrabarti, “Universal Occurrence of Soot Superaggregates with a Fractal Dimension of 2.6 in Heavily Sooting Laminar Diffusion Flames,” *Langmuir*, vol. 20, no. 10, pp. 3969–3973, May 2004.
[68] R. K. Chakrabarty, H. Moosmüller, M. A. Garro, and C. B. Stipe, “Observation of Superaggregates from a Reversed Gravity Low-Sooting Flame,” *Aerosol Sci. Technol.*, vol. 46, no. 1, pp. i–iii, Jan. 2012.
[69] R. Dhaubhadel, F. Pierce, A. Chakrabarti, and C. M. Sorensen, “Hybrid superaggregate morphology as a result of aggregation in a cluster-dense aerosol,” *Phys. Rev. E*, vol. 73, no. 1, Jan. 2006.
[70] R. Dhaubhadel, C. S. Gerving, A. Chakrabarti, and C. M. Sorensen, “Aerosol Gelation: Synthesis of a Novel, Lightweight, High Specific Surface Area Material,” *Aerosol Sci. Technol.*, vol. 41, no. 8, pp. 804–810, Jul. 2007.
[71] R. Dhaubhadel, A. Chakrabarti, and C. M. Sorensen, “Light Scattering Study of Aggregation Kinetics in Dense, Gelling Aerosols,” *Aerosol Sci. Technol.*, vol. 43, no. 11, pp. 1053–1063, Oct. 2009.
[72] R. Dhaubhadel, “An experimental study of dense aerosol aggregations,” 2008.
[73] G. D. Ulrich and N. S. Subramanian, “III. Coalescence as a Rate-Controlling Process,” *Combust. Sci. Technol.*, vol. 17, no. 3–4, pp. 119–126, Dec. 1977.
[74] W. Koch and S. . Friedlander, “The effect of particle coalescence on the surface area of a coagulating aerosol,” *J. Colloid Interface Sci.*, vol. 140, no. 2, pp. 419–427, Dec. 1990.
[75] F. E. Kruis, K. A. Kusters, S. E. Pratsinis, and B. Scarlett, “A Simple Model for the Evolution of the Characteristics of Aggregate Particles Undergoing Coagulation and Sintering,” *Aerosol Sci. Technol.*, vol. 19, no. 4, pp. 514–526, Jan. 1993.
[76] T. Johannessen, S. E. Pratsinis, and H. Livbjerg, “Computational analysis of coagulation and coalescence in the flame synthesis of titania particles,” *Powder Technol.*, vol. 118, no. 3, pp. 242–250, Aug. 2001.
[77] H. Mühlenweg, A. Gutsch, A. Schild, and S. E. Pratsinis, “Process simulation of gas-to-particle-synthesis via population balances: Investigation of three models,” *Chem. Eng. Sci.*, vol. 57, no. 12, pp. 2305–2322, Jun. 2002.
[78] S. Tsantilis and S. E. Pratsinis, “Soft- and Hard-Agglomerate Aerosols Made at High Temperatures,” *Langmuir*, vol. 20, no. 14, pp. 5933–5939, Jul. 2004.
[79] M. C. Heine and S. E. Pratsinis, “Polydispersity of primary particles in agglomerates made by coagulation and sintering,” *J. Aerosol Sci.*, vol. 38, no. 1, pp. 17–38, Jan. 2007.
[80] H.-J. Schmid, B. Al-Zaitone, C. Artelt, and W. Peukert, “Evolution of the fractal dimension for simultaneous coagulation and sintering,” *Chem. Eng. Sci.*, vol. 61, no. 1, pp. 293–305, Jan. 2006.

[81] M. Sander, R. H. West, M. S. Celnik, and M. Kraft, “A Detailed Model for the Sintering of Polydispersed Nanoparticle Agglomerates,” *Aerosol Sci. Technol.*, vol. 43, no. 10, pp. 978–989, Sep. 2009.
[82] P. Meakin, “Computer simulation of cluster-cluster aggregation using linear trajectories: Results from three-dimensional simulations and a comparison with aggregates formed using brownian trajectories,” *J. Colloid Interface Sci.*, vol. 102, no. 2, pp. 505–512, Dec. 1984.
[83] D. Fry, T. Sintes, A. Chakrabarti, and C. M. Sorensen, “Enhanced Kinetics and Free-Volume Universality in Dense Aggregating Systems,” *Phys. Rev. Lett.*, vol. 89, no. 14, Sep. 2002.
[84] T. Serra, J. Colomer, and X. Casamitjana, “Aggregation and Breakup of Particles in a Shear Flow,” *J. Colloid Interface Sci.*, vol. 187, no. 2, pp. 466–473, Mar. 1997.
[85] F. E. Torres, W. B. Russel, and W. R. Schowalter, “Floc structure and growth kinetics for rapid shear coagulation of polystyrene colloids,” *J. Colloid Interface Sci.*, vol. 142, no. 2, pp. 554–574, Mar. 1991.
[86] T. Serra and X. Casamitjana, “Structure of the Aggregates During the Process of Aggregation and Breakup Under a Shear Flow,” *J. Colloid Interface Sci.*, vol. 206, no. 2, pp. 505–511, Oct. 1998.
[87] Y. Kikuchi, H. Yamada, H. Kunimori, T. Tsukada, M. Hozawa, C. Yokoyama, and M. Kubo, “Aggregation Behavior of Latex Particles in Shear Flow Confined between Two Parallel Plates,” *Langmuir*, vol. 21, no. 8, pp. 3273–3278, Apr. 2005.
[88] C. Selomulya, G. Bushell, R. Amal, and T. D. Waite, “Aggregation Mechanisms of Latex of Different Particle Sizes in a Controlled Shear Environment,” *Langmuir*, vol. 18, no. 6, pp. 1974–1984, Mar. 2002.
[89] M. . Lin, R. Klein, H. . Lindsay, D. . Weitz, R. . Ball, and P. Meakin, “The structure of fractal colloidal aggregates of finite extent,” *J. Colloid Interface Sci.*, vol. 137, no. 1, pp. 263–280, Jun. 1990.
[90] J. Martin, J. Wilcoxon, D. Schaefer, and J. Odinek, “Fast aggregation of colloidal silica,” *Phys. Rev. A*, vol. 41, no. 8, pp. 4379–4391, Apr. 1990.
[91] S. J. Jung, R. Amal, and J. A. Raper, “Monitoring effects of shearing on floc structure using small-angle light scattering,” *Powder Technol.*, vol. 88, no. 1, pp. 51–54, Jul. 1996.
[92] L. Wang, D. L. Marchisio, R. D. Vigil, and R. O. Fox, “CFD simulation of aggregation and breakage processes in laminar Taylor–Couette flow,” *J. Colloid Interface Sci.*, vol. 282, no. 2, pp. 380–396, Feb. 2005.
[93] V. Oles, “Shear-induced aggregation and breakup of polystyrene latex particles,” *J. Colloid Interface Sci.*, vol. 154, no. 2, pp. 351–358, Dec. 1992.
[94] M. Vanni and A. Gastaldi, “Hydrodynamic Forces and Critical Stresses in Low-Density Aggregates under Shear Flow,” *Langmuir*, vol. 27, no. 21, pp. 12822–12833, Nov. 2011.
[95] G. Frappier, B. S. Lartiges, and S. Skali-Lami, “Floc Cohesive Force in Reversible Aggregation: A Couette Laminar Flow Investigation,” *Langmuir*, vol. 26, no. 13, pp. 10475–10488, Jul. 2010.
[96] V. Becker and H. Briesen, “A master curve for the onset of shear induced restructuring of fractal colloidal aggregates,” *J. Colloid Interface Sci.*, vol. 346, no. 1, pp. 32–36, Jun. 2010.
[97] A. Zaccone, M. Soos, M. Lattuada, H. Wu, M. U. Bäbler, and M. Morbidelli, “Breakup of dense colloidal aggregates under hydrodynamic stresses,” *Phys. Rev. E*, vol. 79, no. 6, Jun. 2009.

[98] H. Huang and C. M. Sorensen, "Shear effects during the gelation of aqueous gelatin," *Phys. Rev. E*, vol. 53, no. 5, pp. 5075–5078, May 1996.
[99] T. Mokhtari, A. Chakrabarti, C. M. Sorensen, C. Cheng, and D. Vigil, "The effect of shear on colloidal aggregation and gelation studied using small-angle light scattering," *J. Colloid Interface Sci.*, vol. 327, no. 1, pp. 216–223, Nov. 2008.
[100] D. O. Riese, G. H. Wegdam, W. L. Vos, R. Sprik, D. Fenistein, J. H. H. Bongaerts, and G. Grübel, "Effective Screening of Hydrodynamic Interactions in Charged Colloidal Suspensions," *Phys. Rev. Lett.*, vol. 85, no. 25, pp. 5460–5463, Dec. 2000.
[101] J. K. G. Dhont, "Shear Induced Displacement of the Spinodal of Brownian Systems," *Phys. Rev. Lett.*, vol. 76, no. 22, pp. 4269–4272, May 1996.
[102] S. Asakura and F. Oosawa, "On Interaction between Two Bodies Immersed in a Solution of Macromolecules," *J. Chem. Phys.*, vol. 22, no. 7, pp. 1255–1256, Jul. 1954.
[103] J. R. Melrose, "Aggregate Networks Under Shear," *Europhys. Lett. EPL*, vol. 19, no. 1, pp. 51–56, May 1992.
[104] S. J. Khan, C. M. Sorensen, and A. Chakrabarti, "Kinetics and morphology of cluster growth in a model of short-range attractive colloids," *J. Chem. Phys.*, vol. 131, no. 19, p. 194908, 2009.
[105] A. W. Lees and S. F. Edwards, "The computer study of transport processes under extreme conditions," *J. Phys. C Solid State Phys.*, vol. 5, no. 15, pp. 1921–1928, Aug. 1972.
[106] A. T. Skjeltorp, "Visualization and characterization of colloidal growth from ramified to faceted structures," *Phys. Rev. Lett.*, vol. 58, no. 14, pp. 1444–1447, Apr. 1987.
[107] P. R. ten Wolde, M. J. Ruiz-Montero, and D. Frenkel, "Numerical calculation of the rate of crystal nucleation in a Lennard-Jones system at moderate undercooling," *J. Chem. Phys.*, vol. 104, no. 24, pp. 9932–9947, Jun. 1996.
[108] P.-R. ten Wolde, M. J. Ruiz-Montero, and D. Frenkel, "Simulation of homogeneous crystal nucleation close to coexistence," *Faraday Discuss.*, vol. 104, p. 93, 1996.
[109] R. K. Chakrabarty, N. D. Beres, H. Moosmüller, S. China, C. Mazzoleni, M. K. Dubey, L. Liu, and M. I. Mishchenko, "Soot superaggregates from flaming wildfires and their direct radiative forcing," *Sci. Rep.*, vol. 4, Jul. 2014.
[110] C. Dominik, J. Blum, J. Cuzzi, and G. Wurm, "Growth of Dust as the Initial Step Toward Planet Formation," *ArXivastro-Ph0602617*, Feb. 2006.
[111] B. H. Samset, G. Myhre, M. Schulz, Y. Balkanski, S. Bauer, T. K. Berntsen, H. Bian, N. Bellouin, T. Diehl, R. C. Easter, S. J. Ghan, T. Iversen, S. Kinne, A. Kirkevåg, J.-F. Lamarque, G. Lin, X. Liu, J. Penner, ø. Seland, R. B. Skeie, P. Stier, T. Takemura, K. Tsigaridis, and K. Zhang, "Black carbon vertical profiles strongly affect its radiative forcing uncertainty," *Atmospheric Chem. Phys. Discuss.*, vol. 12, no. 11, pp. 28929–28953, Nov. 2012.
[112] B. H. Samset, G. Myhre, A. Herber, Y. Kondo, S.-M. Li, N. Moteki, M. Koike, N. Oshima, J. P. Schwarz, Y. Balkanski, S. E. Bauer, N. Bellouin, T. K. Berntsen, H. Bian, M. Chin, T. Diehl, R. C. Easter, S. J. Ghan, T. Iversen, A. Kirkevåg, J.-F. Lamarque, G. Lin, X. Liu, J. E. Penner, M. Schulz, Ø. Seland, R. B. Skeie, P. Stier, T. Takemura, K. Tsigaridis, and K. Zhang, "Modelled black carbon radiative forcing and atmospheric lifetime in AeroCom Phase II constrained by aircraft observations," *Atmos Chem Phys*, vol. 14, no. 22, pp. 12465–12477, Nov. 2014.
[113] J. P. Schwarz, J. R. Spackman, R. S. Gao, L. A. Watts, P. Stier, M. Schulz, S. M. Davis, S. C. Wofsy, and D. W. Fahey, "Global-scale black carbon profiles observed in the remote

atmosphere and compared to models: HIPPO1 BLACK CARBON PROFILES," *Geophys. Res. Lett.*, vol. 37, no. 18, Sep. 2010.

[114] S. E. Bauer, S. Menon, D. Koch, T. C. Bond, and K. Tsigaridis, "A global modeling study on carbonaceous aerosol microphysical characteristics and radiative effects," *Atmospheric Chem. Phys.*, vol. 10, no. 15, pp. 7439–7456, Aug. 2010.